UNIVERSIDADE DA BEIRA INTERIOR
Engenharia

Aerodynamic Analysis of a Forward-Backward Facing Step Pair on the Upper Surface of a Low-Speed Airfoil

Luís Gonçalo Azevedo Freitas

Dissertação para obtenção do Grau de Mestre em
Engenharia Aeronáutica
(Ciclo de estudos integrado)

Orientador: Professor Doutor Pedro Vieira Gamboa

Covilhã, fevereiro de 2017

This page has been intentionally left blank
for double side copying

To my beloved parents, for their love, trust, and support.

This page has been intentionally left blank
for double side copying

Acknowledgments

I wish to express my most sincere thanks to all who supported me in the execution of this work and throughout these five and a half years away from home.

First, I would like to thank my supervisor, Professor Pedro Gamboa, for allowing me the opportunity to work with him, to participate in an incredible project and for all the guidance, motivation, support, and knowledge throughout this work and during the degree.

Further, I would like to thank my parents, who always believed in me and supported me with unconditional kindness, love, and support during all these years and in every decision in my live, and my sisters, Sara and Cristina, for their support, with a special acknowledgement to Cristina for helping me in the elaboration of this work.

At the same time, I would like to thank my girlfriend, Joana Freitas, for all the support, understanding, dedication, help and love demonstrated throughout the project and during these years.

Finally, I would like to thank my family and all my friends and colleagues in Covilhã and Madeira, in particular my friend Father Manuel Ornelas and my godmother Rita, for their friendship and support.

To all of them, thank you.

This page has been intentionally left blank
for double side copying

Abstract

The Long Endurance Electric Unmanned Air Vehicle (LEEUAV) is a project of a green, low-cost, small footprint electric solar UAV which was designed for civilian surveillance applications, such as coast, forest, or border patrol. Therefore, long endurance is desired, which is accomplished by a lightweight airframe design and an electric propulsion system assisted with solar cell arrays. The LEEUAV has an approximated mass of 5 kg, 4.5 m of wingspan and an 8-hour flight endurance.

To ease the construction, its wing, in addition to its aerodynamic function, must accommodate the solar cells on its upper surface. Since the solar cells have a finite thickness, they create an offset, with a forward facing step at the beginning of the solar cell array and a backward facing step at its end. These two steps affect the aerodynamic performance of the wing mainly because the forward facing step forces the transition of the flow from laminar to turbulent.

The aim of this thesis is to study the influence of these steps in the aerodynamic coefficients of the LEEUAV's airfoil, having as variables the offset's position, length, and thickness. To do this, a numerical analysis was performed initially using XFOIL, an interactive program for the analysis of subsonic airfoils, and then ANSYS Fluent, a commercial computational fluid dynamics (CFD) software.

First, in XFOIL, a total of 444 combinations of offsets were tested, in order to understand the range of positions that could be more appropriate for placing the solar cells. After this initial study, another analysis was performed to better understand their most appropriate positions, considering their precise thickness and length. Afterwards, a small amount of combinations was chosen to perform a CFD analysis that served to validate and refine the results obtained from XFOIL. Since there was no experimental data regarding the LEEUAV's airfoil, several turbulence models were initially tested to see which best resembled the XFOIL's solution. Subsequently, an analysis of the selected combinations was performed and the best position for placing the solar cells, based on the performed analysis, is between 21% and 23% of the airfoil's chord.

Keywords

LEEUAV, solar cells, aerodynamic, steps, airfoil, numerical analysis, XFOIL, ANSYS Fluent

This page has been intentionally left blank
for double side copying

Resumo

O Long Endurance Electric Unmanned Air Vehicle (LEEUAV) é um projeto de um UAV elétrico solar, ecológico e de baixo-custo, projetado para aplicações civis de vigilância, tais como patrulha costeira, florestal ou de fronteira. Portanto, uma grande autonomia é fundamental, para a qual contribui um design de estrutura leve e um sistema de propulsão elétrico assistido por um conjunto de células fotovoltaicas. O LEEUAV tem uma massa aproximada de 5 kg, 4,5 m de envergadura e uma autonomia de voo de 8 horas.

Para facilitar a construção, a sua asa, além da sua função aerodinâmica, tem de acomodar as células fotovoltaicas no seu extradorso e, uma vez que as células possuem uma espessura finita, originam um *offset* (rebordo), com um degrau no início e no fim do conjunto de células fotovoltaicas. Como consequência, estes degraus afetam o desempenho aerodinâmico da asa.

O objetivo deste trabalho é estudar a influência destes degraus nos coeficientes aerodinâmicos do perfil alar do LEEUAV, tendo como variáveis a posição, o comprimento e a espessura do *offset*. Para o concretizar, foi realizada uma análise numérica utilizando, primeiramente, o XFOIL, um programa interativo para a análise de perfis alares subsónicos. E em seguida, utilizando o ANSYS Fluent, um *software* comercial de dinâmica de fluidos computacional (CFD).

Em primeiro lugar, no XFOIL, foi testado um total de 444 combinações de *offsets*, a fim de compreender a gama de posições que poderia ser mais apropriada para colocar as células fotovoltaicas. Após este estudo inicial, foi realizada outra análise, desta vez considerando a espessura e o comprimento específico das células. Posteriormente, uma pequena quantidade de combinações foi escolhida para realizar uma análise de CFD, que serviu para validar e refinar os resultados obtidos do XFOIL. Como não existiam dados experimentais do perfil alar do LEEUAV, vários modelos de turbulência foram testados, para ver qual o que se melhor assemelharia à solução do XFOIL. Depois, foi realizada uma análise às combinações selecionadas, e concluiu-se que as melhores posições para colocar o início das células fotovoltaicas, com base no estudo realizado, são entre 21% e 23% da corda do perfil alar.

Palavras-chaves

LEEUAV, células fotovoltaicas, aerodinâmica, degraus, perfil alar, análise, XFOIL, ANSYS Fluent

This page has been intentionally left blank
for double side copying

Resumo Alargado

Esta dissertação surgiu no âmbito do projeto Long Endurance Electric Unmanned Air Vehicle (LEEUAV), que é um projeto de um UAV elétrico solar, ecológico, de baixo-custo e de pequena pegada ecológica, projetado para aplicações civis de vigilância, tais como patrulha costeira, florestal ou de fronteira. O projeto da aeronave foi desenvolvido internamente no Laboratório Associado de Energia, Transportes e Aeronáutica (LAETA).

Na Figura 1, é apresentado um desenho CAD e uma foto do protótipo do LEEUAV.

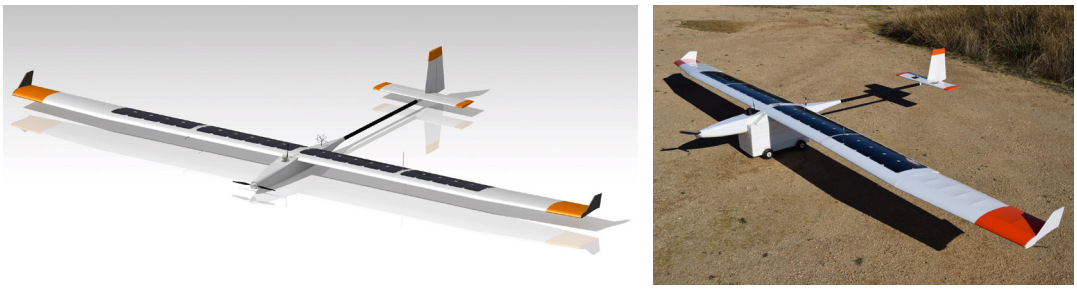

Figura 1 – Renderização CAD do LEEUAV (à esquerda) e protótipo do LEEUAV (à direita)

O LEEUAV tem uma massa aproximada de 5 kg, 4,5 m de envergadura, é capaz de transportar uma carga útil de 1 kg e possui uma autonomia de voo de 8 horas. Um dos pontos fulcrais deste projeto é a sua grande autonomia, concretizada graças a um design de estrutura leve e a um sistema de propulsão elétrico, assistido por um conjunto de células fotovoltaicas. As especificações do LEEUAV incluem a capacidade de descolagem em pistas curtas, a facilidade de construção e manutenção e a alta flexibilidade para realizar diferentes missões de vigilância civis.

Tendo como objetivo a facilidade de construção, foi decidido que a sua asa, além da função aerodinâmica, teria de acomodar as células fotovoltaicas no seu extradorso, em vez de estarem incorporadas na casca da asa. Uma vez que as células possuem uma espessura finita, originam um *offset* (rebordo), com um degrau virado para a frente, no início do conjunto, e um degrau virado para trás, no fim. Estes dois degraus afetam o desempenho aerodinâmico da asa, principalmente porque o degrau virado para a frente força a transição do escoamento de laminar para turbulento.

Na Figura 2, é mostrado este *offset* no extradorso do perfil alar do LEEUAV.

Figura 2 – Perfil alar do LEEUAV com células fotovoltaicas (*offset*) no extradorso

O objetivo deste trabalho é então estudar a influência destes degraus nos coeficientes aerodinâmicos do perfil alar do LEEUAV, tendo como variáveis a posição, o comprimento e a espessura do *offset*, e determinar a melhor posição longitudinal para colocar as células fotovoltaicas no extradorso do perfil alar, com o objetivo de minimizar os efeitos penalizantes no desempenho aerodinâmico. Para concretizar isto, uma análise numérica foi realizada utilizando inicialmente o XFOIL, um programa interativo para a análise de perfis alares subsónicos e, em seguida, o ANSYS Fluent, um *software* comercial de dinâmica de fluidos computacional (CFD).

Em primeiro lugar, no XFOIL, foi testado um total de 444 combinações de *offsets*, a fim de compreender a gama de posições que poderia ser mais apropriada para colocar as células fotovoltaicas. Concluiu-se que a posição do degrau virado para a frente é o que tem mais influência no desempenho do perfil e que a melhor posição para o colocar é entre 20% e 30% da corda do perfil alar. Após este estudo inicial, foi realizada outra análise para compreender melhor as posições mais apropriadas, desta vez considerando a espessura e o comprimento específico das células fotovoltaicas, sendo que se concluiu que a melhor posição para colocar o início das células fotovoltaicas é entre 21% e 23% da corda do perfil alar.

Posteriormente, uma pequena quantidade de combinações foi escolhida para realizar um estudo de CFD, que serviu para validar e refinar os resultados obtidos do XFOIL. Como não existiam dados experimentais do perfil alar do LEEUAV, dois modelos de turbulência foram inicialmente testados, mais especificamente o *Realizable k-ε model* e o *SST k-ω model*, para ver qual o que se melhor assemelhava à solução do XFOIL. Depois foi realizada uma análise às combinações selecionadas e às possíveis melhores posições para colocar as células fotovoltaicas. Com base nessa análise, confirmou-se e concluiu-se que é entre 21% e 23% da corda do perfil alar que se deve colocar o início das células fotovoltaicas, com perdas aproximadas de até 5% na eficiência aerodinâmica, em comparação com o perfil limpo original.

Contents

List of Figures

List of Charts

This page has been intentionally left blank
for double side copying

List of Tables

This page has been intentionally left blank
for double side copying

List of Acronyms

BFS	Backward Facing Step
CAD	Computer-Aided Design
CFD	Computational Fluid Dynamics
FFS	Forward Facing Step
LAETA	Associated Laboratory for Energy, Transport, and Aeronautics
LEEUAV	Long Endurance Electric Unmanned Air Vehicle
NASA	National Aeronautics and Space Administration
RANS	Reynolds-Averaged Navier Stokes
SST	Shear-Stress Transport
UAV	Unmanned Air Vehicle

This page has been intentionally left blank
for double side copying

Nomenclature

c	Chord
M	Mach number
N	Amplification factor
Re	Reynolds number
C_d	Drag coefficient
$C_{d_{min}}$	Minimum drag coefficient
C_f	Skin friction coefficient
C_l	Lift coefficient
$C_{l_{max}}$	Maximum lift coefficient
$C_{l_{C_{d_{min}}}}$	Lift coefficient of minimum drag coefficient
$C_{l_{(C_l/C_d)_{max}}}$	Lift coefficient of maximum lift-to-drag ratio
$C_{l_{\left(C_l^{3/2}/C_d\right)_{max}}}$	Lift coefficient of maximum lift$^{3/2}$-to-drag ratio
C_m	Pitching moment coefficient
C_p	Pressure coefficient
C_l/C_d	Lift-to-drag ratio
$(C_l/C_d)_{max}$	Maximum lift-to-drag ratio
$C_l^{3/2}/C_d$	Lift$^{3/2}$-to-drag ratio
$\left(C_l^{3/2}/C_d\right)_{max}$	Maximum lift$^{3/2}$-to-drag ratio
T_u	Turbulence intensity
x_{tr_u}/c	Relative (to the chord) transition point on the upper surface
x_{tr_l}/c	Relative (to the chord) transition point on the lower surface
(t/c)	Offset thickness-to-chord ratio
$(x/c)_i$	Relative (to the chord) offset initial position
$(x/c)_f$	Relative (to the chord) offset final position
y^+	Dimensionless wall distance

Greek letters

α	Angle of attack
$\alpha_{C_{l_{max}}}$	Maximum lift angle of attack
$\alpha_{C_{d_{min}}}$	Angle of attack of minimum drag coefficient
$\alpha_{(C_l/C_d)_{max}}$	Angle of attack of maximum lift-to-drag ratio

$\alpha_{\left(C_l^{3/2}/C_d\right)_{max}}$	Angle of attack of maximum lift$^{3/2}$-to-drag ratio
ε	Turbulence dissipation rate
k	Turbulence kinetic energy
ω	Specific dissipation rate

Subscripts

i	Initial position
f	Final position
d	Drag
f	Skin friction
l	Lift
m	Pitching moment
p	Pressure
tr	Transition
u	Upper surface
l	Lower surface
max	Maximum condition
min	Minimum condition

Chapter 1

1.Introduction

"So, you see that this airplane is more a symbol. I don't think it will transport 200 people in the next years. But when Lindbergh crossed the Atlantic, the payload was also just sufficient for one person and some fuel. And 20 years later there were 200 people in every airplane crossing the Atlantic."

Bertrand Piccard

1.1. Motivation

The global unmanned aerial vehicle (UAV) market in the last decade has witnessed an enormous growth and the market of small UAVs has high growth potential due to increasing applications in civilian and commercial sectors [1]. Noteworthy applications include oil spill monitoring, search and rescue missions, fire detection and firefighting management, wildlife surveillance, natural disaster areas survey, powerline and pipeline monitoring, among many others.

In another front, society never had so much interest and demand for renewable energy and technology has never been so advanced and accessible to the user, for example, never electric systems such as solar panels, motors, and batteries have been so efficient nor design tools, both numerical and experimental, have been so accessible to the designer. [2]

With this potential of small UAVs, renewable energy, and technological advancements, came the project of the Long Endurance Electric Unmanned Air Vehicle (LEEUAV), which main objective was to develop a low cost, small footprint long endurance electric solar UAV, with the capability of being deployed from short airfields, easy to build and maintain and with high flexibility to perform different civilian surveillance missions.

Hereupon, for ease of construction, the solar panels were to be placed over the wing instead of being embedded into its skin. As a result of this decision, the solar panel placement would certainly affect the airflow on the upper surface of the wing. Therefore, it is important to understand the influence of the solar panels on the aerodynamic coefficients of the LEEUAV's airfoil and find the best position for their placement, in order to have the least impact on the wing's aerodynamic characteristics.

This project is expected to be a reference in the Portuguese UAV community and demonstrate that solar energy is an excellent alternative to achieve a clean and long endurance flight.

1.2. Objectives

The objective of this work is to analyze the influence of the solar panels on the LEEUAV's airfoil performance and to determine the best longitudinal position for placing the solar panels on the upper airfoil's surface with the view to minimize the penalties on the aerodynamic performance and achieve results closer to the ones provided by the initial design.

Firstly, a numerical analysis using XFOIL is to be performed to understand the influence of the solar panel position and thickness on the LEEUAV's airfoil performance, by obtaining the airfoil polar curves. In a second analysis, a few of the solar panels positions are to be analyzed in ANSYS Fluent to validate and refine the results obtained from XFOIL and to visualize the airflow over the airfoil and better understand the influence of the solar panels on the airflow.

The final objective is to provide the best position on the airfoil's chord for the solar panels and quantify the aerodynamic performance penalty associated with placing the solar arrays on the upper surface of the airfoil.

1.3. Overview

Chapter 1 provides the motivation for the development of the LEEUAV project as well as for the aerodynamic analysis of the influence of the solar panels on the airfoil's upper surface and the objective of this thesis.

Chapter 2 presents a brief historic development of solar energy in aeronautics, in particular in UAVs and the state-of-the-art in a manned solar airplane design, and also presents the effects arising from steps.

Chapter 3 briefly presents the Long Endurance Electric UAV project.

Chapter 4 provides some specific concepts as an initial study to begin the analysis: a description of the aerodynamics of the airfoil, the problem definition, and the analysis methodology.

Chapter 5 shows how the first numerical analysis using XFOIL was performed and the conclusions drawn from the study performed.

Chapter 6 presents the second and more complex numerical analysis performed using ANSYS Fluent.

Chapter 7 contains the conclusions drawn from the two analyses regarding the best positions for placing the solar panels.

Chapter 2

2. Bibliographic Review

In this chapter, a brief history of the most significant solar Unmanned Air Vehicle (UAV) designs is presented, together with a project that have recently reached noteworthy achievements. Also, a brief explanation of the effects arising from steps on a surface and on airfoils is presented.

2.1. History of Solar-Powered Airplanes

Solar-powered airplanes consume solar energy instead of traditional fossil fuels which allows to achieve long endurance flights. Thus, they have received a significant amount of interest from researchers and the public alike.

2.1.1. Pioneers of Solar Flight

The first solar powered aircraft to fly was Sunrise I on November 4th 1974 in California (Figure 2-1). With a maiden flight of 20 minutes at an altitude of 100 m, Sunrise I, designed by R. J. Boucher from Astro Flight Inc., demonstrated, for the first time, that an airplane can fly on solar power alone. The Sunrise I had a wingspan of 9.8 m and a gross mass of 12.3 kg. Unfortunately, in 1975, Sunrise I was damaged in a wind storm during a test flight. [3]

An improved version, called Sunrise II, was then constructed. Sunrise II had the same configuration but was 13% lighter, aerodynamically cleaner and 33% more powerful than the Sunrise I. It was expected to reach 15.2 km of altitude in September 1975, but only reached 5.2 km because the command and control system failed. The aircraft was severely damaged and the test flight program was terminated. [3]

Figure 2-1 – Sunrise I (1974) [4]

2.1.2. High Altitude Long Endurance Unmanned Air Vehicles

In 1994, NASA started the Environmental Research Aircraft and Sensor Technology program in response to an increasing demand for high altitude and long endurance aircraft. Its objective was to conduct atmospheric measurements, surveillance missions and serve as a communication relay platform. [5]

The first aircraft used in the program was the solar cell and battery powered Pathfinder (Figure 2-2) that was originally built as a solely battery powered aircraft in the 1980's. In July 1997, it set the world altitude record for solar powered aircraft, reaching 21.8 km of altitude. It was later renamed to Pathfinder Plus (Figure 2-2) and modified with a larger wingspan, new solar cells, improved aerodynamic and propulsion technology. In August 1998, it reached 24.4 km and set a new altitude record. [5]

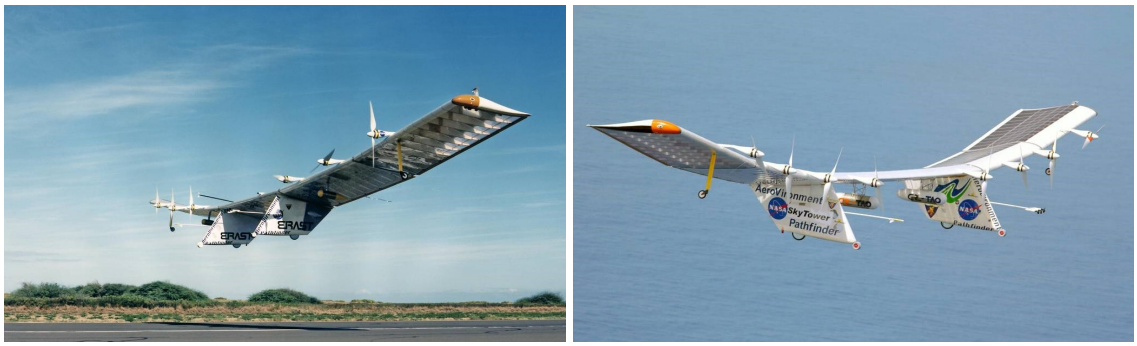

Figure 2-2 – Pathfinder (1997) (on the left) and Pathfinder Plus (2002) (on the right) [6]

The next prototype, the Centurion (Figure 2-3), had a 70% larger wingspan, was mostly made of carbon fiber and Kevlar, and was equipped with improved solar cells. A few test flights were made but the Centurion was just a stepping-stone in the program and was replaced by the final prototype of the series, Helios (Figure 2-3). The main goals set up for the Helios were to achieve sustained flight at an altitude of 30.5 km and to fly for 24 hours straight. In August 2001, Helios managed to achieve sustained flight over 29.3 km of altitude for 40 minutes and a maximum altitude of 29.5 km. Regrettably, it crashed in 2003 when it encountered turbulence. [5]

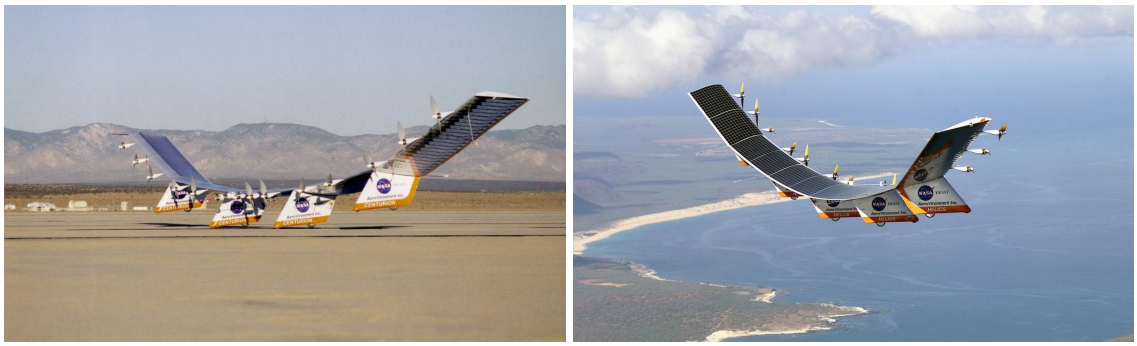

Figure 2-3 – Centurion (1998) (on the left) and Helios (2001) (on the right) [6]

2.1.3. Longest Duration Unmanned Flight

In 2001, a new project started to be developed by the British company QinetiQ, with a new prototype: Zephyr. It is a lightweight, solar-electric, high altitude long endurance UAV with the original objective of filming balloons while attempting to break the world altitude record. [4]

Several prototypes were constructed during the years and, in July 2010, Zephyr 7 (Figure 2-4) established a world flight endurance record of 336 hours and 21 minutes (14 days), in Yuma, Arizona. Zephyr 7 had 23 m of wingspan, 55 kg of mass, could carry a 5-kg payload, and had two propellers driven by electric motors and used energy from solar panels during the day and lithium-sulfur batteries at night. [4]

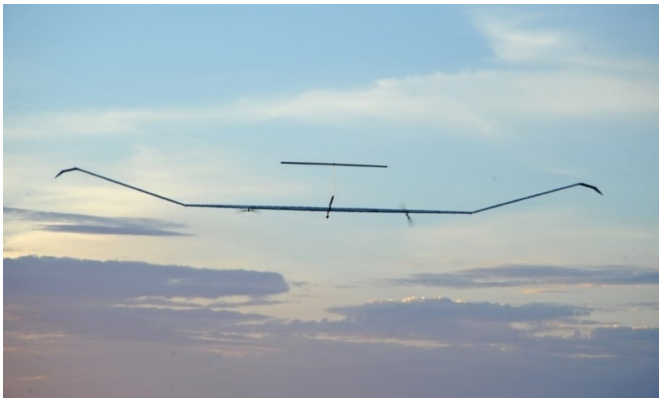

Figure 2-4 – Zephyr 7 (2014) [7]

2.1.4. The First Round-The-World Manned Solar Flight

Bertrand Piccard, a Swiss balloonist from a family of explorers and the first person to circumnavigate the world non-stop in a balloon, has a vision that clean technologies and energy efficiency can reduce our emissions and improve our quality of life. So, in 2003, he joined the Swiss École Polytechnique Fédérale de Lausanne with the ambitious objective of circumnavigating the globe in a solar-powered airplane. From this partnership, the Solar Impulse project was born in 2004. [4]

The first prototype (Figure 2-5), named HB-SIA, had a wingspan of 63.4 m (approximately the same wingspan as a Boeing 747-400), weighted less than 1.6 tons and was powered by four 10 hp motors using the energy collected from 11,628 photovoltaic cells. Surplus solar energy collected during the daytime was stored in 400 kg of lithium batteries. In July 2010, Solar Impulse completed a 26-hour flight using only solar energy. Two years later, it flew from Switzerland (Europe) to Morocco (Africa), which was the first solar-powered intercontinental flight in the world. [4]

Figure 2-5 – First Solar Impulse prototype (2013) [4]

In May 2013, Piccard and Andre Borschberg, a swiss engineer, entrepreneur, pilot, and co-founder of the Solar Impulse project, successfully completed the "Across America" project, whose objective was to fly the HB-SIA from San Francisco to New York. [4]

Named HB-SIB (Figure 2-6), the second prototype of the project had the objective to circumnavigate the globe. It has a 72-m wingspan, 17,248 solar cells and weighs 2.3 tons. It started the circumnavigation challenge in March 2015 in Abu Dhabi and its journey was divided in a total of 17 stages. [8]

Figure 2-6 – Solar Impulse HB-SIB (2016) [8]

On 26th July 2016, after 16 months, Solar Impulse arrived in Abu Dhabi, completing the circumnavigation trip of the globe with no fuel. During the journey, it achieved a maximum continuous flight time of 117 hours and 52 minutes (5 days), a maximum altitude of 8.5 km and a total amount of energy produced of 11,000 kWh during the circumnavigation. Solar Impulse flew 43,000 km in a total flight time of 23 days, across 4 continents, 2 oceans and 3 seas overflown to promote the use of renewable energies. [8]

2.2. Effects of Steps

The setback of placing solar cells on the upper surface of an airplane wing, since the solar cells have a finite thickness, is that, they create a localized thickening or an offset in the airfoil, with a forward facing step (FFS) at the beginning of the solar cell array and a backward facing step (BFS) at its end. These steps may cause separation of the flow: in the FFS flow, one or two regions of separation may occur, one upstream and one downstream, and in the BFS flow, one separated region develops downstream of the step.

In Figure 2-7, the streamwise velocity fluctuations over a forward-backward facing step pair in a study performed in reference [9] can be seen, where the thick black lines represent the separations lines. In this study, the first flow separation, upstream the forward facing step, does not generate a significant amount of turbulence, but in the separation after the sharp corner results in a significant increase of turbulence. Flow separation after the backward facing step also generates high turbulence levels, yet lower than those generated after the forward facing step. [9]

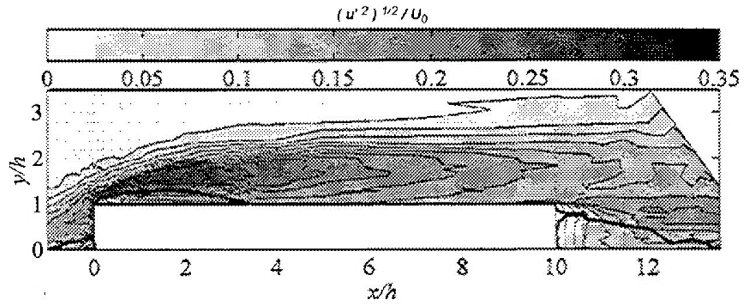

Figure 2-7 - Streamwise velocity fluctuations [9]

A review of several studies on flows over forward and backward facing steps can be found in reference [10].

2.2.1. Backward and Forward Facing Step Features

The backward facing step (Figure 2-8), the simplest reattaching flow among two-dimensional flows, has only one fixed separation line beginning at the edge of the step.

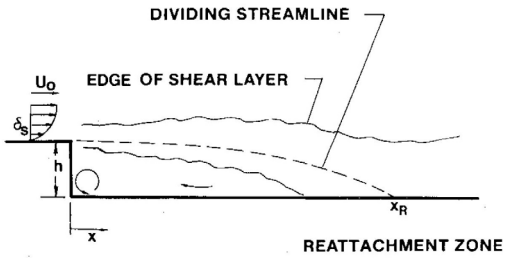

Figure 2-8 - Flow features over a backward facing step [11]

The upstream boundary layer separates at the sharp corner of the step forming a free-shear layer. If the boundary layer is laminar, transition begins soon after separation, unless Reynolds number is very low. The separated shear layer curves abruptly downwards in the reattachment zone and impinges on the wall. Part of the shear layer fluid is deflected upstream into the recirculating flow by a strong adverse pressure gradient. [11]

The flow over a forward facing step has a number of unique features that are shown in Figure 2-9. The step causes an adverse pressure gradient, which causes the flow to separate upstream of the step, the upstream recirculation region contains near stagnant fluid which acts as a slope angle. [12]

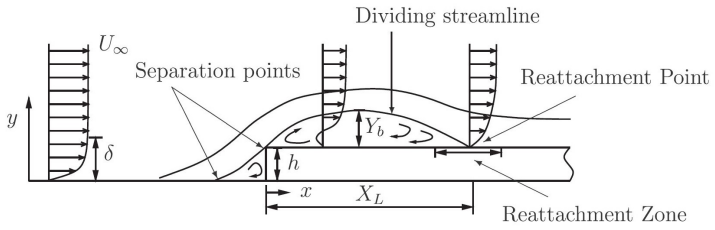

Figure 2-9 - Flow features over a foward facing step [12]

Depending on the Reynolds number and the thickness of the boundary layer, downstream of the step, a second separation may occur, with a recirculation region from the sharp corner to the reattachment point. Consequently, a strong shear layer develops between the low velocity reverse flow close to the wall and the mean free stream flow, increasing local mixing and turbulent intensity within the boundary layer. [12]

2.2.2. Backward Facing Step in an Airfoil

The first time a backward facing step was used in an airfoil was documented in the early 1960's, when Richard Kline and Floyd Fogleman designed a paper airplane with the objective to fly longer distances despite wind and turbulence. The airfoil (Figure 2-10) was flat on the top surface and partially hollowed at the bottom surface. [13]

Figure 2-10 – First Kline-Fogleman airfoil [14]

In 1972, they filled an U.S. patent for their airfoil, and two years later, NASA sponsored an experimental study to examine the Kline-Fogleman patented designs. The study showed that the lift-to-drag ratio of the new airfoil is lower than that of the flat plate, and the airfoil offered no advantages over conventional airfoils. [13]

Despite this, the Kline-Fogleman airfoils inspired Fertis and Smith to design an airfoil with a backward facing step this time on the upper surface (Figure 2-11). [13]

Figure 2-11 – Second Kline-Fogleman Airfoil (KFm-2) [15]

Wind tunnel testing performed by Fertis over a range of Reynolds numbers from 100,000 to 550,000 and over a wide range of angles of attack, showed improved stall characteristics, increased lift coefficients and increased lift-to-drag ratio. But this enhanced performance of airfoils with a backward facing step on the upper surface was not in perfect agreement with the results obtained by numerical and experimental testing done by other investigators, like the study done by Finaish and Witherspoon [16]. In their study, results showed that for a backward facing step installed on the upper surface, the lift-to-drag ratio decreased due to the increasing in the drag, which was directly proportional to the step depth. [13]

A more recent numerical study performed by Mishriky and Walsh [13], showed that using a backward facing step on the upper surface in comparison with the clean airfoil, has an adverse effect on the lift coefficient, the drag coefficient, and the maximum angle of attack. The lift coefficient showed a direct relationship with the location of the step, where the values of the lift coefficient continuously increased with shifting the step location from the leading edge to the trailing edge. And the values of drag coefficient followed and inverse relationship with the step location. [13]

As a consequence of the poor lift-to-drag ratio performance, the Kline-Fogleman airfoil has not been used on any full-size aircraft. But the Kline-Fogleman airfoil and its derivatives in recent years have gained popularity in the world of foam constructed radio controlled model aircraft because of the ease of construction and better lift performance compared to the flat plate, despite the drag penalty.

2.2.3. Increase in Camber and Thickness

The presence of the offset caused by the solar cells, besides the effects arising by the presence of the steps, also increases the camber and thickness of the airfoil, having its effects on the airfoil performance.

It is known that the increase in camber will shift the linear portion of the lift coefficient curve towards lower angles of attack, in other words, it will move the lift coefficient curve to the left. This results in an increase in lift coefficient as camber increases for a given angle of attack. And increasing thickness will affect the maximum lift coefficient but not the linear portion of the lift coefficient curve. [17]

Regarding the drag coefficient, the increase in camber will increase the drag coefficient at angles of attack near zero, moving the drag polar upwards and to the right. Increasing thickness will increase the point of zero-lift drag coefficient, with the effect of moving the drag polar curve to the right. [17]

One proof example of these effects can be found in reference [17], where the NACA airfoils in Figure 2-12 were used in a numerical study. They are distinguished in two series: same thickness and increasing camber (camber series); and same camber and increasing thickness (thickness series).

Figure 2-12 – Camber series (on the left) and thickness series (on the right) [17]

In Figure 2-13 the results of the numerical study are presented, showing the above stated effects on the lift coefficient curve and drag polar curve.

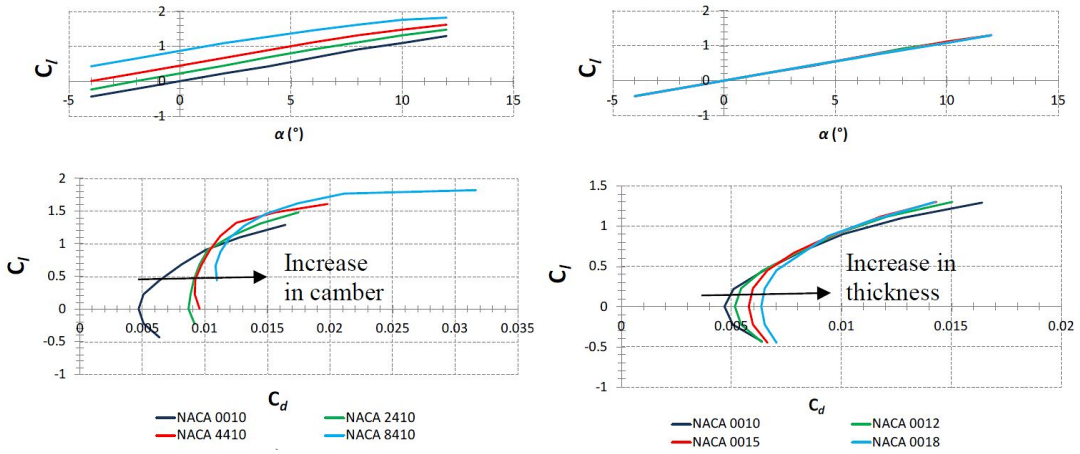

Figure 2-13 – Lift coefficient curve and drag polar for the camber series (on the left) and thickness series (on the right) [17]

Chapter 3

3. Long Endurance Electric Unmanned Air Vehicle

This Master's Thesis is part of a larger project denominated LEEUAV: Long Endurance Electric Unmanned Air Vehicle. In this chapter, a description of the aircraft mission and vehicle characterization is presented.

This project was developed by the Associated Laboratory for Energy, Transport, and Aeronautics (LAETA) and involved three investigation groups, namely the Center for Aerospace Science and Technology, the Aeronautics and Astronautics Research Center and the Institute of Mechanical Engineering. It is a project that is expected to be a reference in the Portuguese unmanned air vehicle community, particularly in academic circles.

For more details regarding the project references [2], [18], [19], [20], [21], and [22] should be consulted.

3.1. Project Requirements and Mission Profile

The objective of the project is the development of a green, low cost, long endurance, electric solar unmanned air vehicle, with low power requirement during cruise, capable of carrying a 1 kg payload and being deployed from short airfields. It should be easily disassembled so that it could be transported in a light vehicle, easy to build and maintain, and flexible enough to perform different civilian surveillance missions.

The mission profile in general terms is summarized in the following list:

- Take off in a very short distance (8 m), or hand launched (3 m);
- Climb to 1,000 m above ground level in 10 minutes;
- Continuous 8-hour flight in the solar equinox at an altitude of 1,000 m and faster than 7 m/s;
- Descend during 29 minutes without power until ground level;
- Landing in the field.

In Figure 3-1, a representative scheme of the mission profile is shown.

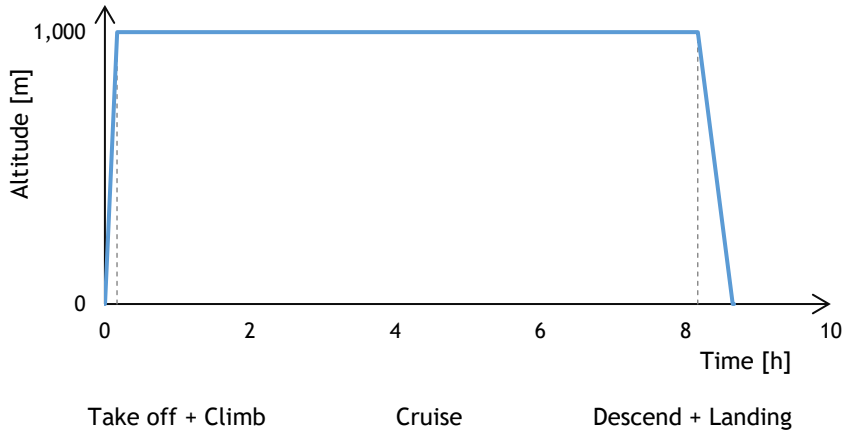

Figure 3-1 – LEEUAV's mission profile

3.2. Aircraft Description

Among others features, the LEEUAV specifications include:

- Long endurance, using electric propulsion assisted with solar power, particularly highly efficiency solar cells, high capacity/density batteries, efficient compact motors, and appropriate long endurance aerodynamic design;
- Autonomous flight, with auto-pilot navigation systems;
- High-strength, low weight structure, using composite materials, with critical areas in the wing and fuselage designed for good impact resistance on landing;
- Multiple missions, with sufficiently large payload range capability and upgradeable modular avionics, to enable an easy software upload and/or hardware swap to meet the selected missions' requirements.

In the selection of the design point the characteristics of the aircraft were established and the most important characteristics regarding dimensions, mass and performance are summarized in Table 3-1. Also, the LEEUAV front, top and left side view CAD drawing with dimensions (Figure 3-2), a CAD rendering (Figure 3-3) and photographs of the prototype with the solar cell arrays (Figure 3-4) are presented.

Table 3-1 – LEEUAV's characteristics

Dimensions		
Wingspan	4.50	m
Length	2.52	m
Wing mean chord	0.33	m
Wing root chord	0.35	m
Wing tip chord	0.25	m
Wing area	1.50	m^2
Aspect ratio	13.5	
Mass		
Structure mass	1.59	kg
Empty mass	3.89	kg
Takeoff mass	4.90	kg
Estimated Performance		
Maximum speed	21.1	m/s
Cruise speed	7.5	m/s
Stall speed	6.1	m/s
Lift-to-drag ratio	20	
Maximum rate of climb	2.2	m/s
Take-off roll distance	8.1	m
Endurance	8	h

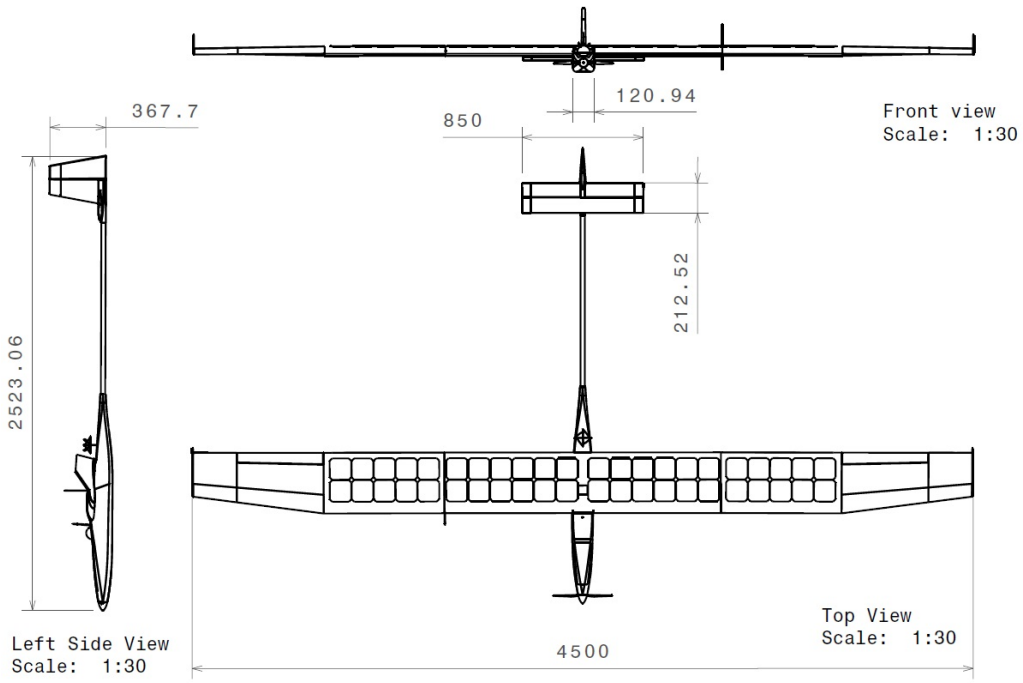

Figure 3-2 – LEEUAV's CAD drawing views

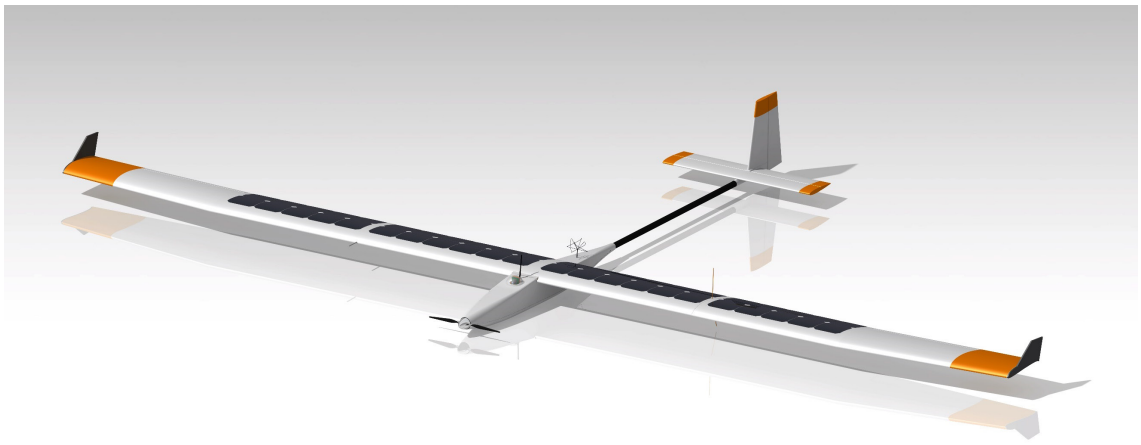

Figure 3-3 – LEEUAV's CAD rendering

Figure 3-4 – LEEUAV's prototype with solar panels

Regarding the airfoil, a new airfoil was developed using an in-house gradient based aerodynamic shape optimization tool. The design goal was to obtain an airfoil with good performance at low speeds, minimum drag coefficient in its design lift coefficient range and high maximum lift coefficient. A more detailed description of the airfoil and its performance is presented in the next chapter.

3.3. Propulsion System

The advantages of using solar energy is not only in terms of emissions and noise but also in providing long endurance, which is particularly important in this project. The propulsive system for the LEEUAV has an architecture completely different from conventional methods. It has resulted in a hybrid solution, using both lithium-polymer batteries and solar panels to provide energy to the electric motor.

The LEEUAV's propulsive system relies on the solar radiation captured by its 44 mono-crystalline silicon photovoltaic cells and one 11.1 V and 10,000 mAh lithium-polymer battery. Also, the propulsive system is equipped with a MPPT Genasun GV-10 for Li-ion batteries solar charger, a Castle Creations - Phoenix Edge with 75 A electronic speed controller and Hyperion ZS 3025-10 out-runner electric motor.

Figure 3-5 shows the LEEUAV's propulsive system scheme.

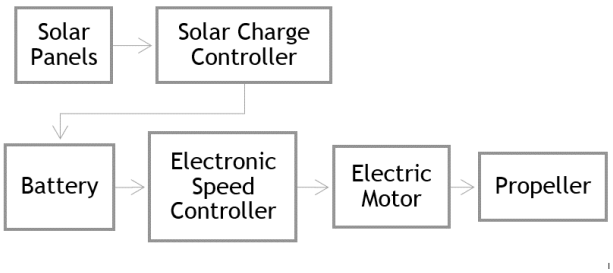

Figure 3-5 – LEEUAV's hybrid propulsive scheme

3.4. Current Work

Besides the aerodynamic analysis of the influence of the solar cells in the aerodynamic performance of the LEEUAV's airfoil, currently, a flight time estimation system based on the current available energy and actual consumption is being developed and all systems are being installed in the airplane to test their fidelity and to perform flight tests. These will give the chance to test the aircraft performance and compare it to the predictions obtained during the design.

This page has been intentionally left blank
for double side copying

Chapter 4

4. Concepts Identification and Problem Definition

This chapter serves to introduce the aerodynamic analysis. A detailed description of the Long Endurance Electric Unmanned Air Vehicle's (LEEUAV's) airfoil, the problem arising with placing the solar cells on its upper surface and the methodology that was used for the analysis are presented.

4.1. LEEUAV's Airfoil Description

As it was said before, a new airfoil was developed using an in-house gradient based aerodynamic shape optimization tool coupled with XFOIL, as the aerodynamic analysis tool.

Since the LEEUAV has a very low cruise speed, the airfoil demonstrates good performance at low Reynolds number (*Re*), since it is directly related with the velocity. It delivers minimum drag coefficient (C_d) in the lift coefficient (C_l) range from 0.6 to 1.5 and a maximum lift coefficient higher than 1.7. For good structural performance of the spar, the relative thickness is greater than 10% and to avoid damage during ground handling and facilitating the construction of the trailing edge elements, the trailing edge thickness is greater than 1 mm.

The solution is the airfoil presented in Figure 4-1 with a thickness-to-chord ratio of 12%.

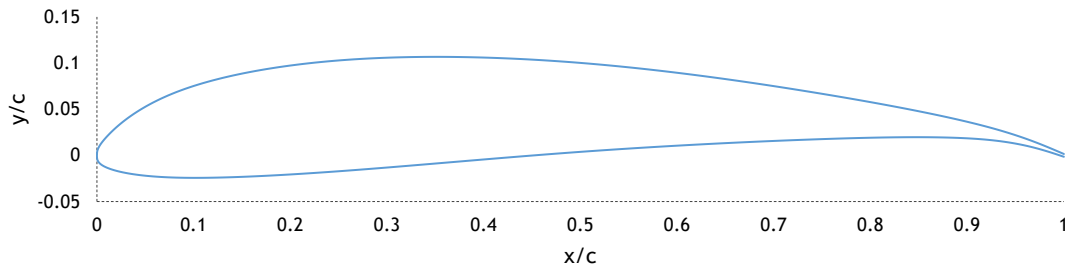

Figure 4-1 – LEEUAV's airfoil

To study the airfoil's performance, XFOIL was used, using an analysis where the parameters held constant are $Re\sqrt{C_l}$ and $M\sqrt{C_l}$, being *M* the Mach number. This corresponds to an aircraft in level flight at a given altitude undergoing trim speed changes. The LEEUAV's airfoil polar graphs, presented in Chart 4-1 and Chart 4-2, were calculated for $Re\sqrt{C_l}$ = 150,000, which corresponds to cruise altitude condition. The airfoil's most relevant performance characteristics are summarized in Table 4-1.

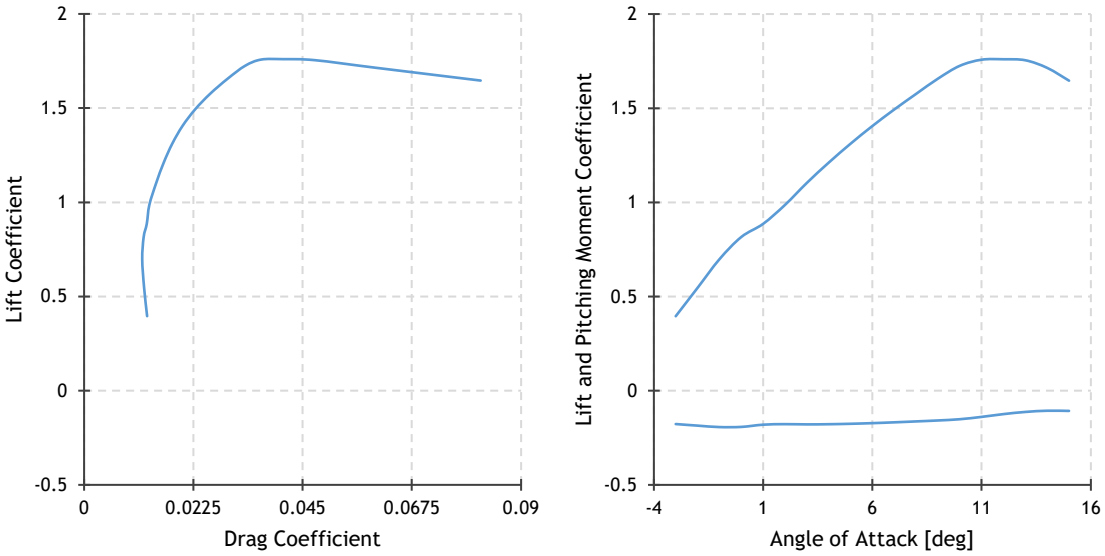

Chart 4-1 - LEEUAV's airfoil drag polar (on the left) and lift and pitching moment coefficient curve (on the right) for $Re\sqrt{C_l}$ = 150,000

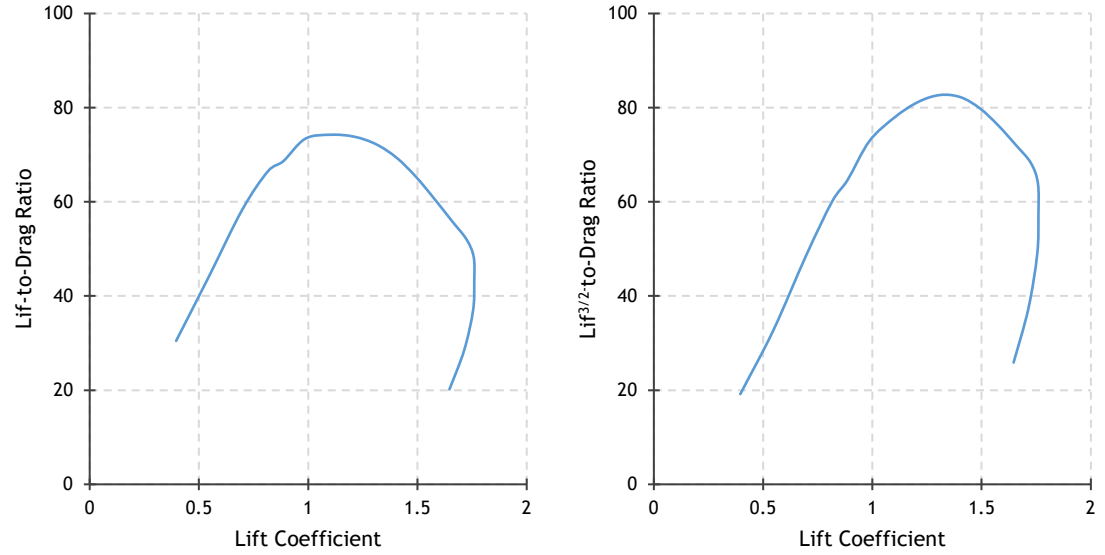

Chart 4-2 - LEEUAV's airfoil lift-to-drag ratio (on the left) and lift$^{3/2}$-to drag ratio (on the right) for $Re\sqrt{C_l}$ = 150,000

Table 4-1 - LEEUAV's airfoil aerodynamic performance

Maximum lift coefficient	$C_{l_{max}}$	1.76
Maximum lift angle of attack	$\alpha_{C_{l_{max}}}$	12 deg
Minimum drag coefficient	$C_{d_{min}}$	0.012
Lift coefficient of minimum drag coefficient	$C_{l_{C_{d_{min}}}}$	0.7
Angle of attack of minimum drag coefficient	$\alpha_{C_{d_{min}}}$	-1 deg

Maximum lift-to-drag ratio	$(C_l/C_d)_{max}$	74.25
Lift coefficient of maximum lift-to-drag ratio	$C_{l_{(C_l/C_d)_{max}}}$	1.10
Angle of attack of maximum lift-to-drag ratio	$\alpha_{(C_l/C_d)_{max}}$	3 deg
Maximum lift$^{3/2}$-to-drag ratio	$\left(C_l^{3/2}/C_d\right)_{max}$	82.70
Lift coefficient of maximum lift$^{3/2}$-to-drag ratio	$C_{l_{\left(C_l^{3/2}/C_d\right)_{max}}}$	1.31
Angle of attack of maximum lift$^{3/2}$-to-drag ratio	$\alpha_{\left(C_l^{3/2}/C_d\right)_{max}}$	5 deg

4.2. Problem Definition

Besides its aerodynamic purpose, the LEEUAV's wing must accommodate the solar cells on its upper surface. Since the solar cells have a finite thickness, they create a localized thickening or an offset in the airfoil, with a forward facing step (FFS) at the beginning of the solar cell array and a backward facing step (BFS) at its end. Moreover, the offset gives the airfoil an increment in camber and thickness. The offset is illustrated in Figure 4-2 and the steps are shown in detail in Figure 4-3.

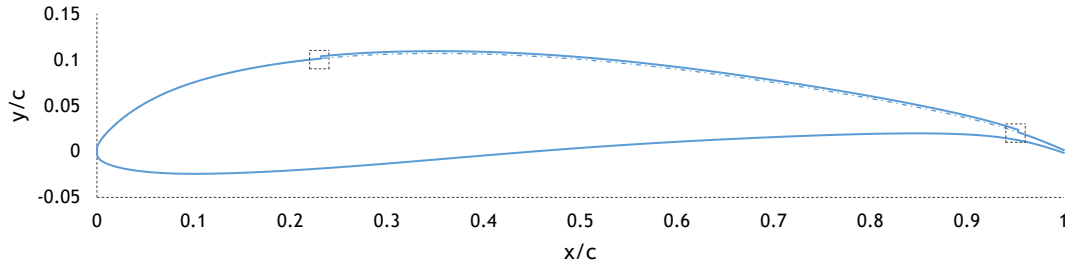

Figure 4-2 - LEEUAV's airfoil with solar panel on its upper surface

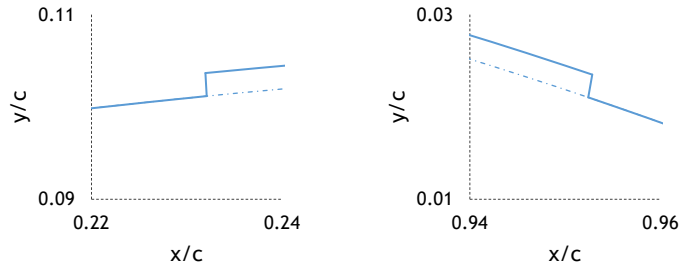

Figure 4-3 - FFS (on the left) and BFS (on the right) in detail

Given this condition, it is necessary to fully understand the influence of these steps on the airfoil performance and achieve the best position for placing the solar panels with the view to deliver the more approximated aerodynamic performance provided by the initial design.

4.3. Study Methodology

More specifically, the objective of the analysis is to understand and quantify the influence of these steps in the lift coefficient (C_l), drag coefficient (C_d), pitching moment coefficient (C_m), lift-to-drag ratio (C_l/C_d), lift$^{3/2}$-to-drag ratio ($C_l^{3/2}/C_d$) and transition point on the upper (x_{tr_u}/c) and lower (x_{tr_l}/c) surfaces, for $Re\sqrt{C_l}$ = 150,000, corresponding to cruise altitude conditions.

First, using XFOIL it is intended to obtain the following graphs:

- C_l *vs.* C_d
- C_l *vs.* α
- C_m *vs.* C_l
- $\frac{C_l}{C_d}$ *vs.* C_l
- $\frac{C_l^{3/2}}{C_d}$ *vs.* C_l
- C_l *vs.* $\frac{x_{tr_u}}{c}$
- C_l *vs.* $\frac{x_{tr_l}}{c}$

To compare with the performance of the clean airfoil, several airfoils must be created containing an offset. The beginning of the offset, the forward facing step, will have the designation of the offset initial position, $(x/c)_i$, and the end of the offset, the backward facing step, as the offset final position, $(x/c)_f$, and the offsets will have a thickness-to-chord ratio, (t/c). These parameters vary according to the intervals and increments in Table 4-2 and are illustrated in Figure 4-4.

Table 4-2 – Offset geometrical parameters

Parameter	Minimum	Maximum	Increment
$\left(\frac{x}{c}\right)_i$	0.10	0.50	0.05
$\left(\frac{x}{c}\right)_f$	0.30	0.95	0.05
$\left(\frac{t}{c}\right)$	0.0025	0.01	0.0025

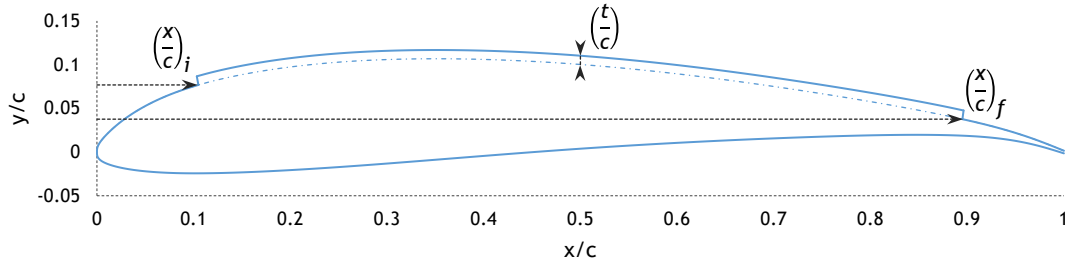

Figure 4-4 - Offset geometrical parameters

In the second part of the work is intended to *1)* choose a few of the solar panels positions analyzed in XFOIL, *2)* perform a computational fluid dynamic analysis using ANSYS Fluent to validate and refine the results obtained from XFOIL, *3)* visualize the airflow over the airfoil to better understand the influence of the solar panels in the airflow.

This page has been intentionally left blank
for double side copying

Chapter 5

5.XFOIL Numerical Analysis

In this chapter, the analysis performed with XFOIL is described, first, with a brief description of the XFOIL software, then, with an explanation of how the different airfoils with offsets were created, how the simulation procedure was performed and what were the analysis results. In the end, the conclusions drawn from it are summarized.

5.1. XFOIL Description

XFOIL is an interactive program for the analysis of subsonic isolated airfoils, and the first version was written by Mark Drela in 1986. The general methodology is described in reference [23].

The main objective of this program is to quickly predict the airfoil performance at low Reynolds numbers and its convergence is achieved through the iteration between the outer and inner flow solutions on the boundary layer displacement thickness. The XFOIL code combines a potential flow panel method and an integral boundary layer formulation for the analysis of flows around airfoils. It can calculate the viscous pressure distribution and capture the influence of limited trailing edge separation and laminar separation bubbles. [24]

XFOIL uses an approximate e^N envelope method to calculate transition. In the present work, N was set to default value of 9, which corresponds to a smooth wing surface in a low turbulence intensity freestream. With this method, the code tracks only the most amplified frequency at a given point on the airfoil downstream from the point of instability, to obtain the amplitude of that disturbance. Transition is assumed when this integrated amplitude reaches an empirically determined value. [24]

XFOIL offers three types of possible analysis, which allow the user to set the dependence of the Mach (M) and Reynolds number (Re) in relation to the lift coefficient (C_l). These are resumed in Table 5-1. In this work, type 2 analysis was used, which corresponds to an aircraft in level flight at a given altitude undergoing trim speed changes.

Table 5-1 - XFOIL analysis types

Type	Parameters held constant		Varying	Fixed
1	M	Re	Lift	Chord, velocity
2	$M\sqrt{C_l}$	$Re\sqrt{C_l}$	Velocity	Chord, lift
3	M	$Re\ C_l$	Chord	Lift, velocity

5.2. Numerical Procedure

The examination of the range of values of the offset geometrical parameters (the offset initial position, $(x/c)_i$, the offset final position, $(x/c)_f$, and the offset thickness-to-chord ratio, (t/c)), assuming that the offset final position must be greater than the initial position, gives a total of 444 combinations of offsets to create, analyze and compare. Since making and analyzing each option one by one would be unpractical, nor time efficient, the solution was to use scripts to automate the process, which are described in the next paragraphs.

5.2.1. Airfoils Conception

XFOIL reads labeled coordinate files, which contains a name string on the first line and bellow the x,y coordinates, which run from the trailing edge, round the leading edge, back to the trailing edge, in either direction.

The easiest and most efficient way of creating the different airfoils incorporated with offsets is to use Microsoft Excel. In its spreadsheet, the values for the offset parameters, $(x/c)_i$, $(x/c)_f$ and (t/c) are established, and, from there, the spreadsheet reads the Long Endurance Electric Unmanned Air Vehicle's (LEEUAV's) airfoil coordinates and identifies, in the upper surface, if the coordinates are between the initial and final limit of the offset. Then, it generates new coordinates, the ones that are inside the limits of the offset, adds an increment so that the spreadsheet creates the offset. The ones which are not within its limits remain the same as the original coordinates.

For data organization, each new airfoil receives the codename "LEEUAV ($(x/c)_i$; $(x/c)_f$; (t/c))", which identifies the offset position and thickness. An example with the offset between 0.20 and 0.60 of the chord and thickness-to-chord ratio of 0.005 is presented in Figure 5-1.

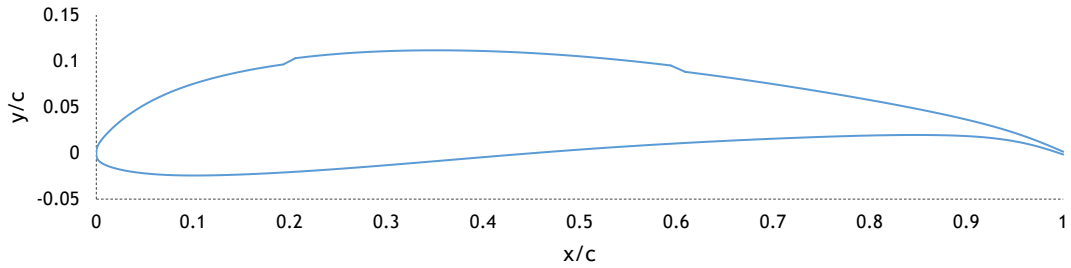

Figure 5-1 – LEEUAV (0.20;0.60;0.005)

With a script in Visual Basic for Applications, it was possible for Excel automatically combine every option of $(x/c)_i$, $(x/c)_f$ and (t/c), and for each combination, create and save the coordinates with the respective codename in a DAT file, so that could be subsequently analyzed by XFOIL.

The setback of this procedure is that the steps are not forming a 90-degree angle with the airfoil's upper surface, which under predicts the damage caused by the offset and for small thickness-to-chord ratio, the panel angle in the steps' location is so small that XFOIL may not assume it as a step, but only as an increase in thickness. On the other hand, a high panel angle induces in convergence problems and program errors in XFOIL, which are reflected in the offsets with greater thickness-to-chord ratio, as it is demonstrated ahead.

5.2.2. XFOIL Simulation Procedure

XFOIL has an user command line interface and it was automated with a Matlab script for the analysis procedure, thus running the simulation for the several airfoils. A viscous type 2 analysis for $Re\sqrt{C_l}$ = 150,000 was performed, for a range of angles of attack from -3 deg to 15 deg. Each analysis normally requires less than a minute of elapse time per polar on an average desktop computer, but for offsets with greater thickness-to-chord ratio, it takes much longer. The total analysis time, for all airfoils, was approximately 28 hours.

5.3. Results and Discussions

The most important points drawn from the analysis are presented next and it is critical to pay special attention to the design lift coefficient range from 0.6 to 1.5. Most of the results are presented for thickness-to-chord ratios equal to 0.005, since these are more visible, thus facilitating comprehension.

5.3.1. Excessive Thickness-to-Chord Ratio

Four thickness-to-chord ratios were analyzed, respectively 0.0025, 0.005, 0.0075 and 0.01. For the last two, XFOIL did not converge for every angle of attack, and, in some cases, the program even crashed. This may have been caused by the excessive panel angle in the steps' location, which, in some cases, reached 50 deg.

In Figure 5-2, the different four thickness-to-chord ratios are illustrated.

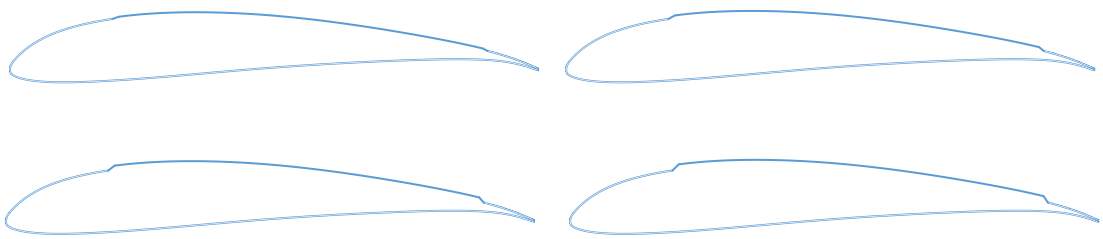

Figure 5-2 – Different thickness-to-chord ratios: (t/c) = 0.0025 (top left); 0.005 (top right); 0.0075 (bottom left); 0.01 (bottom right)

Only 68% and 24% of the offsets combinations with thickness-to-chord ratio equal to 0.0075 and 0.01, respectively converged with adequate polar points (40%), thus becoming extremely difficult to draw conclusions. In Chart 5-1, the C_l/C_d and $C_l^{3/2}/C_d$ curves for the clean airfoil and for offsets combinations with different thickness-to-chord ratios are presented. It is evident that there is a huge lack of polar points for the two greater thickness-to-chord ratios.

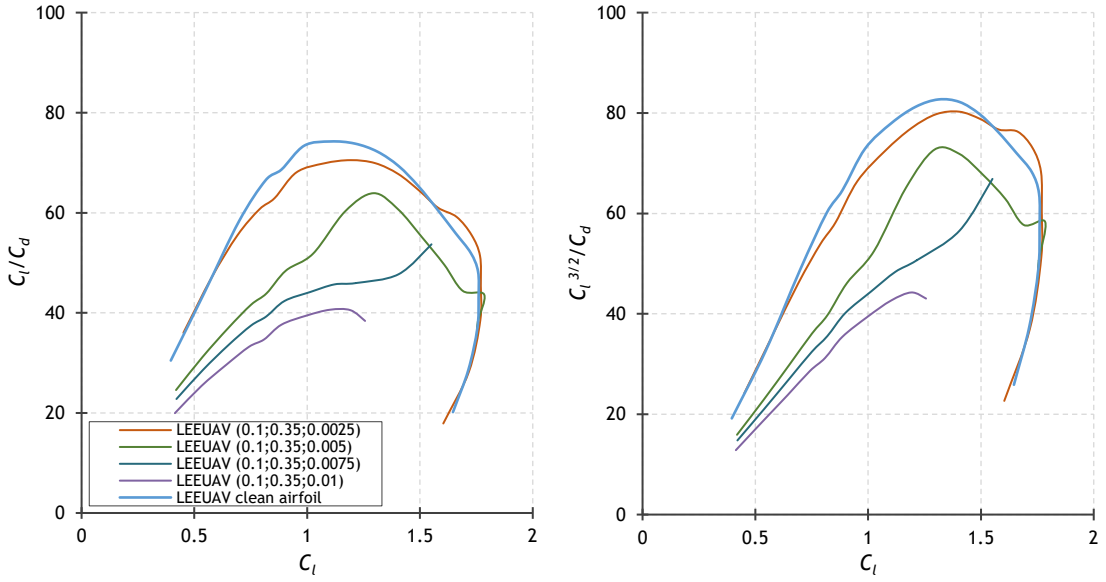

Chart 5-1 - C_l/C_d (on the left) and $C_l^{3/2}/C_d$ (on the right) at $Re\sqrt{C_l}$ = 150,000 for the LEEUAV's clean airfoil and for different offset combinations with different thickness-to-chord ratios

Nevertheless, it clearly shows that the greater thickness-to-chord ratios are extremely prejudicial to the airfoil performance, with increases of up to 80-85% of drag coefficient in the design lift coefficient range from 0.6 to 1.5, and losses of 20-25% of lift coefficient compared to the clean airfoil. It is clear that the influence in the airfoil performance is proportional to the increase in thickness-to-chord ratio of the offset.

5.3.2. Premature Forced Transition

When analyzing the results, one position pops out from the others in any thickness-to-chord ratio: the offset initial position at 0.10 of the airfoil's chord (Figure 5-3), that is, the forward facing step positioned at 10% of the airfoil's chord. In Chart 5-2, an example with offsets with various initial positions and the same final position at 0.95 of the chord is presented.

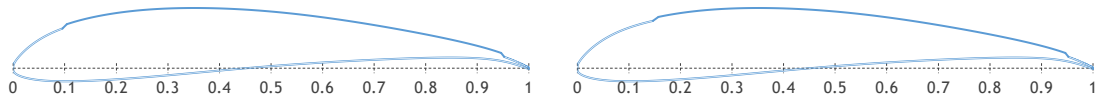

Figure 5-3 – LEEUAV (0.10;0.95;0.005) (on the left) and LEEUAV (0.15;0.95;0.005) (on the right)

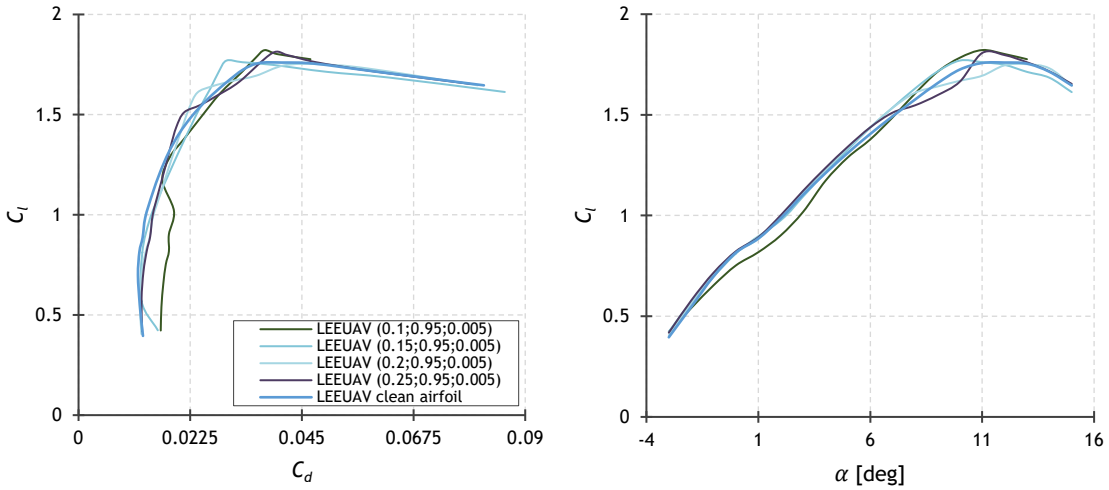

Chart 5-2 - Drag polar (on the left) and lift coefficient curve (on the right) at $Re\sqrt{C_l}$ = 150,000 for the LEEUAV's clean airfoil and for different offset combinations with (t/c) = 0.005

Observing the drag polar and lift coefficient curve, it is evident that the offset initial position at 0.10 of the chord, for lift coefficients lower than 1.2, stands out from the others, with increase in the drag coefficient and decrease in the lift coefficient. The offset initial position at 0.15 of the chord (Figure 5-3) also shows increase in the drag coefficient, but only for lift coefficients lower than 0.6.

The reason for this discrepancy, seen in Chart 5-3, is due to the forward facing step forcing the transition of the flow in the upper surface from laminar to turbulent, shortly after the step's location for low lift coefficients, which corresponds to higher speeds. In the lower surface, the influence of the offset is negligible, yet noticeable.

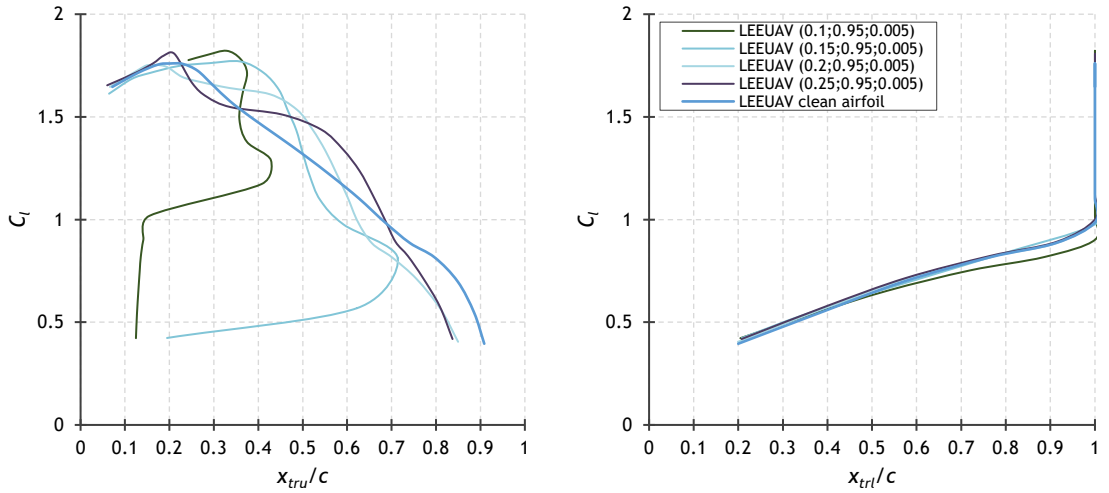

Chart 5-3 - Transition point on the upper (on the left) and lower (on the right) surface at $Re\sqrt{C_l}$ = 150,000 for the LEEUAV's clean airfoil and for different offset combinations with (t/c) = 0.005

In Chart 5-4, a comparison between the pressure coefficient distribution about the airfoil for the LEEUAV clean airfoil and for the LEEUAV (0.10;0.95;0.005) is presented. The "x" represents the transition point.

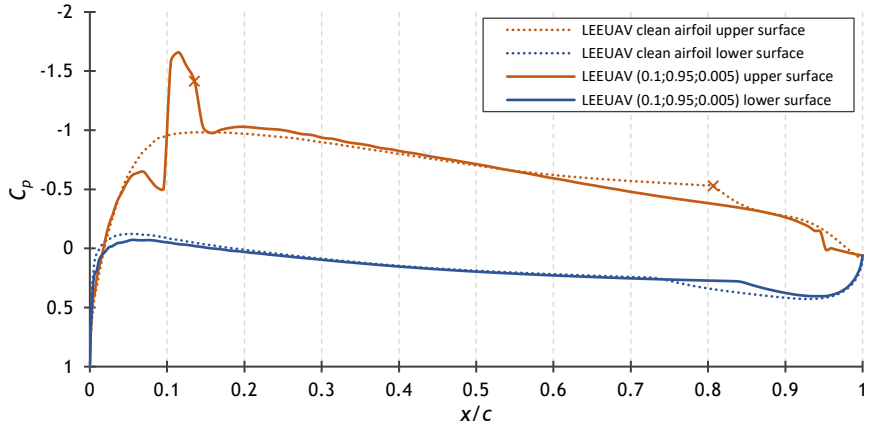

Chart 5-4 - Pressure coefficient distribution at $Re\sqrt{C_l}$ = 150,000 for C_l = 0.8 for the LEEUAV clean airfoil and for the LEEUAV (0.10;0.95;0.005)

Regarding the upper surface, the pressure field experiences the normal drop at the leading edge due to the acceleration of the fluid over the airfoil's curvature. As referred in section "2.2. Effects of Steps", there is a separation upstream and downstream of the forward facing step. Upstream of the step, there is an adverse pressure gradient which causes separation, and in the step location, originated by the acceleration of the fluid over the step, occurs a large decrease in the pressure field, followed downstream by a severe adverse pressure gradient which causes separation and transition of the flow.

Concerning the backward facing step, it is visible that after the step, separation occurs through the adverse pressure gradient. When the flow travels past the backward facing step, it creates a low-pressure recirculation zone and the sudden reduction in the airfoil thickness after the step, relatively decreases the flow velocity, which results in a subsequent high pressure region stretched to the trailing edge of the airfoil.

5.3.3. Forward Facing Step Too Far Behind

Another set of offset initial positions that also severely damage the performance at low lift coefficients, are the offsets beginning after 0.30 of the chord (Figure 5-4).

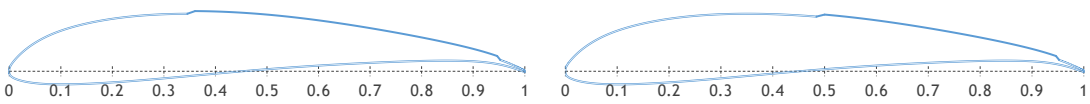

Figure 5-4 - LEEUAV (0.35;0.95;0.005) (on the left) and LEEUAV (0.50;0.95;0.005) (on the right)

The drag polar and lift coefficient curve seen in Chart 5-5 are related to offsets with initial positions after 0.30 of the chord and with the same final position. These affect the performance for lift coefficients below 1, correspondent to higher speeds, and the effects increase as the offset initial position moves further away from the leading edge.

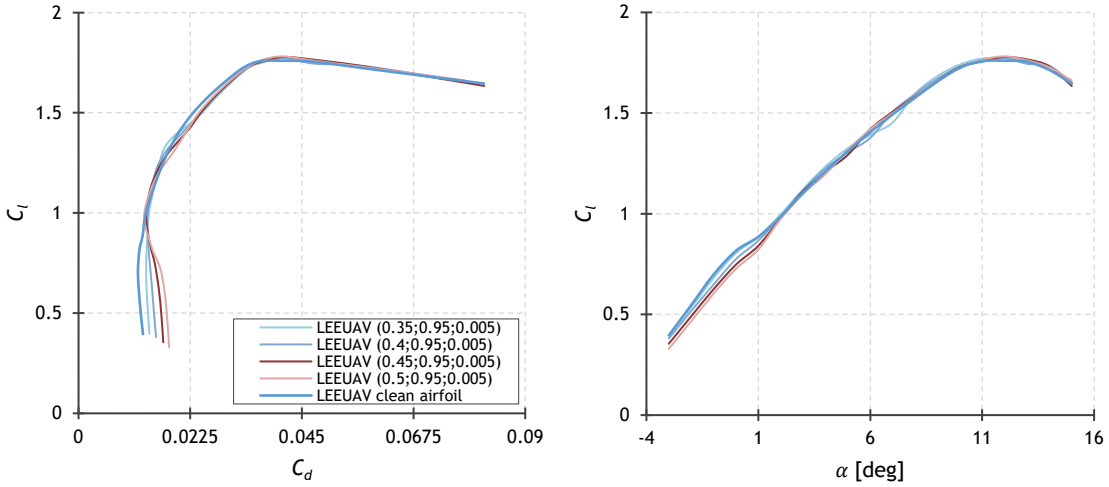

Chart 5-5 - Drag polar (on the left) and lift coefficient curve (on the right) at $Re\sqrt{C_l}$ = 150,000 for the LEEUAV's clean airfoil and for different offset combinations with (t/c) = 0.005

The reason for this divergence is not so obvious observing the pressure coefficient distribution over the airfoil in Chart 5-6, where the comparison of the pressure coefficient distribution for the clean airfoil and for an airfoil with an offset beginning at 0.50 of the airfoil's chord is presented. The forward facing step, the beginning of the offset, is positioned in a region where the pressure coefficient is almost constant and does not cause transition.

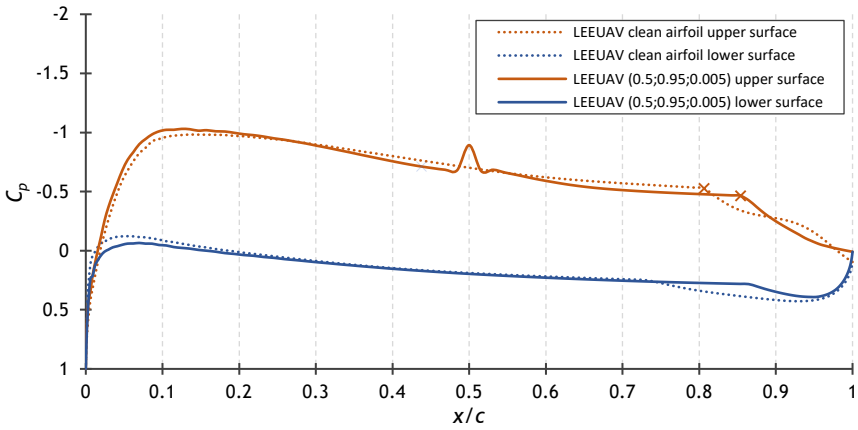

Chart 5-6 - Pressure coefficient distribution at $Re\sqrt{C_l}$ = 150,000 for C_l = 0.8 for the LEEUAV clean airfoil and for the LEEUAV (0.50;0.95;0.005)

The drag coefficient can be decomposed into its mains components, namely the pressure drag coefficient (already referred) and the skin friction drag coefficient. In Chart 5-7, a comparison of the skin friction coefficient distribution over the upper surface between the clean airfoil and the LEEUAV (0.50;0.95;0.005), is presented. The clean airfoil and the airfoil with the offset beginning at 0.50 of the chord exhibit similar skin friction coefficient until around 0.30 of the chord. Upstream of the forward facing step, for the airfoil with offset, the skin friction coefficient drops to zero in the separation point and is followed by a concaved down curve confining the recirculation zone. In the step's location, the skin friction coefficient increases exponentially, originating a high skin friction coefficient zone, which increases the total drag coefficient in relation to the clean airfoil.

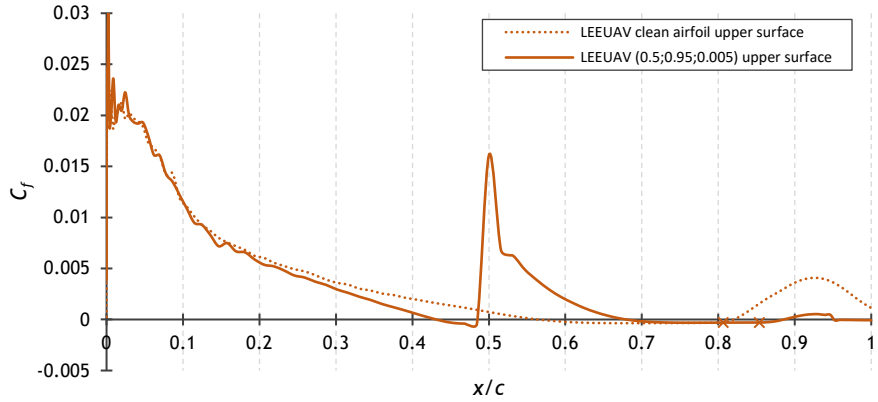

Chart 5-7 - Skin friction coefficient distribution on the upper surface at $Re\sqrt{C_l}$ = 150,000 for C_l = 0.8 for the LEEUAV clean airfoil and for the LEEUAV (0.50;0.95;0.005)

5.3.4. Backward Facing Step Influence

The offset final position does not have significant impact on the airfoil performance, when compared to the initial position. Nevertheless, the offset final position still has some degrading performance positions, where the backward facing step forces the transition of the flow in the upper surface from laminar to turbulent. This is regarding to the offset final positions prior to 0.80 of the airfoil's chord (Figure 5-5).

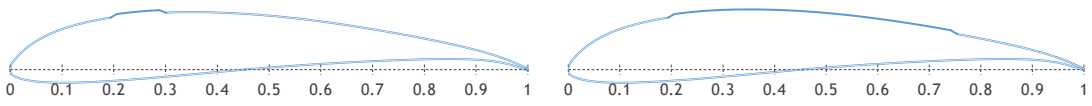

Figure 5-5 - LEEUAV (0.20;0.30;0.005) (on the left) and LEEUAV (0.20;0.75;0.005) (on the right)

When transition occurs, there is an increase in drag coefficient translated in a decrease of C_l/C_d and $C_l^{3/2}/C_d$. In Chart 5-8, is demonstrated a comparison of the curve for the clean airfoil and the curves for airfoils with the same offset initial position, but with different final positions between 0.30 and 0.70 of the chord.

There is a clear decrease in C_l/C_d and $C_l^{3/2}/C_d$, which extends to higher lift coefficients, when the offset final position is further away from the trailing edge.

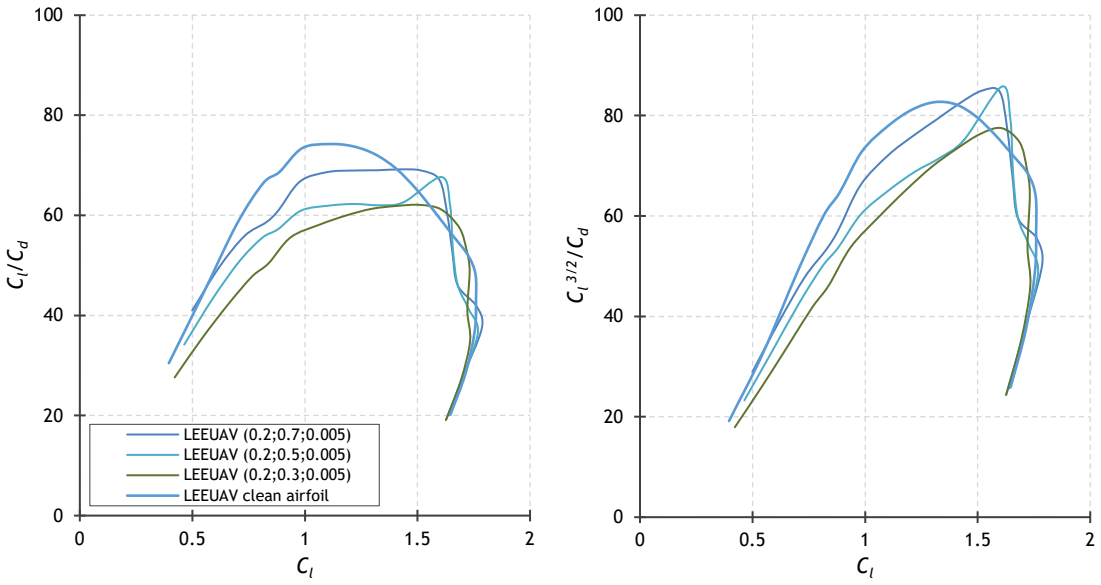

Chart 5-8 - C_l/C_d (on the left) and $C_l^{3/2}/C_d$ (on the right) at $Re\sqrt{C_l}$ = 150,000 for the LEEUAV's clean airfoil and for different offset combinations with (t/c) = 0.005

The reason for this is clearly shown in Chart 5-9, the transition point versus lift coefficient chart. It shows that the further away from the trailing edge the offset final position is, the sooner transition occurs. Once again, in the lower surface, the influence of the offset is negligible.

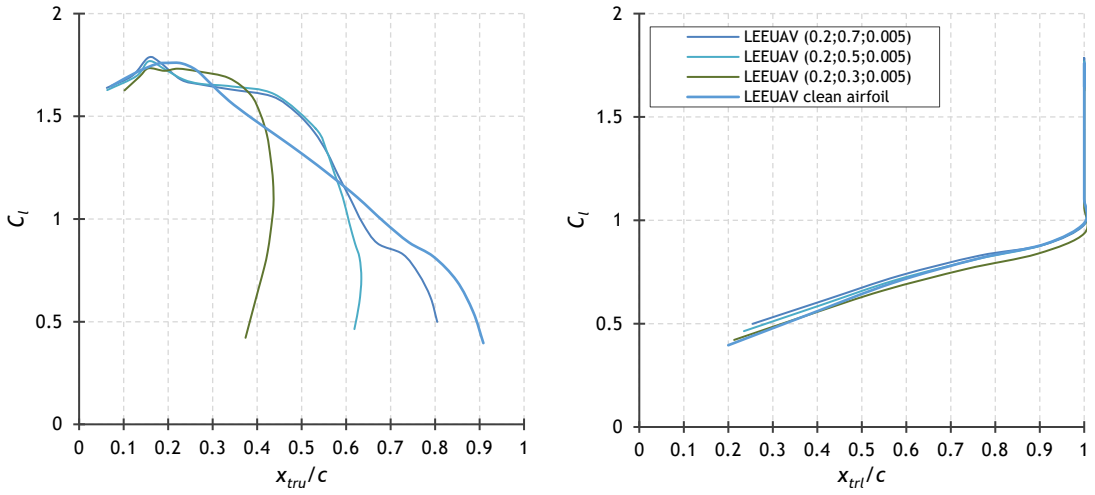

Chart 5-9 - Transition point on the upper (on the left) and lower (on the right) surface at $Re\sqrt{C_l}$ = 150,000 for the LEEUAV's clean airfoil and for different offset combinations with (t/c) = 0.005

In Chart 5-10, a comparison between the pressure coefficient distribution over the airfoil of the LEEUAV clean airfoil and of the airfoil with the offset final position too far ahead, at 0.40 of the airfoil's chord, is presented. The effects of the backward facing step in the pressure coefficient are not very noticeable, but after the backward facing step location, the pressure coefficient remains constant, caused by a laminar separation bubble, and, then, flow transition occurs.

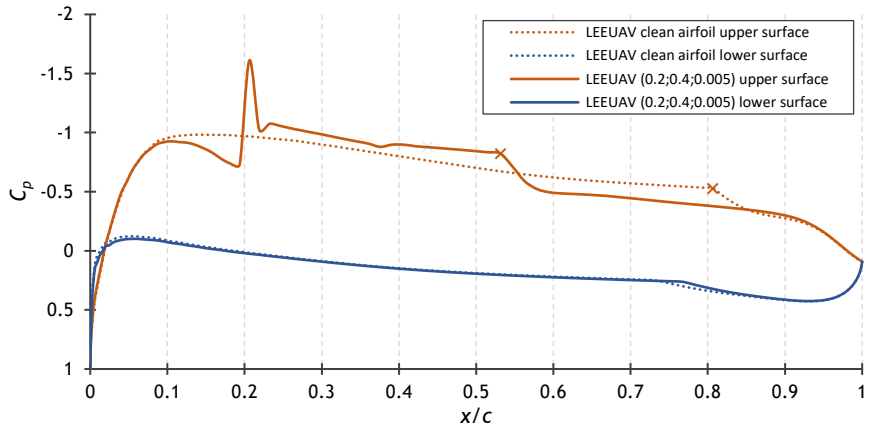

Chart 5-10 - Pressure coefficient distribution at $Re\sqrt{C_l}$ = 150,000 for C_l = 0.8 for the LEEUAV clean airfoil and for the LEEUAV (0.20;0.40;0.005)

The remaining positions for the offset final position, between 0.80 and 0.95 of the airfoil's chord (Figure 5-6), deliver the best performance with minor differences between them. That difference is lower than 1% for high lift coefficients (>1.5). When comparing to the influence of the offset initial position, the influence of the offset final positions is negligible.

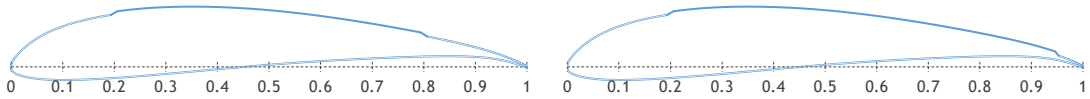

Figure 5-6 - LEEUAV (0.20;0.80;0.005) (on the left) and LEEUAV (0.20;0.95;0.005) (on the right)

In Chart 5-11, the C_l/C_d is presented, on the left, for airfoils with different offsets final positions and the same initial position, and, on the right, for airfoils with different offsets initial positions and the same final position.

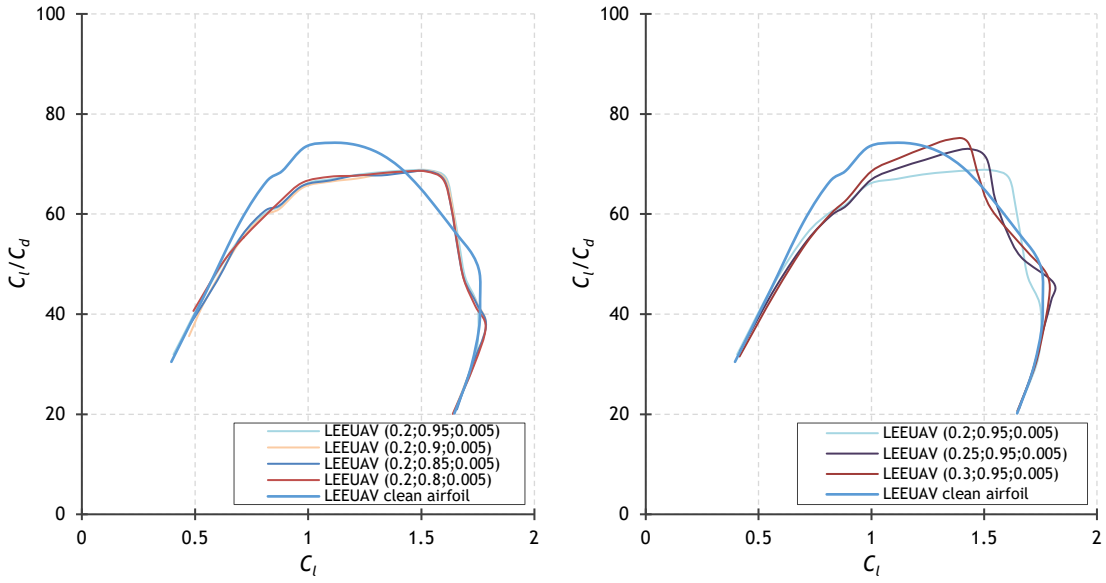

Chart 5-11 - C_l/C_d at $Re\sqrt{C_l}$ = 150,000 for the LEEUAV's clean airfoil and for different offset combinations with (t/c) = 0.005

Chart 5-11 clearly shows that the difference in performance is really caused by the offset initial position, and not its final position. However, the variation of the C_l/C_d by the airfoils with offsets can be distinguished in two regions: for lift coefficients above 1.5, in which there is nearly no difference between them; and for lift coefficient below 1.5, where the offset final position closest to the trailing edge delivers the poorest C_l/C_d. There is an exception for the final position at 0.95, where the C_l/C_d rises and shows similar performance to the one positioned at 0.80 of the chord.

5.3.5. Forward Facing Step Effects

The offset initial position between 0.20 and 0.30 of the airfoil's chord (Figure 5-7) delivers the best performance within the damage and presents similar maximum differences for each aerodynamic coefficient that are explained ahead. For each aerodynamic coefficient, the polar graph is presented, accompanied with a chart showing the differences. These differences, presented in percentage, are between the aerodynamic coefficient of the clean airfoil and those of the airfoils incorporated with offsets.

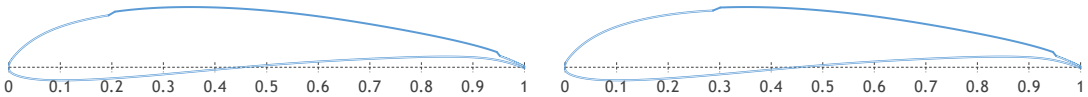

Figure 5-7 - LEEUAV (0.20;0.95;0.005) (on the left) and LEEUAV (0.30;0.95;0.005) (on the right)

For these positions, the effects related with the increase in airfoil thickness and camber are evident. In Table 5-2, the airfoils geometric characteristics regarding thickness and camber for two thickness-to-chord ratios are presented. The offset gives an increase in thickness and camber, proportional to the offset thickness-to-chord ratio, which has the associated effects described in section "2.2.3. Increase in Camber and Thickness". The offset beginning at 0.30 of the chord has different thickness than at 0.20 and 0.25, and this is visible in the polar graphs, where the curve of the offset initial position at 0.30 of the chord does not follow the trend and swaps with the lift coefficient and pitching moment coefficient curve of the offset with initial position at 0.25. This is demonstrated ahead.

Table 5-2 – Airfoils geometric characteristics

LEEUAV's airfoils			Thickness [%]	Camber [%]
Clean airfoil			12	5.2
$(x/c)_i$	$(x/c)_f$	(t/c)		
0.20	0.95	0.0025	12.25	5.33
0.25				
0.30			12.13	
0.20	0.95	0.005	12.5	5.45
0.25				
0.30			12.39	

In regard of the drag coefficient, which is the most affected aerodynamic coefficient, the polar curve moves upward and to the right, due to the increase in camber and thickness [17], thus, showing ranges of lift coefficient where the drag coefficient is lower than the one regarding to the clean airfoil. In relation to the thickness-to-chord ratio equal to 0.005, in Chart 5-12, there is a visible increase in the drag coefficient, but smaller than 15%.

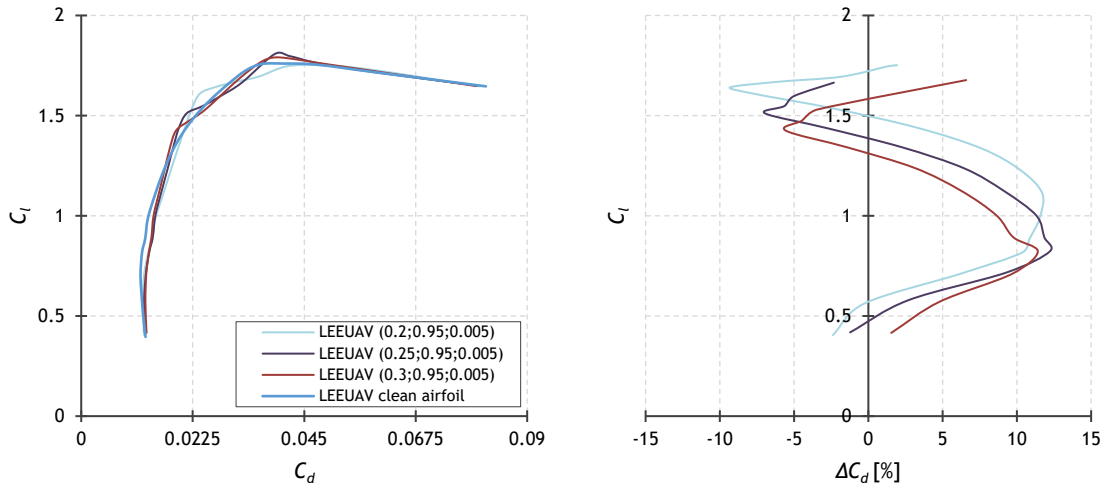

Chart 5-12 - Drag polar at $Re\sqrt{C_l}$ = 150,000 for the LEEUAV's clean airfoil and for different offset combinations with (t/c) = 0.005 (on the left) and its corresponding differences (on the right)

The variation of the drag coefficient by the airfoils incorporated with offsets can be divided in four regions, within the lift coefficient, that vary according to the thickness-to-chord ratio of the offset:

- C_l > ~ 1.5, where the $(x/c)_i$ furthest away from the leading edge increases drag coefficient;
- ~ 0.8-1.2 < C_l < ~ 1.5, where the $(x/c)_i$ closest to the leading edge increases drag coefficient (this C_l bottom limit tends to increase with the decrease of the thickness-to-chord ratio);
- ~ 0.3-0.7 < C_l < ~ 0.8-1.2, where the $(x/c)_i$ furthest away from the leading edge increases drag coefficient (this C_l limits tend to increase with the decrease of the thickness-to-chord ratio);
- C_l < ~ 0.3-0.7, where the $(x/c)_i$ closest to the leading edge increases drag coefficient (not visible in this thickness-to-chord ratio).

Concerning lift coefficient, in Chart 5-13, the linear portion of the lift coefficient curve moves to the left, due to the increase in camber [17]. The variation is not significant, around 5%, and it shows ranges of angles of attack with an increase in the lift coefficient, compared to the clean airfoil, due to the increase in camber.

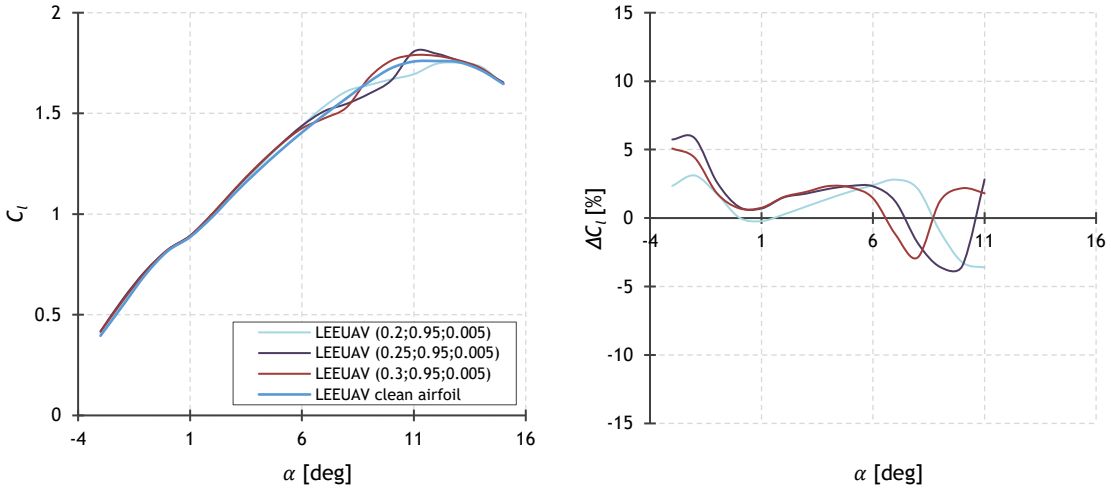

Chart 5-13 - Lift coefficient curve at $Re\sqrt{C_l}$ = 150,000 for the LEEUAV's clean airfoil and for different offset combinations with (t/c) = 0.005 (on the left) and its corresponding differences (on the right)

The difference in the lift coefficient can be divided into two regions within the range of angles of attack:

- α > ~ 6 deg, where the $(x/c)_i$ furthest away from the leading edge decreases lift coefficient (with oscillation close to α = 8 deg);

- α < ~ 6 deg, where the $(x/c)_i$ closest to the leading edge decreases lift coefficient (a mix-up is visible between the offset initial position at 0.25 and 0.30 of the chord, caused by a small difference in airfoil thickness).

The influence in the maximum lift coefficient does not present great variation in the absolute value, less than 2.4%, never being lower than 1.7. The maximum angle of attack also does not change significantly, with a difference always lower than 1 deg.

The pitching moment coefficient, in Chart 5-14, is also less affected by the presence of the offset, but slightly more affected than the lift coefficient, presenting a variation lower than 10%. The pitching moment coefficient curve moves downwards due to the increase in lift.

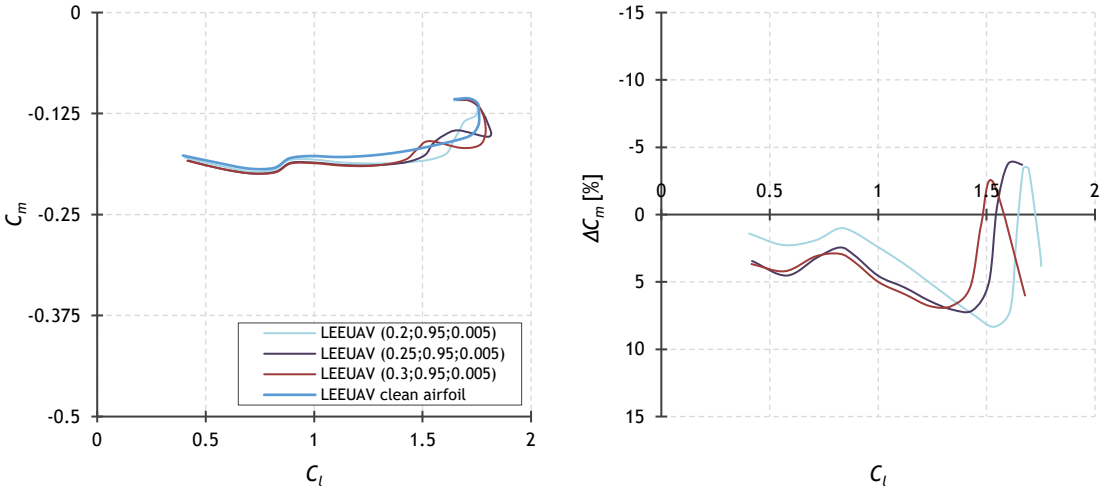

Chart 5-14 – Pitching moment coefficient curve at $Re\sqrt{C_l}$ = 150,000 for the LEEUAV's clean airfoil and for different offset combinations with (t/c) = 0.005 (on the left) and its corresponding differences (on the right)

The discrepancy in the pitching moment coefficient can be divided in two regions within the lift coefficient, identical to the discrepancy of the lift coefficient and with the same relationship with the offset initial position. The variation in this aerodynamic coefficient does not have great influence in the overall performance, being the drag and lift coefficients much more significant. Hereupon, the pitching moment coefficient should not have great influence in the decision of the best positions for placing the offset.

Concerning C_l/C_d, in Chart 5-15, and $C_l^{3/2}/C_d$, both have similar tendency, so they can be grouped together. Basically, moving the $(x/c)_i$ closest to the leading edge, the curve rotates clockwise, existing lift coefficient regions where the ratio is higher than the one for the clean airfoil. The predominating effects are the ones found in the drag coefficient, proving that the drag coefficient is the aerodynamic coefficient most affected by the offsets presence.

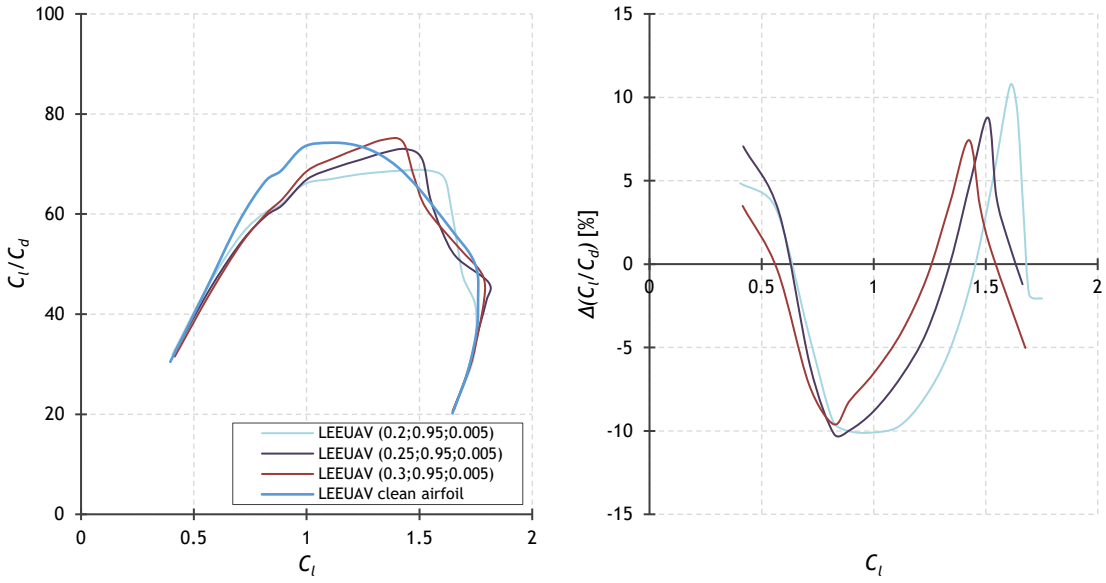

Chart 5-15 - C_l/C_d at $Re\sqrt{C_l}$ = 150,000 for the LEEUAV's clean airfoil and for different offset combinations with (t/c) = 0.005 (on the left) and its corresponding differences (on the right)

The variation of these performance ratios by the airfoils with offsets can be divided in four regions within the lift coefficient, that vary according to the thickness-to-chord ratio of the offset, identical to the variation in the drag coefficient:

- C_l > ~ 1.5, where the $(x/c)_i$ furthest away from the leading edge decreases C_l/C_d;
- ~ 0.8-1.2 < C_l < ~ 1.5, where the $(x/c)_i$ closest to the leading edge decreases C_l/C_d (this C_l bottom limit tends to increase with the decrease of the thickness-to-chord ratio);
- ~ 0.3-0.7 < C_l < ~ 0.8-1.2, where the $(x/c)_i$ furthest away from the leading edge decreases C_l/C_d (this C_l limits tend to increase with the decrease of the thickness-to-chord ratio);
- C_l < ~ 0.3-0.7, where the $(x/c)_i$ closest to the leading edge decreases C_l/C_d (not visible in this thickness-to-chord ratio).

5.3.6. LEEUAV's Solar Cells

Now that the general conclusions about offsets on the upper surface of the LEEUAV's airfoil have been drawn, a comparison between the possible best positions with the precise thickness of the solar cells is presented. Initially, this analysis was not intended to be performed, but the variation in the lift coefficient range of the aerodynamic coefficients vary substantially according to the thickness-to-chord ratio, thus being important to analyze the exact thickness.

The solar cells best possible positions will be between 0.20 and 0.25 of the airfoil's chord. For the most important aerodynamic coefficient, the polar graph and the differences chart are presented. These differences, as seen before, are presented in percentage and relate to the

difference in the aerodynamic coefficient compared to the clean airfoil. The design lift coefficient limits are showed in dashed lines.

The problem with this magnitude of thickness-to-chord ratio (0.001), as seen in Figure 5-8, is that the panel angle is very reduced in the step's location, resulting in less precise results. The main objective in this part of the work is to determine the best position to place the solar panels and not so important the value of the influence, regarding the clean airfoil, because this value will be "corrupted" by the reduced panel angle in the step's location.

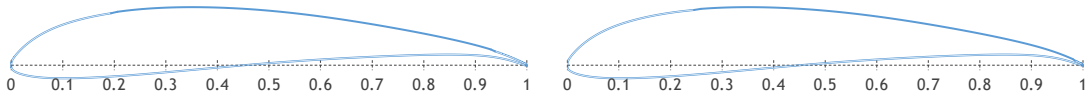

Figure 5-8 - LEEUAV (0.20;0.931;0.001) (on the left) and LEEUAV (0.25;0.981;0.001) (on the right)

The most important lift coefficient range of operation for the LEEUAV is the design lift coefficient range from 0.6 to 1.5, and particularly from 0.6 to 1. Below that, it is also important to have a good performance, due to the maximum speed, and the least important range is the lift coefficient above 1.5. Moreover, the maximum lift coefficient variation is negligible, so the effects above 1.5 are omitted. It is more important to ensure that the drag coefficient is minimum.

Regarding the drag coefficient, in Chart 5-16, its variation by the airfoils incorporated with offsets can be divided in three important regions within the lift coefficient:

- Lower speeds: ~ 1.2 < C_l < ~ 1.5, where the $(x/c)_i$ closest to the leading edge increases drag coefficient;
- Medium speed: ~ 0.7 < C_l < ~ 1.2, where the $(x/c)_i$ furthest away from the leading edge increases drag coefficient;
- Higher speed: C_l < ~ 0.7, where the $(x/c)_i$ closest to the leading edge increases drag coefficient.

The biggest variation between positions is for higher and medium speeds. So, the extreme positions should be put apart, since they exhibit the highest drag coefficient in higher or medium speeds. More specifically, the offset beginning at 0.25 of the airfoil's chord presents greatest drag coefficient in almost all the design lift coefficient, and for the offset beginning at 0.20, there is a rapid increase of drag coefficient for lower lift coefficient, which will correspond to maximum speed, hereupon these two positions will be omitted.

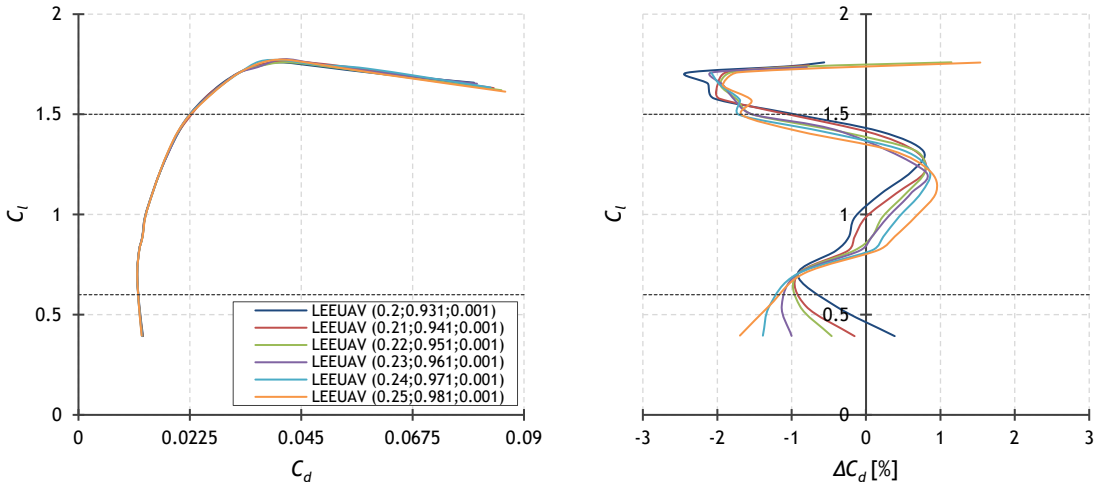

Chart 5-16 - Drag polar at $Re\sqrt{C_l}$ = 150,000 for the LEEUAV's clean airfoil and for different offset positions with similar characteristics as the solar cells (on the left) and its corresponding differences (on the right)

In respect to the lift coefficient, in Chart 5-17, the variation is minimal, and the difference in the lift coefficient only has one important region:

- Lower, medium, and higher speeds: α < ~ 6 deg, where the $(x/c)_i$ closest to the leading edge decreases lift coefficient.

For this coefficient, the best position is the one furthest from the leading edge, but with very little difference between them, reinforcing that the decision for the best position should be taken based on the drag coefficient performance.

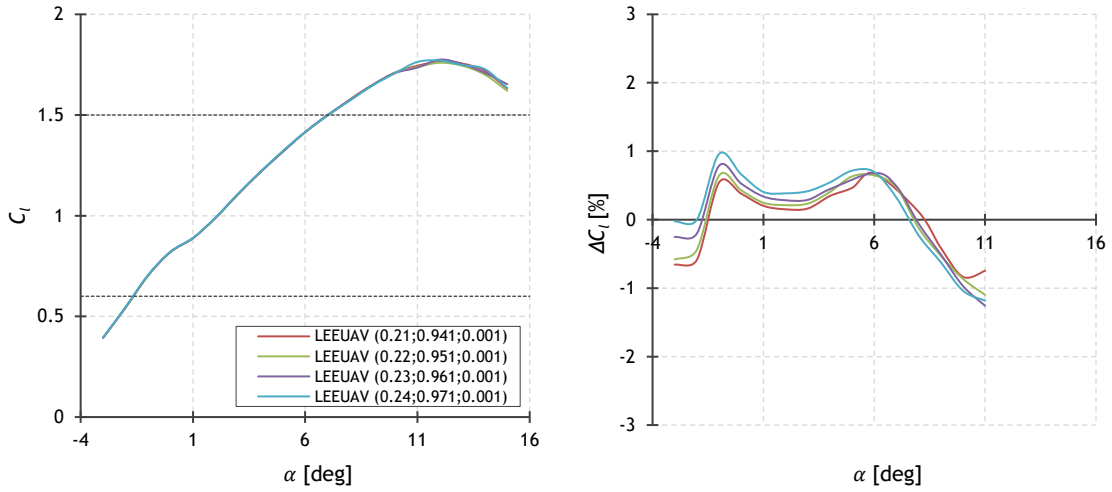

Chart 5-17 – Lift coefficient curve at $Re\sqrt{C_l}$ = 150,000 for the LEEUAV's clean airfoil and for different offset positions with similar characteristics as the solar cells (on the left) and its corresponding differences (on the right)

The C_l/C_d, in Chart 5-18, can be divided in three important regions within the lift coefficient similar to the drag coefficient:

- Lower speeds: ~ 1.2 < C_l < ~ 1.5, where the $(x/c)_i$ closest to the leading edge decreases C_l/C_d;
- Medium speed: ~ 0.7 < C_l < 1.2, where the $(x/c)_i$ furthest away from the leading edge decreases C_l/C_d;
- Higher speed: C_l < ~ 0.7, where the $(x/c)_i$ closest to the leading edge decreases C_l/C_d.

It is not visible which positions are worst, but the larger variation between them is for lift coefficients lower than 0.7, where the position at 0.24 of the chord shows best C_l/C_d. But positioning the offset at 0.24 of the chord has, as consequence, the final offset position at 0.971 of the chord, where it demonstrates a high curvature in the trailing edge of the airfoil. In the region around C_l = 1, the mid lift coefficient of the design range, the best position is the offset initial position at 0.21 of the chord, that exhibits best C_l/C_d performance.

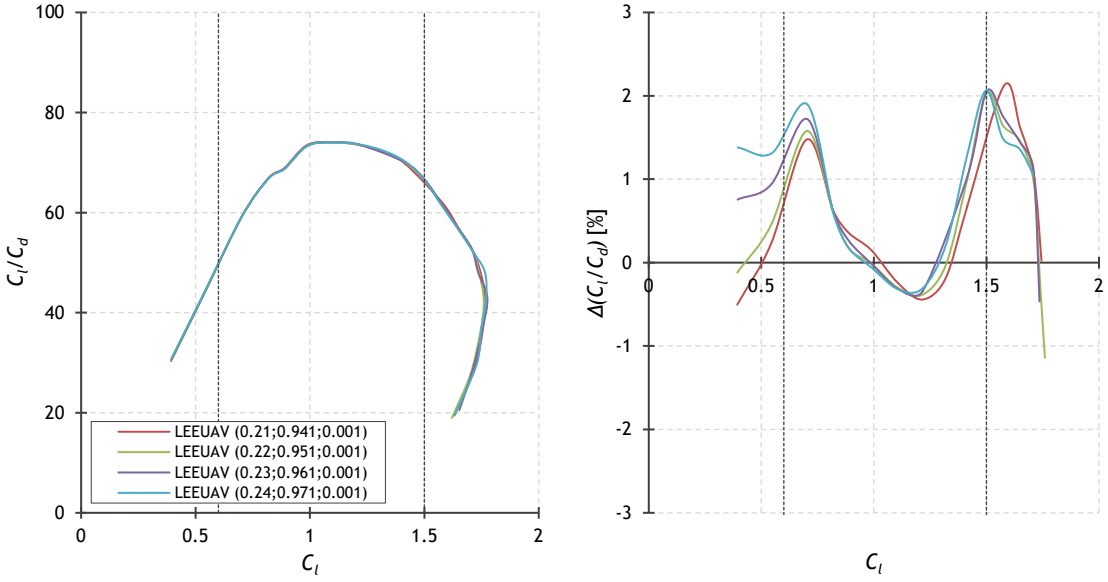

Chart 5-18 – C_l/C_d curve at $Re\sqrt{C_l}$ = 150,000 for the LEEUAV's clean airfoil and for different offset positions with similar characteristics as the solar cells (on the left) and its corresponding differences (on the right)

5.4. Conclusions

This numerical analysis using XFOIL, despite its limitations, has given the chance to understand the influence of having an offset on the upper surface of a low speed airfoil, as well as seeing how the performance varies according to the offset initial and final position and to the thickness-to-chord ratio. Next are summarized the conclusions drawn, organized by topic.

The increase in drag coefficient and decrease in lift coefficient presented are connected to the offset thickness-to-chord ratio equal to 0.005, in exception from the first topic, and are related to the clean airfoil performance.

5.4.1. Thickness-to-Chord Ratio

- The effects of the presence of the offsets are aggravated with the increase in thickness-to-chord ratio;
- As for the step geometry, as thickness-to-chord grows, the analysis viability of the step influence by XFOIL increases;
- For thickness-to-chord ratio higher than 0.005 the effects are too severe, and if the solar panel would present such magnitude of thickness-to-chord ratio, it would be of extremely importance to install them inside the wing (Drag coefficient increase: 80-85%; Lift coefficient decrease: 20-25%).

5.4.2. Offset Initial Position (Forward Facing Step)

- Having the beginning of the offset too close to the leading edge, respectively the offset initial position before 0.20 of the airfoil's chord, causes forced transition of the flow, at low lift coefficients, resulting in a severe increase in drag coefficient (Drag coefficient increase: 35-50%; Lift coefficient decrease: 5-10%);
- Also, having the offset too far behind in the airfoil, the initial positions after 0.30 of the chord, has great penalties regarding performances at low lift coefficients. It increases skin friction drag coefficient resulting in a total increase in drag coefficient (Drag coefficient increase: 25-50%; Lift coefficient decrease: 5-15%);
- The offset initial positions before 0.20 of the chord and after 0.30 deliver the worst performance for low lift coefficients. This is extremely harmful because the drag coefficient increase would not give the desired endurance, nor the maximum speed, nor the required power to do so.

5.4.3. Offset Final Position (Backward Facing Step)

- The offset final position placed before 0.80 of the chord causes perturbation on the flow over the upper surface, which results in transition soon after and consequently increases the drag coefficient (Drag coefficient increase: 15-35%; Lift coefficient decrease: 5%);
- Placing the offset final position between 0.80 and 0.95 of the chord gives the best result, with very similar results;
- The offset final position has minor effect when compared to the offset initial position, hereupon the most important is the position of the forward facing step.

5.4.4. Moving the Offset

- The best position for placing the offset is between 0.20 and 0.30 of the airfoil's chord and every aerodynamic coefficient presents one best position and, in some cases, a best position for each flight speed;
- The drag coefficient is the aerodynamic coefficient with most impact and does not have a best position for every lift coefficient range (Drag coefficient increase lower than 15%);
- The lift coefficient presents best results for offsets further away from the leading edge for the majority of range of angles of attack, and the maximum lift coefficient does not have significant impact (Lift coefficient decrease lower than 5%);
- The pitching moment coefficient, inverse to the lift coefficient, presents best results for offsets closest to the leading edge (Pitching moment coefficient increase lower than 10%);
- The C_l/C_d shows similar effects to the drag coefficient, so it does not have a best position for every lift coefficient range (C_l/C_d decrease lower than 15%);
- The $C_l^{3/2}/C_d$, has the same variation as the C_l/C_d ($C_l^{3/2}/C_d$ decrease lower than 15%).

5.4.5. LEEUAV's Solar Cells

- The reduced thickness-to-chord ratio associated with the LEEUAV's solar cells has, as consequence, less precise results;
- In the drag coefficient and C_l/C_d, being the performance at medium and higher speed most important, it must be chosen a position that presents good performance in both speed ranges;
- For the lift coefficient, the further away the offset is from the leading edge, the best performance it will have;
- The best position for placing the solar cells is between 0.21 and 0.23 of the airfoil's chord.

Chapter 6

6. Computational Fluid Dynamics Analysis

In this chapter, the second analysis, the Computational Fluid Dynamics (CFD) analysis, is described: a brief description of the software ANSYS Fluent and its turbulence models used in this work, followed by an explanation of the numerical procedure, its results and, lastly, by the drawn conclusions.

6.1. ANSYS Fluent and Turbulence Models Description

ANSYS, Inc. is a computer-aided engineering software, with engineering analysis software developed for a wide range of disciplines. In one of them, the fluid dynamics, we have ANSYS Fluent, first developed in 1961, which is a CFD software tool for design and analysis. Fluent includes well-validated physical modeling capabilities to deliver accurate results across a wide range of CFD and multiphysics applications, although it might be very time consuming since it requires a considerable knowledge about the software and physics models. Fluent provides a diverse choice of turbulence models, and no single turbulence model is universally accepted as being superior for all classes of problems. The turbulence model to be used must be chosen considering the physics encompassed in the flow, the level of accuracy required, the available computational resources and the amount of time available for the simulation. [25] [26]

The behavior of viscous fluid flow is described by the Navier-Stokes equations, which is time-dependent. This leads to two alternative methods that can be used to transform the Navier-Stokes equation in a way, that the small-scale turbulent fluctuations do not have to be directly simulated: Reynolds averaging and filtering. We will be focusing on the Reynolds-Averaged Navier Stokes (RANS), which is generally adopted for practical engineering calculations. RANS equations represent transport equations for the mean flow quantities only, with all the scales of turbulence being modeled. The approach of permitting a solution for the mean flow variables greatly reduces the computational effort and, if the mean flow is steady, the governing equations will not contain time derivatives and a steady-state solution can be obtained economically. The Reynolds-averaged approach uses models as Spalart-Allmaras, k-ε, k-ω and the Reynolds stress model. [26]

For this work, the most suitable solution would be to choose a model, with three or four equations, with boundary layer transition detection capability, but with the time and computational resources available, the best solution was to use a simpler two equation turbulence models, with the limitation of not predicting transition. Two equation models are considered the simplest and more complete turbulence models, in which the solution of two

separate transport equations allow the turbulent velocity and length scale to be independently determined. For this reason, the *k-ε* turbulence model and the *k-ω* turbulence model were chosen to be used in the present work, which are described next.

A more detailed description about modeling turbulence is described in reference [26].

6.1.1. Realizable *k-ε* Turbulence Model

The standard *k-ε* model is a semi-empirical model based on model transport equations for the turbulence kinetic energy (*k*) and its dissipation rate (*ε*). It has become the most used turbulence model for practical engineering flow calculations, because it is robust, economic and delivers reasonable accuracy for a wide range of turbulent flows. A limitation of this model is that it is only valid for fully turbulent flows. Further, at near-wall regions, near-wall modeling (enhanced wall treatment) must be used. Improvements have been made to the model to improve its performance, which has resulted in two variants available in Fluent: the RNG *k-ε* model and the Realizable *k-ε* model. [26]

The Realizable *k-ε* model is a relatively recent development and differs from the standard model in two significant ways: it contains a new formulation for the turbulent viscosity and a new transport equation for the dissipation rate, *ε,* has been derived from an exact equation for the transport of the mean-square vorticity fluctuations. The term “realizable” means that the model satisfies certain mathematical constraints on the Reynolds stresses, consistent with the physics of the turbulent flows. It provides better performance for flows involving rotation, boundary layer under strong adverse pressure gradients, separation, and recirculation. The realizable model provides the best performance of all the *k-ε* models versions. [26]

6.1.2. Shear-Stress Transport *k-ω* Turbulence Model

The standard *k-ω* model is an empirical model based on model transport equations for the turbulent kinetic energy (*k*) and the specific dissipation rate (*ω*). A variation of the standard *k-ω* model available in Fluent is the Shear-Stress Transport (SST) *k-ω* model. [26]

The SST *k-ω* model was developed to effectively blend the robust and accurate formulation of the *k-ω* model in the near-wall region, with the free-stream independence of the *k-ε* model in the far field. The improved model includes the four following refinements: the standard *k-ω* model and the transformed *k-ε* model are both multiplied by a blending function and added together; the SST model incorporates a damped cross-diffusion derivative term in the *ω* equation; the definition of the turbulent viscosity is modified to account for the transport of the turbulent shear stress; and the modeling constants are different. These improvements make the SST model more accurate and reliable for a wide class of flows, like the low Reynold number airfoil flows, than the standard model. [26]

6.2. Numerical Procedure

The procedure for a CFD analysis includes a sequence of steps: generation of geometry and mesh, definition of boundary conditions and simulation setups. These procedures are described next.

6.2.1. Geometry and Mesh Generation

The geometry for the different airfoils was designed using ANSYS DesignModeler, in which, unlike the XFOIL analysis, the forward facing step and backward facing step can form a 90-degree angle with the airfoil's upper surface. Therefore, there is no limitation to the geometry.

For the mesh generation, ANSYS Meshing was used. After several thorough studies on mesh quality and convergence, a final compromise was met, and the solution was to use a hybrid O-type mesh. It had the outer boundaries placed 35 chords away from the airfoil and, in addition to the global control volume, a smaller elliptical control volume was employed near the airfoil in the mesh generation process, which is the unstructured part of the mesh.

The airfoil was defined with 1,000 divisions around its contour and a bias factor was employed to place smaller divisions around the leading and trailing edge and in the steps' location. Special attention was given to the boundary layer region to ensure that the first point of the mesh corresponds to a y^+~1, and, for this, an inflation layer was used all around the airfoil. The final meshes have approximately 170,000 elements.

In Figure 6-1, the mesh for the LEEUAV (0.20;0.85;0.0025) is presented. It can be seen the global control volume and a detail of the mesh around the airfoil, which corresponds to the elliptical control volume. The mesh around the airfoil is unstructured except for the inflation layer.

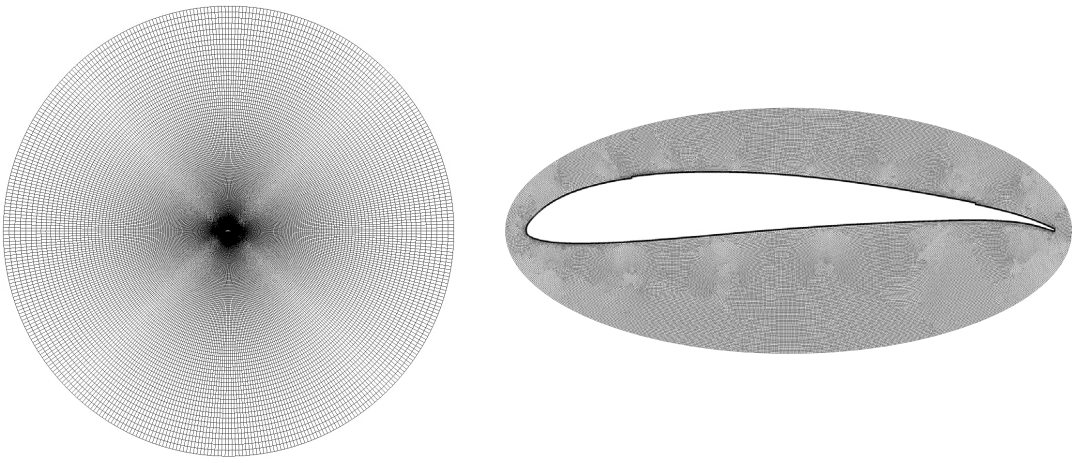

Figure 6-1 – General view of the mesh (on the left) and a detail around the airfoil (on the right)

6.2.2. Boundary Conditions and CFD Simulation Procedure

To simulate the airfoils at the desired flow conditions, of $Re\sqrt{C_l}$ = 150,000 as the XFOIL simulation, a density-based and steady state solver was used. The inlet was represented by a velocity inlet, using the velocity magnitude to prescribe the flow speed, and the outlet was represented by a pressure outlet. The desired angle of attack was obtained using the appropriate flow direction vector components. The airfoil top and bottom surfaces were defined, as wall boundary conditions, and the fluid inside the domain was defined as air with $\rho = 1.225\ kg/m^3$ and $\mu = 1.789 \cdot 10^{-5}$ Pa s. These procedures give the advantage of simulating all angles of attack using only a single mesh. A second order discretization was set for the flow and turbulence equations, and convergence was achieved by monitoring the residual monitors of the solution, as it dropped below $1 \cdot 10^{-6}$ for all equations.

To achieve the appropriate flow conditions of $Re\sqrt{C_l}$ = 150,000, for each angle of attack, from -3 deg to 15 deg, since is not automatic like in XFOIL, it was employed a Direct Optimization, so that the velocity was able to vary until the product of $Re\sqrt{C_l}$ was equal to the desired value. An average of 10 attempts was necessary to achieve $Re\sqrt{C_l}$ = 150,000 for each angle of attack, taking approximately 45 minutes to run a single Fluent simulation on an average desktop computer. For each airfoil, it took roughly 5 to 6 days until all solutions were calculated for the tested turbulence models in steady state solver.

6.3. Results and Discussions

The CFD results are divided into four parts: *1)* selection of the most suitable turbulence model for the analysis; *2)* comparison of the results from XFOIL and from ANSYS Fluent; *3)* analysis of the possible positions for the Long Endurance Unmanned Air Vehicle's (LEEUAV's) solar cells; *4)* visualization of the steps' effects in the airflow over the airfoil.

6.3.1. Turbulence Model Study

For the CFD analysis, two turbulence models were tested: The Realizable k-ε model and the SST *k-ω* model. With the SST *k-ω* model two options were tried, the default one and the low-Reynolds-number (Low-*Re*) correction, in which were included corrections that improve the accuracy in predicting low Reynolds number flows [27].

For the SST *k-ω* model with Low-*Re* corrections not every angle of attack was calculated, because, for higher angles of attack, the steady state solver did not converge, since vortex shedding was very active, that, in turn, produced grave oscillations in the pressure field about the airfoil [20]. Consequently, it was necessary to use transient state solver, which exponentially increased the computational cost. The results are presented in Chart 6-1, where the comparison of the drag and lift coefficient for the LEEUAV's airfoil obtained from XFOIL and from ANSYS Fluent is shown.

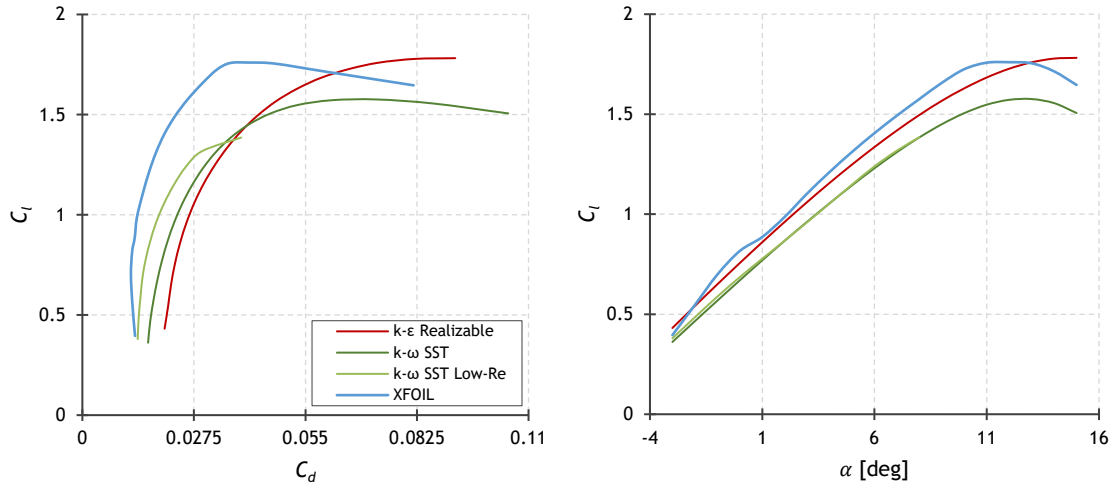

Chart 6-1 - LEEUAV's airfoil drag polar (on the left) and lift coefficient curve (on the right) for $Re\sqrt{C_l}$ = 150,000 for XFOIL and for ANSYS Fluent

None of the turbulence models produces accurate results with the XFOIL's solution, but since the most important aspect in this study is the comparison of the results between the clean airfoil and the airfoils with offsets, the turbulence model should be chosen considering the polar curves shape and not the absolute value, that is the model that best resembles the XFOIL's solution.

The Realizable *k-ε* model, from all the above models, is the one which overpredicts the drag coefficient the most. But regarding the lift coefficient, it delivers more accurate results in the linear portion of the lift coefficient curve, but it does not predict well the maximum lift coefficient, overpredicting it for an angle of attack higher than 15 deg. The SST *k-ω* model presents better results in the drag coefficient prediction than the Realizable *k-ε* model, being the Low-*Re* correction that presents the best results. This model, with and without Low-*Re* corrections, under predicts the lift coefficient with very similar results for both options. In addition, since none of the models predicts transition, none of them predicts the corners of the low drag region.

In Chart 6-2, the C_l/C_d and $C_l^{3/2}/C_d$ curves are presented, where it is visible which model best resembles the XFOIL polar curves. The worst model is the Realizable *k-ε* model, which exaggeratedly under predicts C_l/C_d and $C_l^{3/2}/C_d$. The better one, still with under prediction of C_l/C_d and $C_l^{3/2}/C_d$, is the SST *k-ω* model with Low-*Re* corrections, which best resembles the shape and absolute value of the C_l/C_d and $C_l^{3/2}/C_d$ curves from XFOIL. The setback of the option with the Low-*Re* corrections is not predicting all the angles of attack in steady state solver.

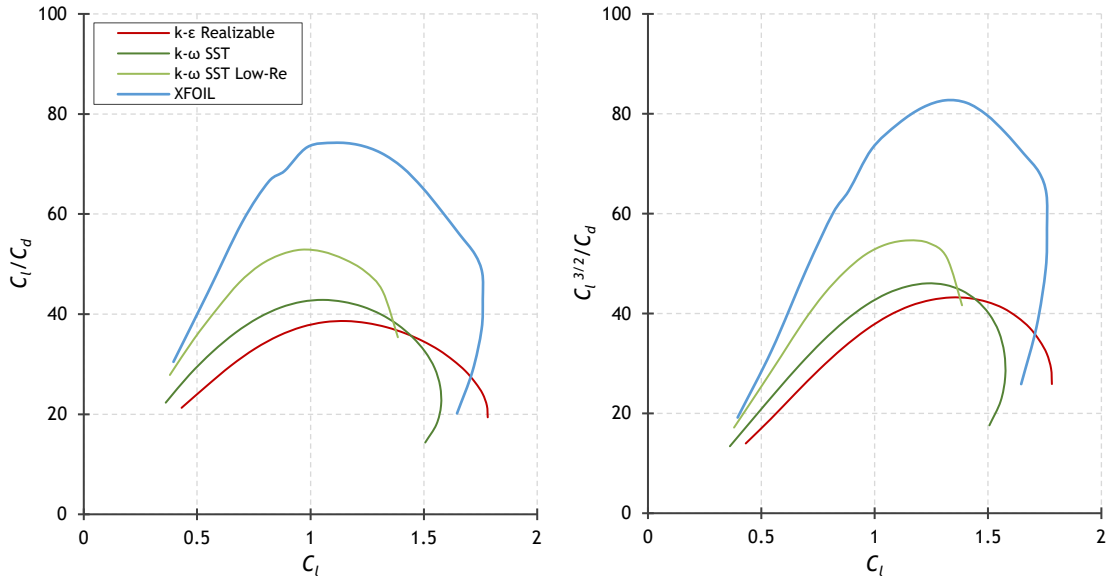

Chart 6-2 - LEEUAV's airfoil C_l/C_d (on the left) and $C_l^{3/2}/C_d$ (on the right) for $Re\sqrt{C_l}$ = 150,000 for XFOIL and for ANSYS Fluent

Taking all the considerations into account, the most suitable model to use in this work is the SST k-ω model, with better results than the Realizable k-ε model, and considerable less computational costs than the SST k-ω model Low-*Re*, despite less accurate results.

As stated in section "5.1. XFOIL Description", XFOIL uses an approximate e^N envelope method to calculate transition, in which *N* can be calculated by Eq. (1), as presented by van Ingen [28], where T_u represents the absolute turbulence intensity. In order to approximate the solution from XFOIL to Fluent, it is possible to increase turbulence intensity within XFOIL by decreasing *N*. The minimal value allowed by XFOIL is 0, in which turbulent flow is present in all the airfoil's chord.

$$N = -8.43 - 2.4\, ln\, T_u \quad (1)$$

In Chart 6-3, a comparison between the used *N*'s default value of 9 and the minimal value allowed by XFOL with the turbulence model chosen in Fluent is presented. For the XFOIL results with *N* = 0, the results are in good agreement with the Fluent's solution, noticing that the turbulence model used is fully turbulent. The airfoil's most relevant performance characteristics are summarized in Table 6-1: it is clear that the results are in good agreement with the turbulence model when increasing turbulence intensity in XFOIL.

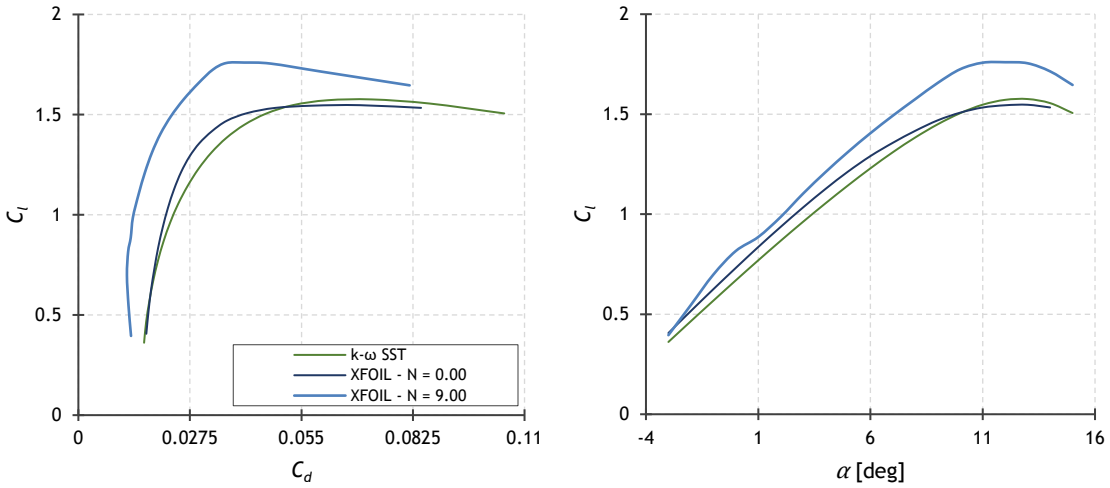

Chart 6-3 - LEEUAV's airfoil drag polar (on the left) and lift coefficient curve (on the right) for $Re\sqrt{C_l}$ = 150,000 for different *N* values in XFOIL and for the SST *k*-*ω* model in ANSYS Fluent

Table 6-1 - LEEUAV's airfoil aerodynamic performance for XFOIL and for the SST *k*-*ω* model

		XFOIL		SST *k*-*ω* model
		N = 9	*N* = 0	
Maximum lift coefficient	$C_{l_{max}}$	1.76	1.55	1.58
Maximum lift angle of attack	$\alpha_{C_{l_{max}}}$	12 deg	13 deg	13 deg
Maximum lift-to-drag ratio	$(C_l/C_d)_{max}$	74.25	47.90	42.85
Lift coefficient of maximum lift-to-drag ratio	$C_{l_{(C_l/C_d)_{max}}}$	1.10	1.21	1.05
Maximum lift$^{3/2}$-to-drag ratio	$\left(C_l^{3/2}/C_d\right)_{max}$	82.70	53.53	46.03
Lift coefficient of maximum lift$^{3/2}$-to-drag ratio	$C_{l_{\left(C_l^{3/2}/C_d\right)_{max}}}$	1.31	1.29	1.23

6.3.2. XFOIL Results Comparison

Next, the comparison between the results obtained from XFOIL and from ANSYS Fluent for the LEEUAV clean airfoil and for airfoils with offsets are presented. The objective is to understand if the relation between the airfoils is the same in both software programs. The scale of the polar graphs for the results obtained with Fluent is different from the ones with XFOIL, so that, the results are more similar between them.

The combinations of the chosen offsets to perform the CFD analysis were the ones with lengths of 0.65: for the thickness-to-chord ratio equal to 0.0025 and 0.005, three offsets initial positions were tested, 0.10, 0.20 and 0.30; and for the greater thickness-to-chord ratios, of 0.0075 and 0.01, only the offset initial position at 0.10 of the chord was tested. A total of eight offset combinations were tested.

In Chart 6-4, the drag polar curve for both software programs is presented. As it was predicted, the results are more similar for greater thickness-to-chord ratios, because, in XFOIL, the greater the thickness-to-chord ratio, the higher the panel angle in the steps' location and the more trustworthy is the step's geometry.

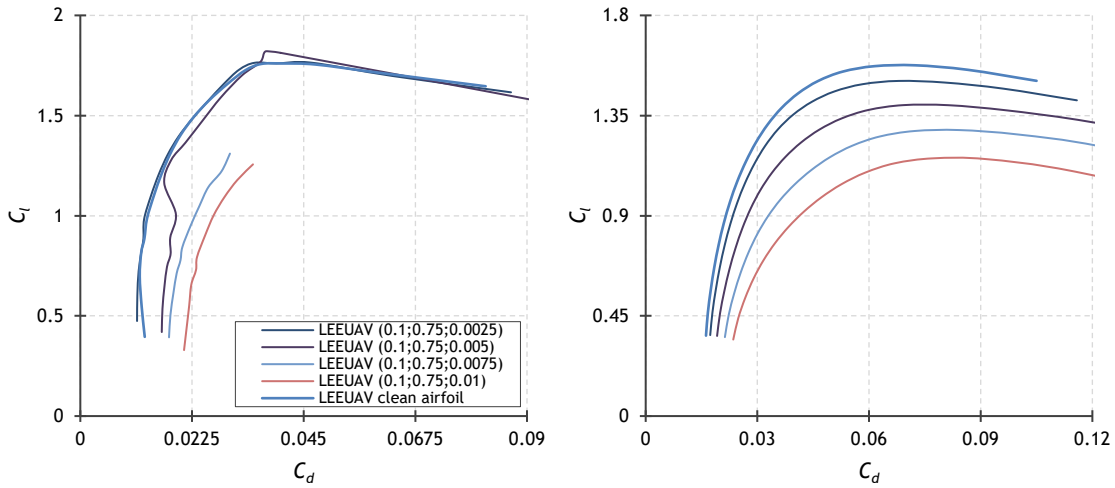

Chart 6-4 - Drag polar at $Re\sqrt{C_l}$ = 150,000 for the LEEUAV's clean airfoil and for different offset combinations obtained from XFOIL (on the left) and from ANSYS Fluent (on the right)

The results from Fluent are in reasonable agreement with the ones from XFOIL, emphasizing two details: first, since it was used a turbulence model without the capabilities to calculate transition, the curves are smoother than the ones from XFOIL. The decrease in the drag coefficient seen in the XFOIL's drag polar for the offset with thickness-to-chord ratio of 0.005 as the lift coefficient rises is not present in the Fluent results. Second, for smallest thickness-to-chord ratio in XFOIL, it does not present great difference from the clean airfoil, though in Fluent it does, specially the thickness-to-chord ratio of 0.0025 that in XFOIL the results are very similar to the clean airfoil. This is due to the small panel angle in the steps' location, existing in the XFOIL geometry, that in Fluent is a perfect 90-degree step.

With the lift coefficient curve, in Chart 6-5, is the same outcome. The results in Fluent are in reasonable agreement with the ones obtained from XFOIL. For Fluent results, the curves are smoother and unlike the XFOIL results, the lift coefficient for the airfoils with offsets presents very similar performance to the clean airfoil for low angles of attack. Furthermore, a detail that was not possible to realize in the XFOIL results, due to the scarcity of point in the greater thickness-to-chord ratios, is that the maximum lift coefficient is inversely proportional to the thickness-to-chord ratio.

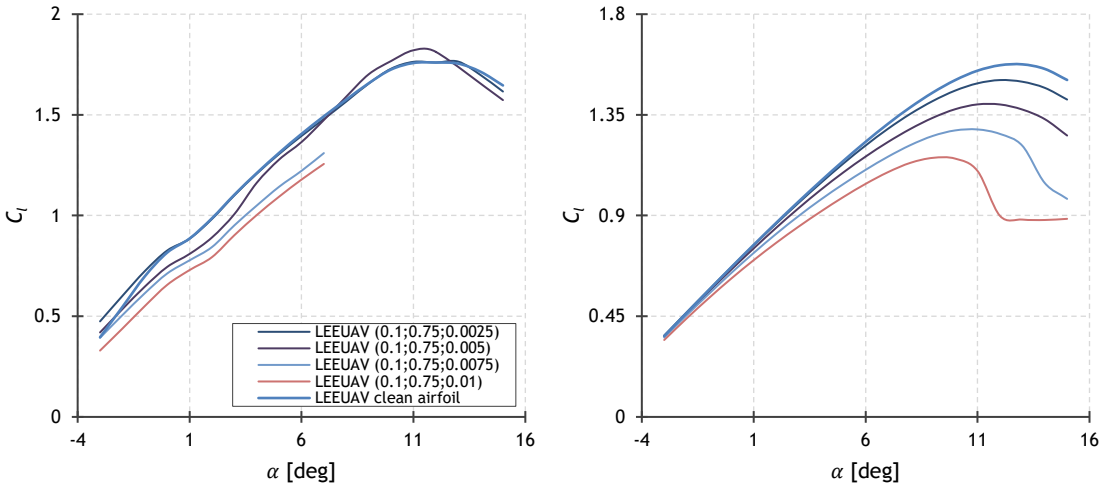

Chart 6-5 – Lift coefficient curve at $Re\sqrt{C_l}$ = 150,000 for the LEEUAV's clean airfoil and for different offset combinations obtained from XFOIL (on the left) and from ANSYS Fluent (on the right)

In the case of the XFOIL results, for smaller thickness-to-chord ratios, the increase in thickness and camber, caused by the offset, has visible effects in the increase of lift coefficient and decrease of drag coefficient in some ranges of lift coefficient. But in ANSYS Fluent, the performance with the offset presence are always worse, compared to the clean airfoil performance. The steps' effects are always greater than the ones from the increase in camber and thickness.

An important aspect, highlighted in the XFOIL analysis, is the relationship between the different offsets' positions. These are demonstrated in Chart 6-6 and Chart 6-7, where C_l/C_d accompanied with the corresponding differences chart are presented, as previously seen in the XFOIL analysis. These are related to the offsets with thickness-to-chord ratio of 0.005 and with offset initial position of 0.20 and 0.30 of the airfoil's chord.

The relationship between the different offsets' positions are in good agreement for both software programs. Higher lift coefficients are the exception, that in the XFOIL results the C_l/C_d curves crosses each other, which in the Fluent results it does not happen. Also, it is visible that the performance differences are more degrading, as we move towards lower lift coefficients, unlike the XFOIL, that were higher than the clean airfoil in some lift coefficient ranges and lower in others.

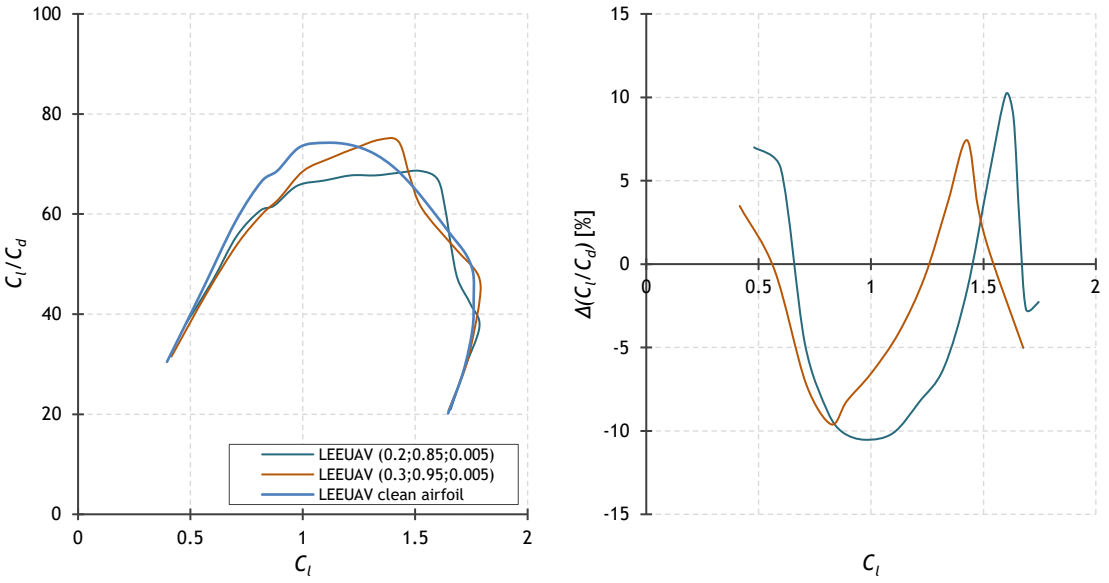

Chart 6-6 - C_l/C_d curve at $Re\sqrt{C_l}$ = 150,000 for the LEEUAV's clean airfoil and for different offset combinations (on the left) and its corresponding differences (on the right) for the XFOIL results

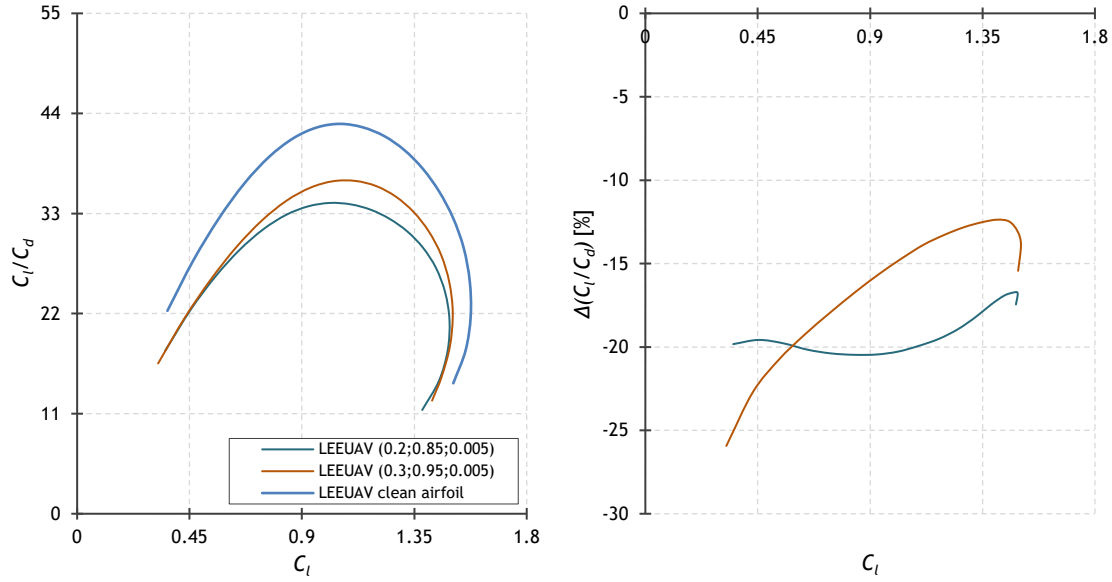

Chart 6-7 - C_l/C_d curve at $Re\sqrt{C_l}$ = 150,000 for the LEEUAV's clean airfoil and for different offset combinations (on the left) and its corresponding differences (on the right) for the ANSYS Fluent results

The variation of C_l/C_d by the airfoils with offsets with thickness-to-chord ratio equal to 0.005 and 0.0025, can be divided in three regions, not four like the XFOIL results, within the lift coefficient that vary according to the thickness-to-chord ratio of the offset:

- C_l > ~ 0.6-0.8, where the $(x/c)_i$ closest to the leading edge decreases C_l/C_d (this C_l limit tends to increase with the decrease of the thickness-to-chord ratio);
- ~ 0.2-0.5 < C_l < ~ 0.6-0.8, where the $(x/c)_i$ furthest away from the leading edge decreases C_l/C_d (this C_l limits tends to increase with the decrease of the thickness-to-chord ratio);

- C_l < ~ 0.2-0.5, where the $(x/c)_i$ closest to the leading edge decreases C_l/C_d (not visible for this thickness-to-chord ratio).

Chart 6-8 and Chart 6-9 display a comparison of the pressure coefficient distributions between the results obtained from XFOIL and Fluent for a 3 deg angle of attack. The results are in good agreement for the first half of the airfoil's chord, after that, the results from Fluent do not show a significant change in the pressure coefficient over the backward facing step, as does the XFOIL results. The decrease in pressure coefficient over the forward facing step, in the Fluent results, is more accentuated than the XFOIL results. This is due to the step's geometry, that in Fluent is a 90-dregre step, unlike the XFOIL.

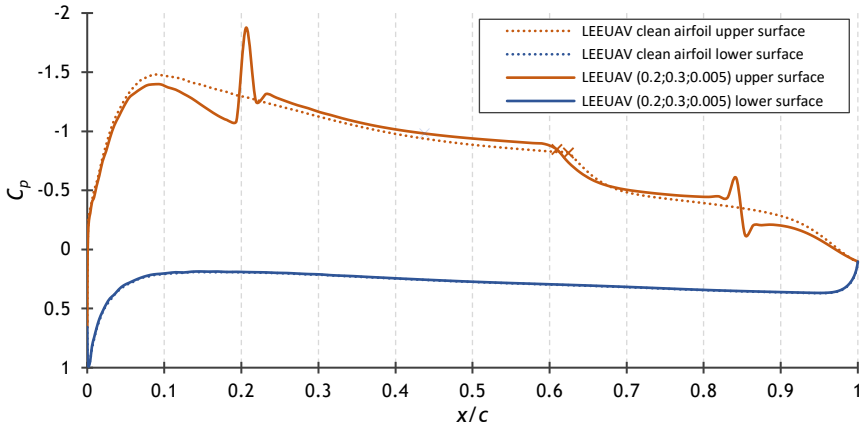

Chart 6-8 – XFOIL's pressure coefficient distribution at $Re\sqrt{C_l}$ = 150,000 for α = 3 deg for the LEEUAV clean airfoil and for the LEEUAV (0.20;0.85;0.005)

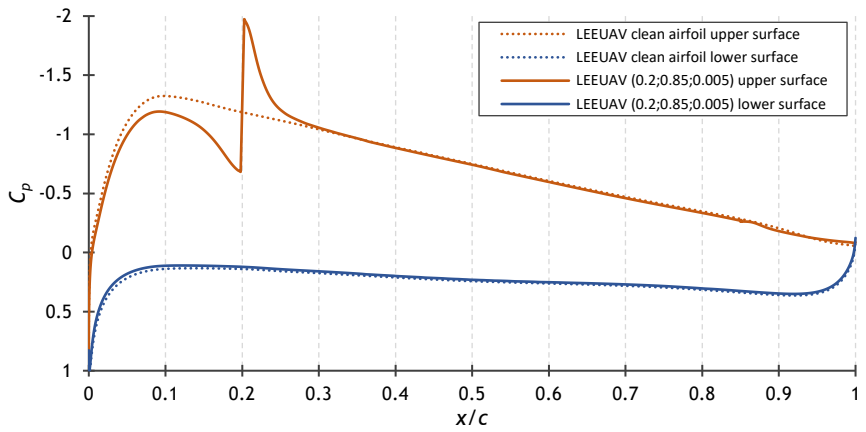

Chart 6-9 – ANSYS Fluent's pressure coefficient distribution at $Re\sqrt{C_l}$ = 150,000 for α = 3 deg for the LEEUAV clean airfoil and for the LEEUAV (0.20;0.85;0.005)

6.3.3. LEEUAV's Solar Cells

For the LEEUAV's solar cells, all six possibilities for the solar cells' positions were tested. The results confirmed the outcome from the XFOIL analysis that the best positions for placing the offset is between 0.21 and 0.23 of the chord.

As previously said, the results from XFOIL showed regions where the airfoils with offsets show better performance than the clean airfoil. To the Fluent results, the relationship between positions remain the same, but the difference in respect to the clean airfoil is different. This is caused by the small thickness-to-chord ratio, which caused extremely small panel angle in the steps' location in XFOIL, and, therefore, less precise results. With a 90-degree steps in Fluent, the results from the airfoils with offsets are always worse than the ones from the clean airfoil.

As for the drag coefficient, displayed at Chart 6-10, for the best three positions, the results are very similar between them. Showing that any of the three positions deliver best performance for the drag coefficient between all options of positions. The penalty in drag coefficient is more pronounced for lower lift coefficients, which means that as velocity increases, the difference in drag coefficient regarding to the clean airfoil increases. The increases in drag coefficient for the lift coefficient range tested vary from approximately 0.1% to 3.1%.

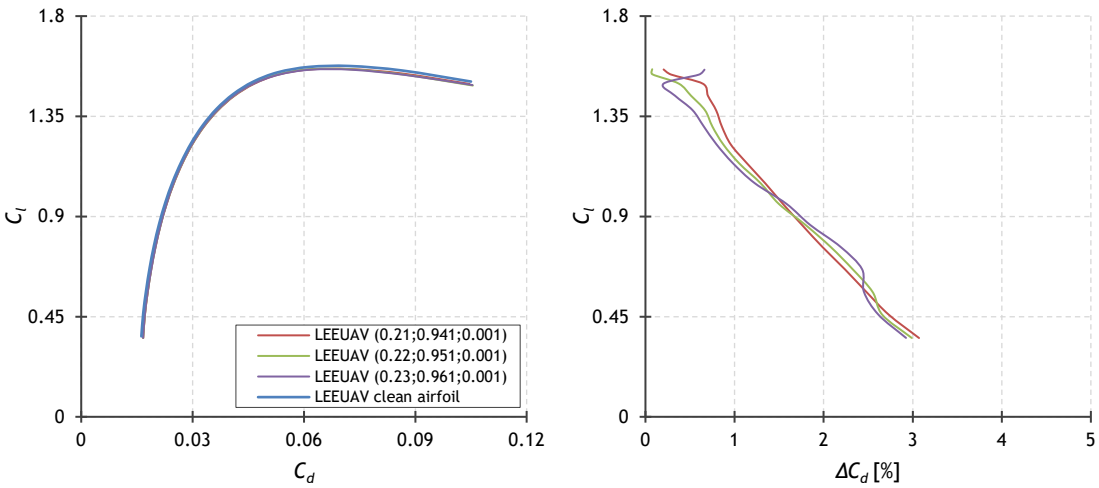

Chart 6-10 - Drag polar at $Re\sqrt{C_l}$ = 150,000 for the LEEUAV's clean airfoil and for the best offset positions with the same characteristics as the solar cells (on the left) and its corresponding differences (on the right)

Regarding the lift coefficient, in Chart 6-11, the results are also very similar for the three best positions for placing the solar panels. Even so, the offset initial position at 0.23 of the chord presents slightly better results than the alternatives. Alike the drag coefficient, the penalty in the lift coefficient is also more pronounced for higher speeds. The decreases in the lift coefficient for the range of angles of attack tested vary from approximately -0.4% to -2.1%.

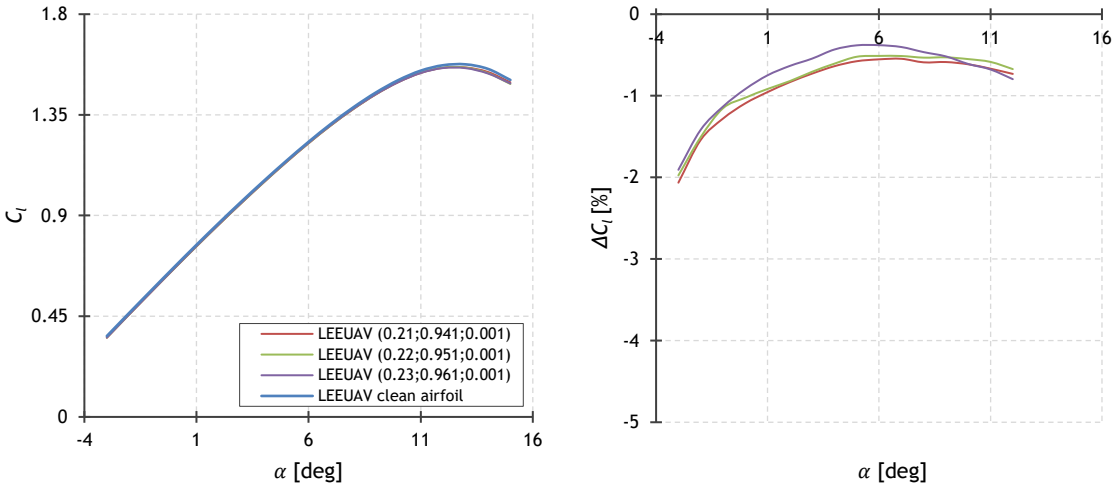

Chart 6-11 - Lift coefficient curve at $Re\sqrt{C_l}$ = 150,000 for the LEEUAV's clean airfoil and for the best offset positions with the same characteristics as the solar cells (on the left) and its corresponding differences (on the right)

In Chart 6-12, the results regarding C_l/C_d are presented. As seen in the XFOIL analysis for the C_l/C_d, as well as the drag coefficient, there is not a position that delivers best performance for all the lift coefficient range. But the little difference from the lift coefficient for the offset initial position at 0.23 of the chord makes a difference in C_l/C_d, delivering the best performance from the three positions at almost all lift coefficient range. The penalty associated to C_l/C_d for the lift coefficient range tested vary from approximately -0.7% to -5%.

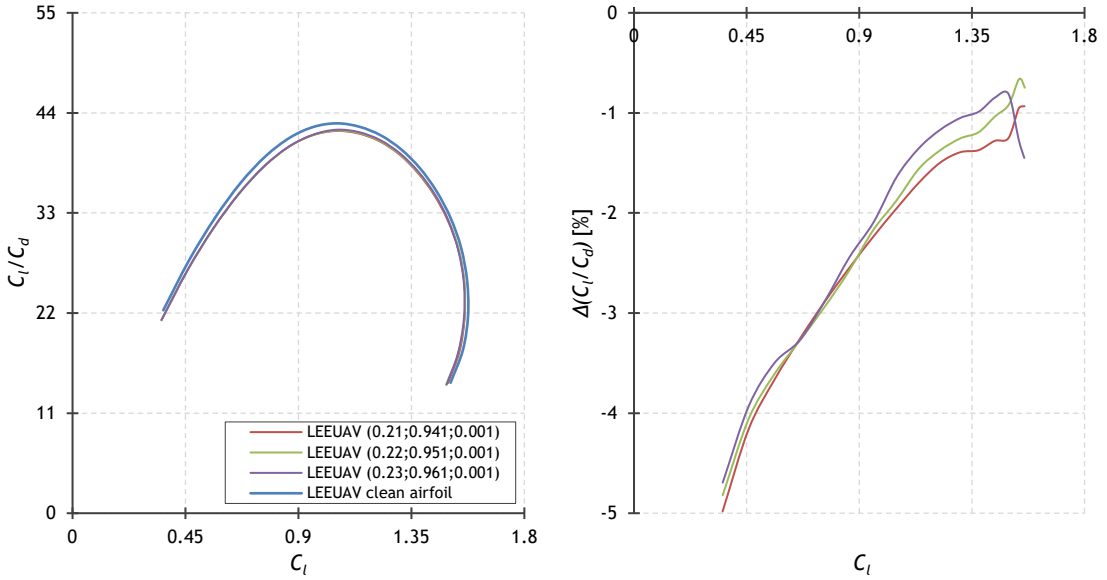

Chart 6-12 – C_l/C_d curve at $Re\sqrt{C_l}$ = 150,000 for the LEEUAV's clean airfoil and for the best offset positions with the same characteristics as the solar cells (on the left) and its corresponding differences (on the right)

6.3.4. Step's Effects

Figure 6-2 shows a comparison of the velocity magnitude contour for the LEEUAV clean airfoil and for airfoils with offsets for the four-principal thickness-to-chord ratios under the same flow speed and at the same angle of attack of 3 deg. The steps' effects in the flow are perfectly visible as described in section "2.2. Effects of Steps": the forward facing step (FFS) creates two separations regions, one upstream and one downstream; and the backward facing step (BFS) creates a separation region downstream, that is extended to the trailing edge for greater step's height.

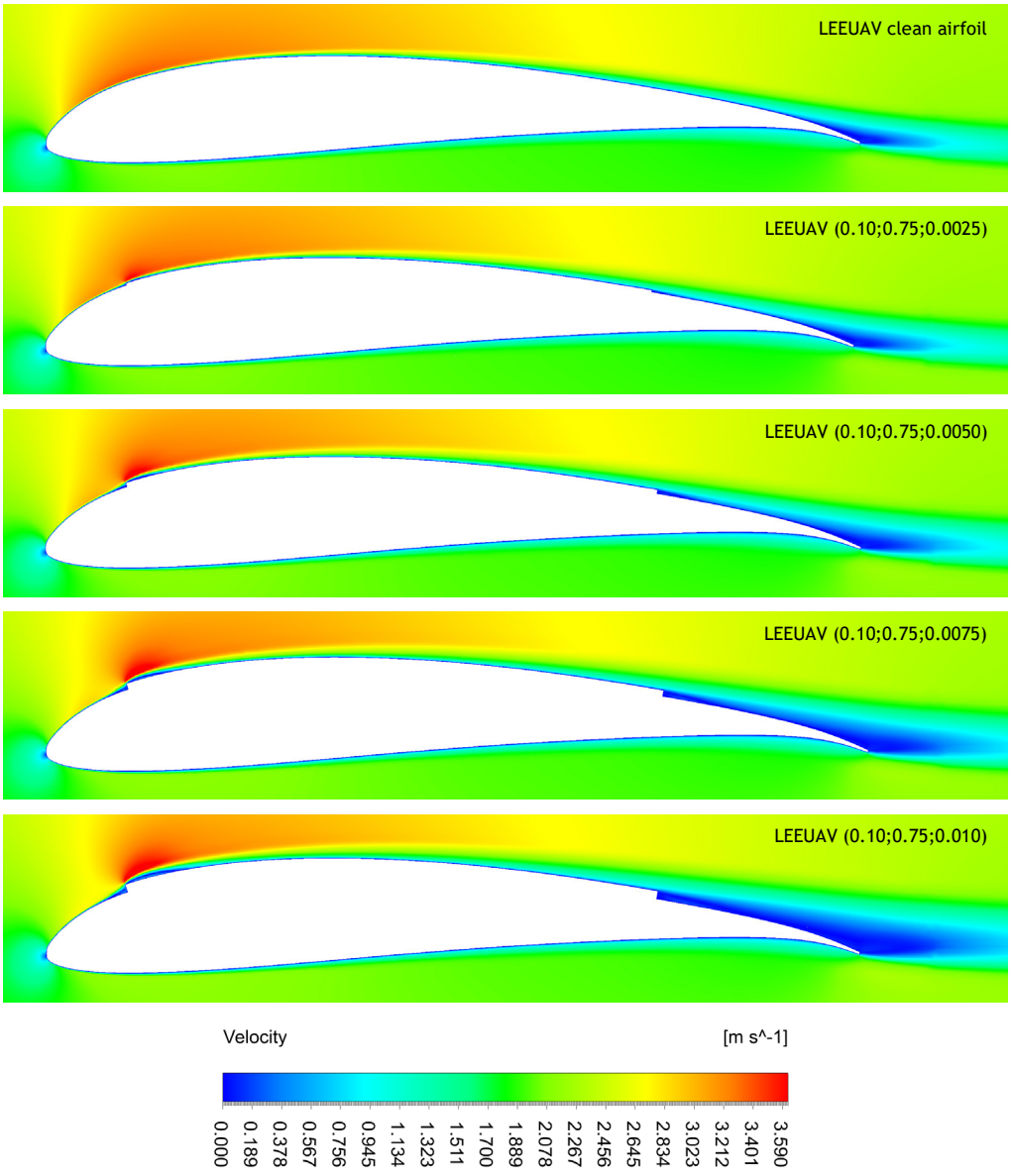

Figure 6-2 – Comparison of velocity magnitude contour under an angle of attack of 3 deg at *Re* = 150,000 between computed results for the LEEUAV clean airfoil and for the airfoil with offsets for the four-principal thickness-to-chord ratio

The size of these separation regions is proportional to the steps' height. The features of the forward and backward facing steps can be seen in detail in Figure 6-3, with the flow streamlines evidencing the separation regions.

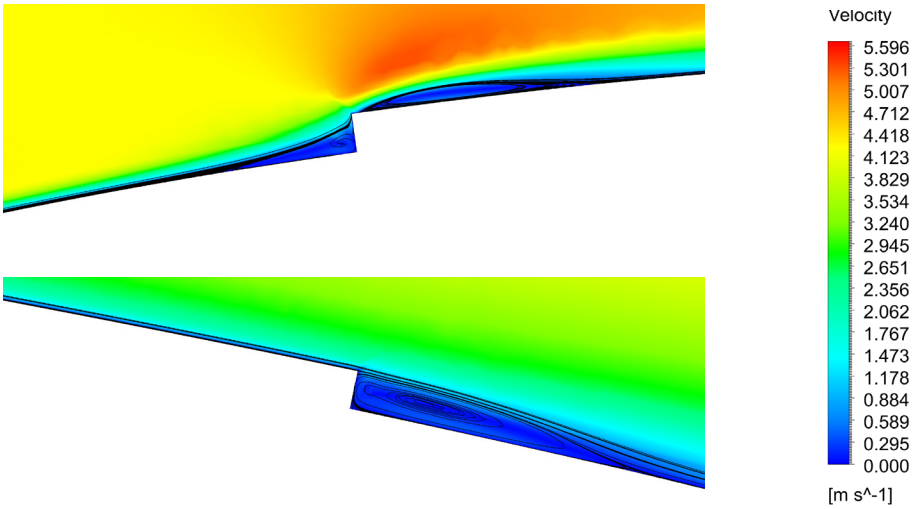

Figure 6-3 – Detail of flow streamlines with velocity contour under an angle of attack of -3 deg at $Re\sqrt{C_l}$ = 150,000 for the FFS and BFS of the LEEUAV (0.20;0.85;0.005)

In Figure 6-4, a comparison of the turbulence kinetic energy between the clean airfoil and airfoils with offsets in different positions is shown. These offsets have a thickness-to-chord ratio of 0.005 and the airfoils are subjected to the same flow conditions at an angle of attack of 3 deg. As concluded with the XFOIL analysis, and mentioned in section "2.2. Effects of Steps", the separation downstream of the forward facing step generates the highest levels of turbulence, showing that the forward facing step position (the offset initial position) is the most important aspect when choosing the position of the offset (solar cells).

Concerning the other separations regions, the separation upstream of the forward facing step does not generate a significant amount of turbulence, and the separation downstream of the backward facing step generates a visible increase in turbulence, although with no comparison to the increase in the separation downstream of the forward facing step. Also, in this angle of attack, the closest to the leading edge the forward facing step is, the greatest levels of turbulence it generates. More specifically, the turbulence kinetic energy, after the forward facing step placed at 0.10 of the chord, is substantially higher than the forward facing step placed at 0.30.

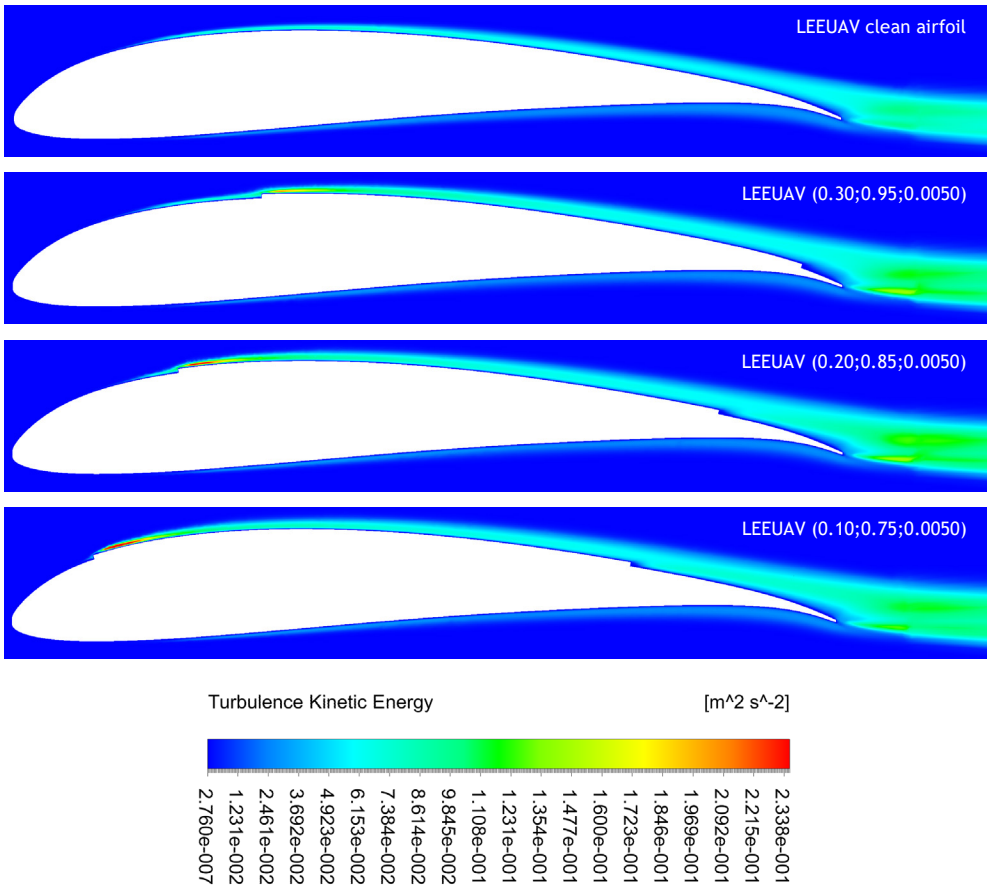

Figure 6-4 - Comparison of turbulence kinetic energy under an angle of attack of 3 deg at *Re* = 150,000 between computed results for the LEEUAV clean airfoil and for the LEEUAV with offsets with four thickness-to-chord ratios equal to 0.005

6.4. Conclusions

The CFD analysis using ANSYS Fluent, as well as the XFOIL analysis, had its limitations. A more complex turbulence model with transitions detections capability would be a better option, but due to the computational resources and time available, the two equations SST *k-ω* model was chosen. The Fluent solution does not resemble the XFOIL solution in absolute value when the XFOIL' s parameter *N* is set to 9, but despite this, it was possible to validate the results of the previous analysis: the relationship between the LEEUAV clean airfoil and the LEEUAV airfoils with offsets and the relationship between the different airfoil with offsets. In addition, since there was no limitation regarding the geometry, it was possible to refine the results from XFOIL.

This analysis proved that the panel angle, in the steps' location in the XFOIL geometry, not being a perfect 90-degree angle, had its influences in the solution. Fluent results showed that the offset presence is always degrading for the airfoil performance relative to the clean airfoil, with the difference, in percentage, proportional to the flow speed. This means that, as speed increases, the influence of the offset relative to the clean airfoil intensifies.

Regarding the LEEUAV's solar cells, this analysis came to confirm that the best positions for the solar cells are between 0.21 and 0.23 of the airfoil's chord, with better results for the further aft position. For the drag coefficient, it is expected an increase of up to approximately 3% for low lift coefficients, a loss of up to about 2% of the lift coefficient and a variation of the pitching moment coefficient of only around 0.5%. Concerning C_l/C_d and $C_l^{3/2}/C_d$, it is expected losses of 5% and 6%, respectively.

And finally, through the airflow visualization, by the velocity contours, streamlines and turbulence kinetic energy, it was possible to confirm the expected flow features described in the literature for the forward and backward facing steps flows.

This page has been intentionally left blank
for double side copying

Chapter 7

7. Conclusions and Recommendations

"If an airplane has succeeded to fly day and night without fuel, then we can power our world on clean energy."

Bertrand Piccard

7.1. Summary

The aim of this work was to perform an aerodynamic analysis of a forward-backward facing step pair on the upper surface of a low-speed airfoil, belonging to the Long Endurance Electric Unmanned Air Vehicle (LEEUAV), due to the presence of solar cells.

For this, two numerical analysis using XFOIL and ANSYS Fluent were performed, both with limitations. In XFOIL, the geometry of the step could not form a 90-degree angle with the airfoil's upper surface, since it resulted in program errors. This lead to the underprediction of the offset effects, more pronounced for the smallest thickness-to-chord ratios. In ANSYS Fluent, due to the time and computational resources available, a fully turbulent model was used, which was not capable of predicting transition. Thus, no transition effects were calculated.

The analysis performed with both software programs corresponds to an aircraft, undergoing trim speed changes in level flight at a given altitude, in which the parameter $Re\sqrt{C_l}$ is held constant. This is automatic in XFOIL, but in ANSYS Fluent it was necessary to implement an iterative strategy, which made the CFD analysis very time consuming.

With XFOIL, it was possible to understand which positions were worst to the airfoil performance and the relationship between the best positions. First, the greater thickness-to-chord ratios, of 0.0075 and 0.01, originated program errors in XFOIL, which resulted in insufficient polar points for a considerable number of offset combinations. Second, the offset initial positions of 0.10 and 0.15 resulted in premature forced transition, which resulted in increase in drag coefficient and reduction in lift coefficient. Also, regarding the offset initial position, when positioned after 0.30 of the chord, it resulted in increase in drag coefficient and reduction in lift coefficient. Third, when the offset final position was forward of 0.80 of the chord, it originated transition with the related effects.

The best positions for the forward facing step, based on the analysis performed, is between 0.20 and 0.30 of the airfoil's chord and for the backward facing step between 0.80 and 0.95.

Yet, the backward facing step have negligible effects when compared to the effects of the forward facing step. Regarding the relationship between the best positions: for the drag coefficient, there is not a position that delivers best performance for all lift coefficient range; for the lift coefficient, the farther from the leading edge, the better performance for the majority of the range of angles of attack; and the pitching moment coefficient has the opposite effects of the lift coefficient. After this initial study, the exact thickness and length of the LEEUAV's solar cells were analyzed, and the best positions for placing the forward facing step, the ones that deliver best performance, were determined as being between 0.21 and 0.23 of the airfoil's chord.

For the CFD analysis, first it was tested two turbulence models, to see which resembled best the XFOIL's solution. With disappointing absolute results, the model chosen was the SST k-ω turbulence model. Then, a small number of offset combinations were analyzed, that served to validate the results from XFOIL, which were in reasonable agreement, except for small details due to the chosen turbulence model. Afterwards, the exact thickness and length of the LEEUAV's solar cells where analyzed, where the influence and relationship between positions were confirmed. It also showed that the offset presence is always degrading compared to the clean airfoil. In addition, it was possible to conclude that the best position, as previously predicted, is between 0.21 and 0.23 of the airfoil's chord. Yet, the best performance is delivered for the farther position, and it was possible to quantify the loss in performance, losses of up to 5% of C_l/C_d.

It is clear that XFOIL is an excellent airfoil design and analysis tool. The ease of use of XFOIL compared to the more complex CFD analysis performed in ANSYS Fluent, has given the chance to test a wide range of offset combinations, although with the limitation of underpredicting the damage caused by the limitation in geometry. ANSYS Fluent requires much more time, in both computational time and personal work time, and an incredible amount of software and model knowledge. Nevertheless, it delivered more consistent results than XFOIL, since it does not have a geometrical limitation.

7.2. Concluding Remarks

This analysis concludes that the best positions for having an offset on the upper surface of the LEEUAV's airfoil is placing the offset initial position between 20% and 30% of the airfoil's chord and the final position between 80% and 95%. But the offset initial position is what really makes an impact on the airfoil performance.

The final objective of this work, is to provide the best position for placing the solar cells, and this is between 21% and 23% of the airfoil's chord, with general best results for the farther position, with losses of around 5% of C_l/C_d for lower lift coefficients relative to the LEEUAV's clean airfoil performance.

7.3. Future Work

In the future, regarding the analysis of the solar cells influence, a more detailed CFD analysis should be performed with a more adequate turbulence model, with boundary layer transition detection capability.

Concerning the LEEUAV project, considering the losses in C_l/C_d performance, a new wing with the solar arrays embedded in its upper surface should be designed and constructed.

This page has been intentionally left blank
for double side copying

References

[1] Research and Markets, "Unmanned Aerial Vehicles (UAV) Market, By Value and Volume Analysis and Forecast, 2015-2020," 2016.

[2] A. C. Marta and P. V. Gamboa, "Long Endurance Electric UAV for Civilian Surveillance Missions," in *29th International Council of the Aeronautical Sciences Congress*, St. Petersburg, Russia, 2014.

[3] R. J. Boucher, "Sunrise, the world's first solar-powered airplane," *Journal of Aircraft,* vol. 22, no. 10, pp. 840-846, 1985.

[4] X. Zhu, Z. Guo and Z. Hou, "Solar-powered airplanes: A historical perspective and future challenges," *Progress in Aerospace Sciences,* vol. 71, pp. 36-53, 2014.

[5] M. Hoffborn, *A historical survey of solar powered airplanes and evaluation of it's potential market,* Sweden: Mälardalen University, School of Innovation, Design and Engineering, 2009.

[6] NASA, "Armstrong Photo Gallery," 26 July 2016. [Online]. Available: http://www.nasa.gov/centers/armstrong/multimedia/imagegallery/index.html. [Accessed 26 September 2016].

[7] Airbus Defence & Space, "Zephyr," [Online]. Available: https://airbusdefenceandspace.com/our-portfolio/military-aircraft/uav/zephyr/. [Accessed 12 October 2016].

[8] Solar Impulse SA 2016, "Solar Impulse - Exploration to Change the World," [Online]. Available: http://www.solarimpulse.com/. [Accessed 14 October 2016].

[9] D. Leclercq, M. Jacob, A. Louisot and C. Talotte, "Forward-backward facing step pair - Aerodynamic flow, wall pressure and acoustic characterisation," in *7th AIAA/CEAS Aeroacoustics Conference and Exhibit*, Maastricht, Netherlands, 2001.

[10] H. Abu-Mulaweh, "A review of research on laminar mixed convection flow over backward- and forward-facing steps," *International Journal of Thermal Sciences,* no. 42, p. 897–909, 2003.

[11] J. K. Eaton and J. P. Johnston, "A Review of Research on Subsonic Turbulent Flow Reattachment," *The American Institute of Aeronautics and Astronautics,* vol. 19, no. 9, pp. 1093-1100, 1981.

[12] M. Sherry, D. L. Jacono and J. Sheridan, "An experimental investigation of the recirculation zone formed downstream of a forward facing step," *Journal of Wind Engineering and Industrial Aerodynamics,* vol. 98, no. 12, pp. 888-894, 2010.

[13] F. Mishriky and P. Walsh, "Effect of the Backward-Facing Step Location on the Aerodynamics of a Morphing Wing," *Aerospace,* vol. 3, no. 3, 2016.

[14] F. Floyd and K. Richard, "Airfoil for aircraft". United States Patent US 3706430 A, 19 December 1972.

[15] D. G. Fertis and L. L. Smith, "Airfoil". United States Patent US 4606519 A, 19 August 1986.

[16] F. Finaish and S. Witherspoon, "Aerodynamic Performance of an Airfoil with Step-Induced Vortex for Lift Augmentation," *Journal of Aerospace Engineering,* vol. 11, no. 1, pp. 9-16, 1998.

[17] C. R. Marks, M. P. Rumpfkeil and G. W. Reich, "Predictions of the effect of wing camber and thickness on airfoil self-noise," in *20th AIAA/CEAS Aeroacoustics Conference*, Atlanta, 2014.

[18] L. F. Cândido, "Projeto de um UAV Solar de grande autonomia," Universidade da Beira Interior, Covilhã, 2014.

[19] H. M. Vidales, "Design, Construction and Test of the Propulsion System of a Solar UAV," Instituto Superior Técnico, Lisboa, 2013.

[20] N. M. Silva, "Parametric Design, Aerodynamic Analysis and Parametric Optimization of a Solar UAV," Instituto Superior Técnico, Lisboa, 2014.

[21] J. C. Sousa, "Solar System for a Long Endurance Electric UAV," Universidade da Beira Interior, Covilhã, 2015.

[22] A. E. Duarte, "Development part of the Structure of a Long Endurance Electric UAV," Universidade da Beira Interior, Covilhã, 2016.

[23] M. Drela, "XFOIL: An Analysis and Design System for Low Reynolds Number Airfoils," in *Conference on Low Reynolds Number Airfoil Aerodynamics*, University of Notre Dame, 1989.

[24] J. Morgado, R. Vizinho, M. Silvestre and J. Páscoa, "XFOIL vs CFD performance predictions for high lift low Reynolds number airfoils," *Aerospace Science and Technology,* no. 52, pp. 207-214, 2016.

[25] ANSYS, Inc., "ANSYS Fluent," 2016 ANSYS, Inc., 2016. [Online]. Available: http://www.ansys.com/Products/Fluids/ANSYS-Fluent. [Accessed 29 December 2016].

[26] Fluent Inc., "Modeling Turbulence," in *FLUENT 6.1 User's Guide*, Fluent Inc., 2003, pp. 659-740.

[27] ANSYS, Inc, ANSYS Fluent User's Guide, ANSYS, Inc., 2013.

[28] J. v. Ingen, "The eN Method for Transition Prediction. Historical Review of Work at TU Delft," in *38th Fluid Dynamics Conference and Exhibit*, Seattle, 2008.

Appendix

This page has been intentionally left blank
for double side copying

Appendix I

LEEUAV Airfoil Coordinates

Upper Surface					
x	y	x	y	x	y
1.000000	0.001500	0.740877	0.068247	0.232087	0.101173
0.999753	0.001611	0.726995	0.070592	0.218958	0.099738
0.999013	0.001946	0.712890	0.072925	0.206107	0.098141
0.997781	0.002503	0.698574	0.075239	0.193546	0.096384
0.996057	0.003280	0.684062	0.077526	0.181288	0.094469
0.993844	0.004276	0.669369	0.079779	0.169344	0.092400
0.991144	0.005485	0.654508	0.081990	0.157726	0.090177
0.987958	0.006899	0.639496	0.084152	0.146447	0.087801
0.984292	0.008505	0.624345	0.086258	0.135516	0.085272
0.980147	0.010287	0.609072	0.088300	0.124944	0.082591
0.975528	0.012224	0.593691	0.090271	0.114743	0.079754
0.970440	0.014292	0.578217	0.092162	0.104922	0.076759
0.964888	0.016467	0.562667	0.093967	0.095492	0.073599
0.958877	0.018723	0.547054	0.095677	0.086460	0.070264
0.952414	0.021037	0.531395	0.097286	0.077836	0.066747
0.945503	0.023389	0.515705	0.098784	0.069629	0.063057
0.938153	0.025762	0.500000	0.100166	0.061847	0.059215
0.930371	0.028145	0.484295	0.101423	0.054497	0.055240
0.922164	0.030526	0.468605	0.102552	0.047586	0.051156
0.913540	0.032899	0.452946	0.103552	0.041123	0.046990
0.904508	0.035261	0.437333	0.104419	0.035112	0.042773
0.895078	0.037616	0.421783	0.105152	0.029560	0.038540
0.885257	0.039968	0.406309	0.105747	0.024472	0.034328
0.875056	0.042319	0.390928	0.106202	0.019853	0.030185
0.864484	0.044670	0.375655	0.106515	0.015708	0.026160
0.853553	0.047024	0.360504	0.106683	0.012042	0.022317
0.842274	0.049380	0.345492	0.106703	0.008856	0.018721
0.830656	0.051738	0.330631	0.106572	0.006156	0.015388
0.818712	0.054098	0.315938	0.106288	0.003943	0.012300
0.806454	0.056459	0.301426	0.105847	0.002219	0.009422
0.793893	0.058820	0.287110	0.105245	0.000987	0.006691
0.781042	0.061181	0.273005	0.104480	0.000247	0.003949
0.767913	0.063540	0.259123	0.103547	0.000000	0.000000
0.754521	0.065896	0.245479	0.102444		

Lower Surface					
x	y	x	y	x	y
1.000000	-0.001500	0.740877	0.017294	0.232087	-0.018512
0.999753	-0.001413	0.726995	0.016762	0.218958	-0.019427
0.999013	-0.001154	0.712890	0.016190	0.206107	-0.020273
0.997781	-0.000722	0.698574	0.015578	0.193546	-0.021049
0.996057	-0.000120	0.684062	0.014925	0.181288	-0.021752
0.993844	0.000650	0.669369	0.014232	0.169344	-0.022377
0.991144	0.001580	0.654508	0.013498	0.157726	-0.022924
0.987958	0.002659	0.639496	0.012723	0.146447	-0.023387
0.984292	0.003870	0.624345	0.011905	0.135516	-0.023764
0.980147	0.005190	0.609072	0.011046	0.124944	-0.024050
0.975528	0.006590	0.593691	0.010144	0.114743	-0.024241
0.970440	0.008036	0.578217	0.009200	0.104922	-0.024331
0.964888	0.009493	0.562667	0.008212	0.095492	-0.024315
0.958877	0.010925	0.547054	0.007181	0.086460	-0.024186
0.952414	0.012302	0.531395	0.006106	0.077836	-0.023935
0.945503	0.013595	0.515705	0.004986	0.069629	-0.023562
0.938153	0.014783	0.500000	0.003822	0.061847	-0.023071
0.930371	0.015849	0.484295	0.002614	0.054497	-0.022464
0.922164	0.016781	0.468605	0.001367	0.047586	-0.021745
0.913540	0.017571	0.452946	0.000088	0.041123	-0.020918
0.904508	0.018219	0.437333	-0.001217	0.035112	-0.019989
0.895078	0.018734	0.421783	-0.002541	0.029560	-0.018963
0.885257	0.019131	0.406309	-0.003877	0.024472	-0.017846
0.875056	0.019418	0.390928	-0.005219	0.019853	-0.016646
0.864484	0.019603	0.375655	-0.006561	0.015708	-0.015371
0.853553	0.019696	0.360504	-0.007896	0.012042	-0.014028
0.842274	0.019701	0.345492	-0.009217	0.008856	-0.012624
0.830656	0.019626	0.330631	-0.010518	0.006156	-0.011151
0.818712	0.019476	0.315938	-0.011793	0.003943	-0.009586
0.806454	0.019256	0.301426	-0.013034	0.002219	-0.007894
0.793893	0.018972	0.287110	-0.014235	0.000987	-0.006012
0.781042	0.018629	0.273005	-0.015390	0.000247	-0.003782
0.767913	0.018232	0.259123	-0.016491	0.000000	0.000000
0.754521	0.017786	0.245479	-0.017533		

Aerodynamic Analysis of a Forward–Backward Facing Step Pair on the Upper Surface of a Low-Speed Airfoil

Luís G. Freitas†
Universidade da Beira Interior, Covilhã, 6201-001, Portugal

The Long Endurance Electric Unmanned Air Vehicle (LEEUAV) is a project of a green, low-cost, small footprint electric solar UAV which was designed for civilian surveillance applications. Therefore, long endurance is desired, which is accomplished by a lightweight airframe design and an electric propulsion system assisted with solar cell arrays. To ease the construction, its wing, in addition to its aerodynamic function, must accommodate the solar cells on its upper surface. Since the solar cells have a finite thickness, they create an offset, with a forward facing step at the beginning of the solar cell array and a backward facing step at its end. The aim of this paper is to study the influence of these steps in the aerodynamic coefficients of the LEEUAV's airfoil, having as variables the offset's position, length, and thickness. To do this, a numerical analysis was performed initially using XFOIL, in which numerous combination of offsets were tested, in order to understand the range of positions that could be more appropriate for placing the solar cells. Afterwards, a small amount of combinations was chosen to perform a CFD analysis in ANSYS Fluent that served to validate and refine the results obtained from XFOIL. And the best position for placing the solar cells, based on the performed analysis, is between 21% and 23% of the airfoil's chord.

Nomenclature

c	=	chord
N	=	amplification factor
Re	=	Reynolds number
C_d	=	drag coefficient
C_f	=	skin friction coefficient
C_l	=	lift coefficient
C_m	=	pitching moment coefficient
C_p	=	pressure coefficient
C_l / C_d	=	lift-to-drag ratio
$C_l^{3/2} / C_d$	=	lift$^{3/2}$-to-drag ratio
T_u	=	turbulence intensity
x_{tru} / c	=	relative transition point on the upper surface
$(x/c)_i$	=	relative offset initial position
$(x/c)_f$	=	relative offset final position
(t/c)	=	offset thickness-to-chord ratio
y^+	=	dimensionless wall distance
α	=	angle of attack
ε	=	turbulence dissipation rate
k	=	turbulence kinetic energy
ω	=	specific dissipation rate

I. Introduction

THE global unmanned aerial vehicle (UAV) market in the last decade has witnessed an enormous growth and the market of small UAVs has high growth potential due to increasing applications in civilian and commercial sectors [1]. In another front, society never had so much interest and demand for renewable energy and technology has never been so advanced and accessible to the user. [2]

With this potential of small UAVs, renewable energies, and technological advancements, came the project of the Long Endurance Electric Unmanned Air Vehicle (LEEUAV), which main objective was to develop a low cost, small footprint long endurance electric solar UAV, with the capability of being deployed from short airfields, easy to build and maintain and with high flexibility to perform different civilian surveillance missions.

Hereupon, for ease of construction, the solar panels were to be placed over the wing instead of being embedded into its skin. As a result of this decision, the solar panel placement would certainly affect the airflow on the upper surface of the wing. Therefore, it is important to understand the influence of the solar panels on the aerodynamic coefficients of the LEEUAV's airfoil and find the best position for their placement, in order to have the least impact on the wing's aerodynamic characteristics.

The objective of this work is to analyze the influence of the solar panels on the LEEUAV's airfoil performance and to provide the best longitudinal position on the airfoil's chord for the solar panels with the view to minimize the penalties on the aerodynamic performance and achieve results closer to the ones provided by the initial design and quantify the aerodynamic performance penalty associated with placing the solar arrays on the upper surface of the airfoil.

† MSc Student, Aerospace Sciences Department, luisazevedo93@hotmail.com.

II. Concepts Identification and Problem Definition

A. LEEUAV's Airfoil

For the LEEUAV project, a new airfoil was developed using an in-house gradient based aerodynamic shape optimization tool coupled with XFOIL, as the aerodynamic analysis tool. Since the LEEUAV has a very low cruise speed, the airfoil demonstrates good performance at low Reynolds number (Re), since it is directly related with the velocity. It delivers minimum drag coefficient (C_d) in the lift coefficient (C_l) range from 0.6 to 1.5 and $C_{l_{máx}}$ higher than 1.7. It has a relative thickness of 12% and a trailing edge thickness greater than 1 mm.

B. Problem Definition

Besides its aerodynamic purpose, the LEEUAV's wing must accommodate the solar cells on its upper surface. Since the solar cells have a finite thickness, they create a localized thickening or an offset in the airfoil, with a forward facing step (FFS) at the beginning of the solar cell array and a backward facing step (BFS) at its end. Moreover, the offset gives the airfoil an increment in camber and thickness. In Figure 1, the LEEUAV's airfoil with the offset is presented.

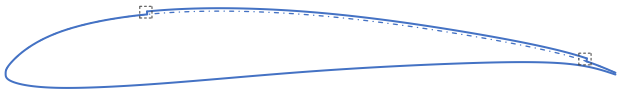

Figure 1. LEEUAV's airfoil with solar panel on its upper surface.

Given this condition, it is necessary to fully understand the influence of these steps on the airfoil performance and achieve the best position for placing the solar panels with the view to deliver the more approximated aerodynamic performance provided by the initial design.

According to the literature, it is known that, these steps may cause separation of the flow: in a the FFS flow, one or two regions of separation may occur, one upstream and one downstream, and in a the BFS flow, one separated region develops downstream of the step.

In Figure 2, the streamwise velocity fluctuations over a forward–backward facing step pair in a study performed in reference [3] can been seen, where the thick black lines represent the separations lines. The first flow separation, upstream the FFS, does not generate a significant amount of turbulence, but in the separation after the sharp corner of the FFS results in a significant increase of turbulence. Flow separation after the BFS also generates high turbulence levels, yet lower than those generated after the FFS. [3]

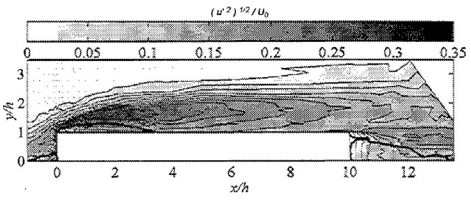

Figure 2. Streamwise velocity fluctuations [3].

C. Study Methodology

The objective of this analysis is to understand and quantify the influence of these steps in the lift coefficient, drag coefficient, pitching moment coefficient (C_m), lift-to-drag ratio (C_l/C_d), lift$^{3/2}$-to-drag ratio ($C_l^{3/2}/C_d$) and transition point on the upper (x_{tr_u}/c) and lower surfaces, for $Re\sqrt{C_l} = 150{,}000$, corresponding to cruise altitude conditions.

First, using XFOIL it is intended to obtain the airfoils polar curves. To compare with the performance of the clean airfoil, several airfoils must be created containing an offset. The beginning of the offset, the FFS, will have the designation of the offset initial position, $(x/c)_i$, and the end of the offset, the BFS, as the offset final position, $(x/c)_f$, and the offsets will have a thickness-to-chord ratio, (t/c). These parameters vary according to the intervals and increments in Table 1.

Table 1. Offset geometrical parameters.

Parameter	Minimum	Maximum	Increment
$(x/c)_i$	0.10	0.50	0.05
$(x/c)_f$	0.30	0.95	0.05
(t/c)	0.0025	0.01	0.0025

In the second part of the work is intended to *1)* choose a few of the solar panels positions analyzed in XFOIL, *2)* perform a computational fluid dynamics (CFD) analysis using ANSYS Fluent to validate and refine the results obtained from XFOIL, *3)* visualize the airflow over the airfoil to better understand the influence of the solar panels in the airflow.

III. XFOIL Numerical Analysis

A. XFOIL Description

XFOIL is an interactive program for the analysis of subsonic isolated airfoils. Its code combines a potential flow panel method and an integral boundary layer formulation for the analysis of flows around airfoils and its convergence is achieved through the iteration between the outer and inner flow solutions on the boundary layer displacement thickness. XFOIL uses an approximate e^N envelope method to calculate transition. In the present work, N was set to default value of 9, which corresponds to a smooth wing surface in a low turbulence intensity freestream. [4]

In this work, a type 2 analysis was used, which corresponds to an aircraft in level flight at a given altitude undergoing trim speed changes in which the parameter $Re\sqrt{C_l}$ is held constant.

B. Numerical Procedure

1. Airfoils Conception

XFOIL reads labeled coordinate files, which contains a name string on the first line and bellow the x,y coordinates, which run from the trailing edge (TE), round the leading edge (LE), back to the trailing edge, in either direction.

The easiest and most efficient way of creating the different airfoils incorporated with offsets is to use

Microsoft Excel. In its spreadsheet, the values for the offset parameters, are established, and, from there, the spreadsheet reads the LEEUAV's airfoil coordinates and identifies, in the upper surface, if the coordinates are between the initial and final limit of the offset. Then, it generates new coordinates, the ones that are inside the limits of the offset, adds an increment so that the spreadsheet creates the offset. The ones which are not within its limits remain the same as the original coordinates.

For data organization, each new airfoil receives the codename "LEEUAV ($(x/c)_i$; $(x/c)_f$; (t/c))", an example is presented in Figure 3.

Figure 3. LEEUAV (0.20;0.60;0.005).

With a script in Visual Basic for Applications, it was possible for Excel automatically combine every option of $(x/c)_i$, $(x/c)_f$ and (t/c), and for each combination, create and save the coordinates with the respective codename in a DAT file, so that could be subsequently analyzed by XFOIL.

The setback of this procedure is that the steps are not forming a 90-degree angle with the airfoil's upper surface, which under predicts the damage caused by the offset and for small (t/c), the panel angle in the steps' location is so small that XFOIL may not assume it as a step, but only as an increase in thickness. On the other hand, a high panel angle induces in convergence problems and program errors in XFOIL, which are reflected in the offsets with greater (t/c), as it is demonstrated ahead.

2. XFOIL Simulation Procedure

XFOIL has an user command line interface and it was automated with a Matlab script for the analysis procedure, thus running the simulation for the several airfoils. A viscous type 2 analysis for $Re\sqrt{C_l} = 150{,}000$ was performed, for a range of angles of attack from -3 deg to 15 deg.

C. Results and Discussions

The most important points drawn from the analysis are presented next and it is critical to pay special attention to the design C_l range from 0.6 to 1.5. Most of the results are presented for (t/c) equal to 0.005, since these are more visible, thus facilitating comprehension.

1. Excessive Thickness-to-Chord Ratio

Four (t/c) were analyzed, respectively 0.0025, 0.005, 0.0075 and 0.01. For the last two, XFOIL did not converge for every angle of attack, and, in some cases, the program even crashed. This may have been caused by the excessive panel angle in the steps' location, which, in some cases, reached 50 deg.

Only 68% and 24% of the offsets combinations with (t/c) equal to 0.0075 and 0.01, respectively converged with adequate polar points (40%), thus becoming extremely difficult to draw conclusions. In Figure 4, the C_l/C_d curve for the clean airfoil and for offsets combinations with different (t/c) is presented. It is evident that there is a huge lack of polar points for the two greater (t/c).

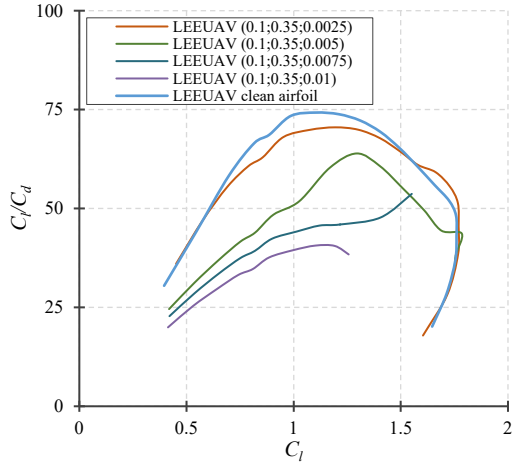

Figure 4. C_l/C_d at $Re\sqrt{C_l} = 150{,}000$ for the LEEUAV's clean airfoil and for different offset combinations with different (t/c).

Nevertheless, it clearly shows that the greater (t/c) are extremely prejudicial to the airfoil performance, with increases of up to 80-85% of C_d in the design C_l range from 0.6 to 1.5, and losses of 20-25% of C_l compared to the clean airfoil. It is clear that the influence in the airfoil performance is proportional to the increase in (t/c) of the offset.

2. Premature Forced Transition

When analyzing the results, one position pops out from the others in any (t/c): the $(x/c)_i$ at 0.10 of the airfoil's chord, that is, the FFS positioned at 10% of the airfoil's chord. In Figure 5, an example with offsets with various initial positions and the same final position at 0.95 of the chord is presented.

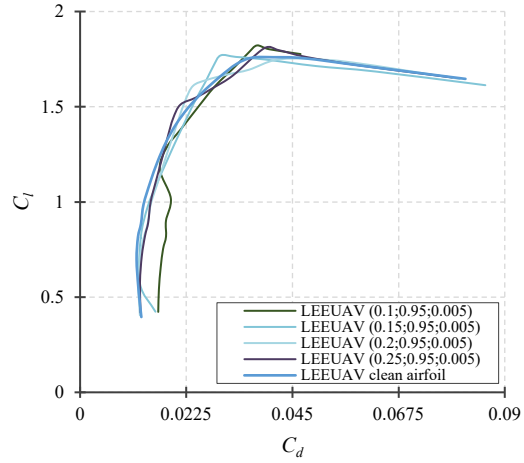

Figure 5. Drag polar at $Re\sqrt{C_l} = 150{,}000$ for the LEEUAV's clean airfoil and for different offset combinations with $(t/c) = 0.005$.

Observing the drag polar, it is evident that the $(x/c)_i$ at 0.10 of the chord, for C_l lower than 1.2, stands out from the others, with increase in the C_d and, although it is not demonstrated here, decrease in the C_l. The $(x/c)_i$ at 0.15

of the chord also shows increase in the C_d, but only for C_l lower than 0.6. The reason for this discrepancy, seen in Figure 6, is due to the FFS forcing the transition of the flow in the upper surface from laminar to turbulent, shortly after the step's location for low C_l. In the lower surface, the influence of the offset is negligible.

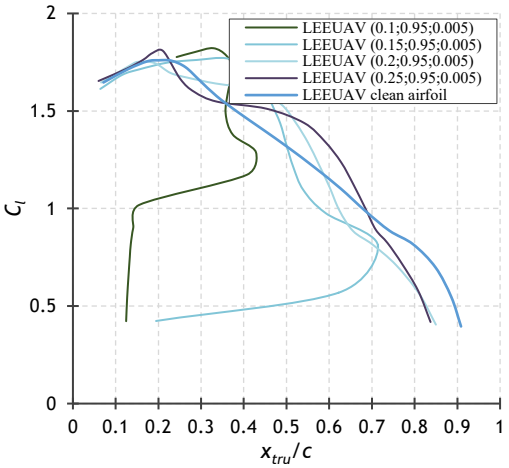

Figure 6. x_{tru}/c at $Re\sqrt{C_l}$ = 150,000 for the LEEUAV's clean airfoil and for different offset combinations with (t/c) = 0.005.

In Figure 7, a comparison between the pressure coefficient (C_p) distribution about the airfoil for the LEEUAV clean airfoil and for the LEEUAV (0.10;0.95;0.005) is presented. The "x" represents the transition point.

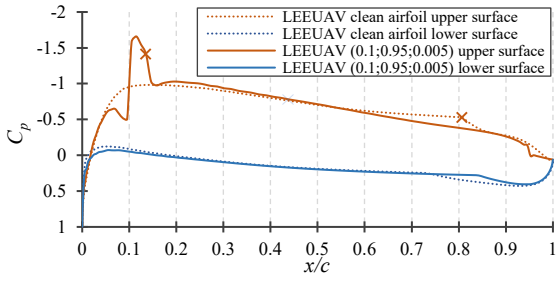

Figure 7. C_p distribution at $Re\sqrt{C_l}$ = 150,000 for C_l = 0.8 for the LEEUAV clean airfoil and for the LEEUAV (0.10;0.95;0.005).

Regarding the upper surface, the pressure field experiences the normal drop at the LE due to the acceleration of the fluid over the airfoil's curvature. As referred in section "II. B. Problem Definition", there is a separation upstream and downstream of the FFS. Upstream of the step, there is an adverse pressure gradient which causes separation, and in the step location, originated by the acceleration of the fluid over the step, occurs a large decrease in the pressure field, followed downstream by a severe adverse pressure gradient which causes separation and transition of the flow.

Concerning the BFS, it is visible that after the step, separation occurs through the adverse pressure gradient. When the flow travels past the BFS, it creates a low-pressure recirculation zone and the sudden reduction in the airfoil thickness after the step, relatively decreases the flow velocity, which results in a subsequent high pressure region stretched to the TE of the airfoil.

3. Forward Facing Step Too Far Behind

Another set of $(x/c)_i$ that also severely damage the performance at low C_l, are the offsets beginning after 0.30 of the chord. These affect the performance for C_l below 1, and the effects increase as the $(x/c)_i$ moves further away from the LE.

The reason for this divergence can be seen in Figure 8, where a comparison of the skin friction coefficient (C_f) distribution over the upper surface between the clean airfoil and the LEEUAV (0.50;0.95;0.005), is presented. The clean airfoil and the airfoil with the offset beginning at 0.50 of the chord exhibit similar C_f until around 0.30 of the chord. Upstream of the FFS, for the airfoil with offset, the C_f drops to zero in the separation point and is followed by a concaved down curve confining the recirculation zone. In the step's location, the C_f increases exponentially, originating a high C_f zone, which increases the total C_d in relation to the clean airfoil.

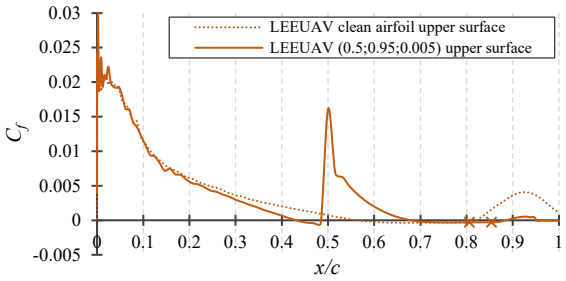

Figure 8. C_f distribution on the upper surface at $Re\sqrt{C_l}$ = 150,000 for C_l = 0.8 for the LEEUAV clean airfoil and for the LEEUAV (0.50;0.95;0.005).

4. Backward Facing Step Influence

The $(x/c)_f$ does not have significant impact on the airfoil performance, when compared to the initial position. Nevertheless, the $(x/c)_f$ still has some degrading performance positions, where the BFS forces the transition of the flow in the upper surface from laminar to turbulent. This is regarding to the $(x/c)_f$ prior to 0.80 of the airfoil's chord and the further away from the TE the $(x/c)_f$ is, the sooner transition occurs.

In Figure 9, a comparison between the C_p distribution over the airfoil of the LEEUAV clean airfoil and of the airfoil with the $(x/c)_f$ at 0.40 of the airfoil's chord, is presented.

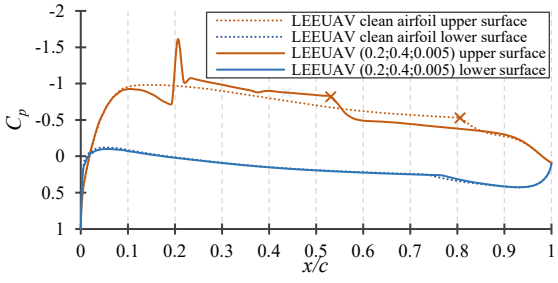

Figure 9. C_p distribution at $Re\sqrt{C_l}$ = 150,000 for C_l = 0.8 for the LEEUAV clean airfoil and for the LEEUAV (0.20;0.40;0.005).

The effects of the BFS in the C_p are not very noticeable, but after the BFS location, the C_p remains constant, caused by a laminar separation bubble, and, then, flow transition occurs.

The remaining positions for the $(x/c)_f$, between 0.80 and 0.95 of the airfoil's chord, deliver the best performance with minor differences between them. When comparing to the influence of the $(x/c)_i$, the influence of the $(x/c)_f$ is negligible.

5. Forward Facing Step Effects

The $(x/c)_i$ between 0.20 and 0.30 of the airfoil's chord delivers the best performance within the damage and presents similar maximum differences for each aerodynamic coefficient that are explained ahead. For the most relevant aerodynamic coefficient, the polar graph is presented, accompanied with a chart showing the differences. These differences, presented in percentage, are between the aerodynamic coefficient of the clean airfoil and those of the airfoils incorporated with offsets.

For these positions, the effects related with the increase in airfoil thickness and camber are evident. In Table 2, the airfoils geometric characteristics regarding thickness and camber for the (t/c) equal to 0.005 is presented. The offset gives an increase in thickness and camber, proportional to the offset (t/c), which has the associated effects. The offset beginning at 0.30 of the chord has different thickness than at 0.20 and 0.25, and this is visible in the polar graphs, where the curve of the $(x/c)_i$ at 0.30 of the chord does not follow the trend and swaps with the C_l and C_m curve of the offset with $(x/c)_i$ at 0.25. This is demonstrated ahead.

Table 2. Airfoils geometric characteristics.

LEEUAV's airfoils			Thickness [%]	Camber [%]
Clean airfoil			12	5.2
$(x/c)_i$	$(x/c)_f$	(t/c)		
0.20	0.95	0.005	12.5	5.45
0.25				
0.30			12.39	

In regard of C_d, which is the most affected aerodynamic coefficient, the polar curve moves upward and to the right, due to the increase in camber and thickness [5], thus, showing ranges of C_l where the C_d is lower than the one regarding to the clean airfoil. In relation to (t/c) equal to 0.005, in Figure 10, there is a visible increase in the C_d, but smaller than 15%.

The variation of the C_d by the airfoils incorporated with offsets can be divided in four regions, within the C_l, that vary according to the (t/c) of the offset:

- $C_l >$ ~ 1.5, where the $(x/c)_i$ furthest away from the LE increases C_d;
- ~ 0.8-1.2 < $C_l <$ ~ 1.5, where the $(x/c)_i$ closest to the LE increases C_d (this C_l bottom limit tends to increase with the decrease of the (t/c));
- ~ 0.3-0.7 < $C_l <$ ~ 0.8-1.2, where the $(x/c)_i$ furthest away from the LE increases C_d (this C_l limits tend to increase with the decrease of the (t/c));
- $C_l <$ ~ 0.3-0.7, where the $(x/c)_i$ closest to the LE increases C_d (not visible in this (t/c)).

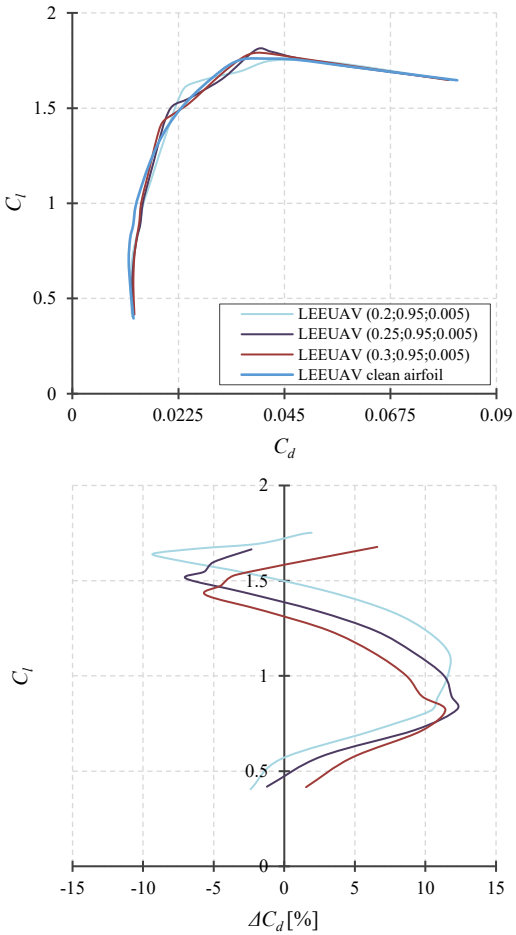

Figure 10. Drag polar at Re$\sqrt{C_l}$ = 150,000 for the LEEUAV's clean airfoil and for different offset combinations with (t/c) = 0.005 (on the top) and its corresponding differences (on the bottom).

Concerning C_l, in Figure 11, the linear portion of the C_l curve moves to the left, due to the increase in camber [5]. The variation is not significant, around 5%, and it shows ranges of angles of attack with an increase in C_l, compared to the clean airfoil, due to the increase in camber.

The difference in the C_l can be divided into two regions within the range of angles of attack:

- $\alpha >$ ~ 6 deg, where the $(x/c)_i$ furthest away from the LE decreases C_l (with oscillation close to α = 8 deg);
- $\alpha <$ ~ 6 deg, where the $(x/c)_i$ closest to the LE decreases C_l (a mix-up is visible between the $(x/c)_i$ at 0.25 and 0.30 of the chord, caused by a small difference in airfoil thickness).

The influence in the $C_{l_{máx}}$ does not present great variation in the absolute value, less than 2.4%, never being lower than 1.7. The maximum angle of attack also does not change significantly, with a difference always lower than 1 deg.

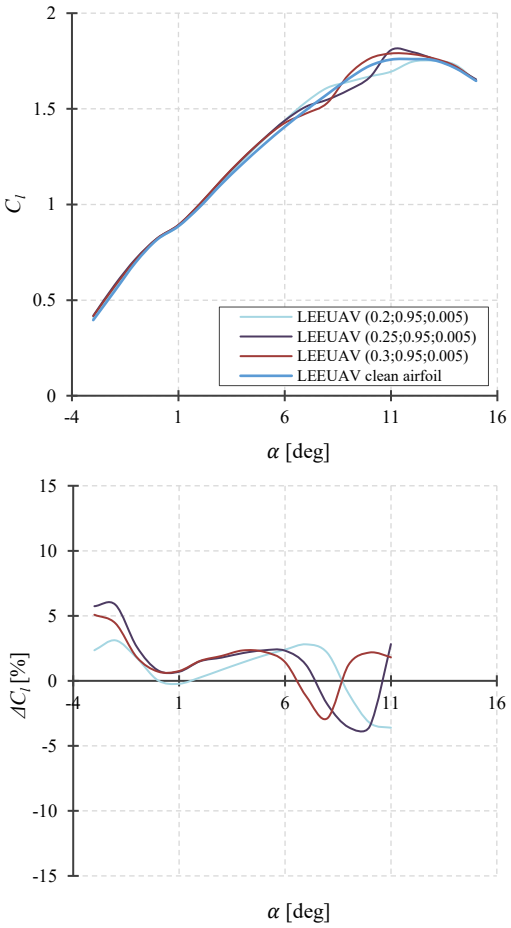

Figure 11. C_l curve at $Re\sqrt{C_l}$ = 150,000 for the LEEUAV's clean airfoil and for different offset combinations with (t/c) = 0.005 (on the top) and its corresponding differences (on the bottom).

The C_m is also less affected by the presence of the offset, but slightly more affected than the C_l. The C_m curve moves downwards due to the increase in lift. The discrepancy in the C_m can be divided in two regions within the C_l, identical to the discrepancy of the C_l and with the same relationship with the $(x/c)_i$. The variation in this aerodynamic coefficient does not have great influence in the overall performance, being the drag and C_l much more significant. Hereupon, the C_m should not have great influence in the decision of the best positions for placing the offset.

Concerning C_l/C_d and $C_l^{3/2}/C_d$, both have similar tendency, so they can be grouped together. Basically, moving the $(x/c)_i$ closest to the LE, the curve rotates clockwise, existing C_l regions where the ratio is higher than the one of the clean airfoil. The predominating effects are the ones found in the C_d, proving that the C_d is the aerodynamic coefficient most affected by the offsets presence. The variation of these performance ratios by the airfoils with offsets can be divided in four regions within the C_l, that vary according to the (t/c) of the offset, identical to the variation in the C_d:

- $C_l >$ ~ 1.5, where the $(x/c)_i$ furthest away from the LE decreases C_l/C_d;
- ~ 0.8-1.2 < C_l < ~ 1.5, where the $(x/c)_i$ closest to the LE decreases C_l/C_d (this C_l bottom limit tends to increase with the decrease of (t/c));
- ~ 0.3-0.7 < C_l < ~ 0.8-1.2, where the $(x/c)_i$ furthest away from the LE decreases C_l/C_d (this C_l limits tend to increase with the decrease of (t/c));
- $C_l <$ ~ 0.3-0.7, where the $(x/c)_i$ closest to the LE decreases C_l/C_d (not visible for this (t/c)).

6. *LEEUAV's Solar Cells*

Now that the general conclusions about offsets on the upper surface of the LEEUAV's airfoil have been drawn, a comparison between the possible best positions with the precise thickness of the solar cells is presented.

The solar cells best possible positions will be between 0.20 and 0.25 of the airfoil's chord. For the most important aerodynamic coefficient, the differences chart is presented. These differences, as seen before, are presented in percentage and relate to the difference in the aerodynamic coefficient compared to the clean airfoil. The design C_l limits are showed in dashed lines.

The problem with this magnitude of (t/c) (0.001), is that the panel angle is very reduced in the step's location, resulting in less precise results. The main objective in this part of the work is to determine the best position to place the solar panels and not so important the value of the influence, regarding the clean airfoil, because this value will be "corrupted" by the reduced panel angle in the step's location.

The most important C_l range of operation for the LEEUAV is the design C_l range from 0.6 to 1.5, and particularly from 0.6 to 1. Below that, it is also important to have a good performance, due to the maximum speed, and the least important range is the C_l above 1.5. Moreover, the $C_{l_{máx}}$ variation is negligible, so the effects above 1.5 are omitted. It is more important to ensure that the C_d is minimum.

Regarding C_d, in Figure 12, its variation by the airfoils incorporated with offsets can be divided in three important regions within the C_l:

- Lower speeds: ~ 1.2 < C_l < ~ 1.5, where the $(x/c)_i$ closest to the LE increases C_d;
- Medium speed: ~ 0.7 < C_l < ~ 1.2, where the $(x/c)_i$ furthest away from the LE increases C_d;
- Higher speed: $C_l <$ ~ 0.7, where the $(x/c)_i$ closest to the LE increases C_d.

The biggest variation between positions is for higher and medium speeds. So, the extreme positions should be put apart, since they exhibit the highest C_d in higher or medium speeds. More specifically, the offset beginning at 0.25 of the airfoil's chord presents greatest C_d in almost all the design C_l, and for the offset beginning at 0.20, there is a rapid increase of C_d for lower C_l, which will correspond to maximum speed, hereupon these two positions will be omitted.

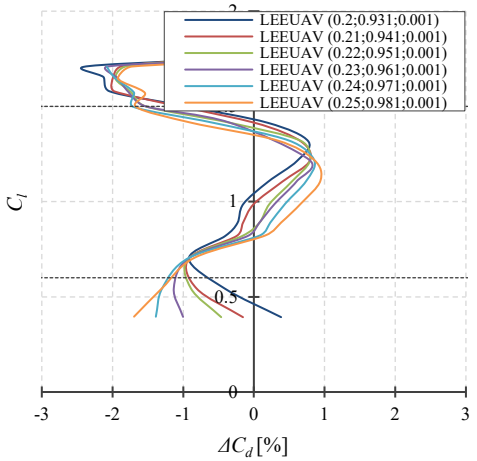

Figure 12. Drag polar corresponding differences at $Re\sqrt{C_l} = 150{,}000$ for the LEEUAV's clean airfoil and for different offset positions with similar characteristics as the solar cells.

In respect to the C_l, in Figure 13, the variation is minimal, and the difference in the C_l only has one important region:

- Lower, medium and higher speeds: $\alpha < \sim 6$ deg, where the $(x/c)_i$ closest to the LE decreases C_l.

For this coefficient, the best position is the one furthest from the leading edge, but with very little difference between them, reinforcing that the decision for the best position should be taken based on the C_d performance.

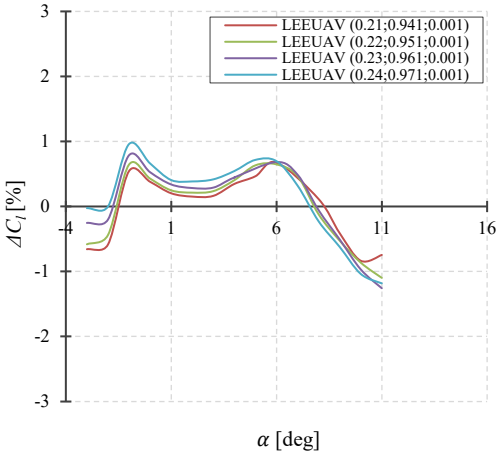

Figure 13. C_l corresponding differences at $Re\sqrt{C_l} = 150{,}000$ for the LEEUAV's clean airfoil and for different offset positions with similar characteristics as the solar cells.

The C_l/C_d, can be divided in three important regions within the C_l very similar to the C_d variation:

- Lower speeds: $\sim 1.2 < C_l < \sim 1.5$, where the $(x/c)_i$ closest to the LE decreases C_l/C_d;
- Medium speed: $\sim 0.7 < C_l < 1.2$, where the $(x/c)_i$ furthest away from the LE decreases C_l/C_d;
- Higher speed: $C_l < \sim 0.7$, where the $(x/c)_i$ closest to the LE decreases C_l/C_d.

It is not evident which positions are best, but the larger variation between them is for C_l lower than 0.7, where the position at 0.24 of the chord shows lower C_d. But positioning the offset at 0.24 of the chord has, as consequence, the final offset position at 0.971 of the chord, where it demonstrates a high curvature in the TE of the airfoil. In the region around $C_l = 1$, the mid C_l of the design range, the best position is the $(x/c)_i$ at 0.21 of the chord, that exhibits best C_d performance.

So, the best position for placing the solar cells, is between 0.21 and 0.23 of the airfoil's chord.

IV. Computational Fluid Dynamics Analysis

A. Turbulence Models Description

ANSYS Fluent was chosen to perform the CFD analysis. It provides a diverse choice of turbulence models, and for this work, the most suitable solution would be to choose a model, with three or four equations, with boundary layer transition detection capability, but with the time and computational resources available, the best solution was to use a simpler two equation turbulence models, with the limitation of not predicting transition.

1. Realizable k-ε Turbulence Model

The standard *k-ε* model is a semi-empirical model based on model transport equations for the turbulence kinetic energy (k) and its dissipation rate (ε). The Realizable *k- ε* provides the best performance of all the *k-ε* models versions, providing better performance for flows involving rotation, boundary layer under strong adverse pressure gradients, separation, and recirculation. [6]

2. Shear-Stress Transport k-ω Turbulence Model

The standard *k-ω* model is an empirical model based on model transport equations for the turbulent kinetic energy (k) and the specific dissipation rate (ω). The SST *k-ω* model was developed to effectively blend the robust and accurate formulation of the *k-ω* model in the near-wall region, with the free-stream independence of the *k-ε* model in the far field. It is more accurate and reliable for a wide class of flows, like the low Reynold number airfoil flows, than the standard model. [6]

B. Numerical Procedure

1. Geometry and Mesh Generation

The geometry for the different airfoils was designed using ANSYS DesignModeler, in which, unlike the XFOIL analysis, the FFS and BFS can form a 90-degree angle with the airfoil's upper surface. Therefore, there is no limitation to the geometry.

For the mesh generation, ANSYS Meshing was used. After several thorough studies on mesh quality and convergence, a final compromise was met, and the solution was to use a hybrid O-type mesh. It had the outer boundaries placed 35 chords away from the airfoil and, in addition to the global control volume, a smaller elliptical control volume was employed near the airfoil in the mesh generation process, which is the unstructured part of the mesh. The airfoil was defined with 1,000 divisions around its contour and a bias factor was employed to place smaller divisions around the LE and TE and in the steps' location. Special attention was given to the boundary layer region

to ensure that the first point of the mesh corresponds to a y^+~1, and, for this, an inflation layer was used all around the airfoil. The final meshes have approximately 170,000 elements.

2. Boundary Conditions and CFD Simulation Procedure

To simulate the airfoils at the desired flow conditions, of $Re\sqrt{C_l}$ = 150,000 as the XFOIL simulation, a density-based and steady state solver was used. The inlet was represented by a velocity inlet, using the velocity magnitude to prescribe the flow speed, and the outlet was represented by a pressure outlet. The desired angle of attack was obtained using the appropriate flow direction vector components. The airfoil top and bottom surfaces were defined, as wall boundary conditions, and the fluid inside the domain was defined as air with $\rho = 1.225$ kg/m^3 and $\mu = 1.789 \cdot 10^{-5}$ Pa s. These procedures give the advantage of simulating all angles of attack using only a single mesh. A second order discretization was set for the flow and turbulence equations, and convergence was achieved by monitoring the residual monitors of the solution, as it dropped below $1 \cdot 10^{-6}$ for all equations.

To achieve the appropriate flow conditions of $Re\sqrt{C_l}$ = 150,000, for each angle of attack, from -3 deg to 15 deg, since is not automatic like in XFOIL, it was employed a Direct Optimization, so that the velocity was able to vary until the product of $Re\sqrt{C_l}$ was equal to the desired value.

C. Results and Discussions

The CFD results are divided into four parts: *1)* selection of the most suitable turbulence model for the analysis; *2)* comparison of the results from XFOIL and from ANSYS Fluent; *3)* analysis of the possible positions for the LEEUAV's solar cells; *4)* visualization of the steps' effects in the airflow over the airfoil.

1. Turbulence Model Study

For the CFD analysis, two turbulence models were tested: The Realizable k-ε model and the SST *k-ω* model. With the SST *k-ω* model two options were tried, the default one and the low-Reynolds-number (Low-*Re*) correction, in which were included corrections that improve the accuracy in predicting Low-*Re* flows [7].

For the SST *k-ω* model with Low-*Re* corrections not every angle of attack was calculated, because, for higher angles of attack, the steady state solver did not converge, since vortex shedding was very active, that, in turn, produced grave oscillations in the pressure field about the airfoil [8]. As a consequence, it was necessary to use transient state solver, which exponentially increased the computational cost.

None of the turbulence models produces accurate results with the XFOIL's solution, but since the most important aspect in this study is the comparison of the results between the clean airfoil and the airfoils with offsets, the turbulence model should be chosen considering the polar curves shape and not the absolute value, that is the model that best resembles the XFOIL's solution.

The Realizable *k-ε* model, from all the above models, is the one which overpredicts C_d the most. But regarding C_l, it delivers more accurate results in the linear portion of the C_l curve, but it does not predict well $C_{l_{máx}}$, overpredicting it for an angle of attack higher than 15 deg. The SST *k-ω* model presents better results in the C_d prediction than the Realizable *k-ε* model, being the Low-*Re* correction that presents the best results. This model, with and without Low-*Re* corrections, under predicts the C_l with very similar results for both options. In addition, since none of the models predicts transition, none of them predicts the corners of the low drag region.

The results for the C_d performance are presented in Figure 14, where the comparison of the drag for the LEEUAV's airfoil obtained from XFOIL and from Fluent is shown.

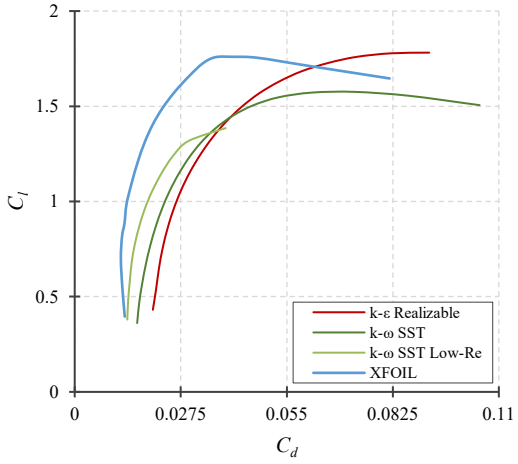

Figure 14. LEEUAV's airfoil drag polar for $Re\sqrt{C_l}$ = 150,000 for XFOIL and for ANSYS Fluent.

Taking all the considerations into account, the most suitable model to use in this work is the SST k-ω model, with better results than the Realizable k-ε model, and considerable less computational costs than the SST k-ω model Low-*Re*, despite less accurate results.

As previously stated, XFOIL uses an approximate e^N envelope method to calculate transition, in which N can be calculated by Eq. (1), as presented by van Ingen [9], where T_u represents the absolute turbulence intensity. In order to approximate the solution from XFOIL to Fluent, it is possible to increase T_u within XFOIL by decreasing N. The minimal value allowed by XFOIL is 0, in which turbulent flow is present in all the airfoil's chord.

$$N = -8.43 - 2.4 \ln T_u \quad (1)$$

In Figure 15, a comparison between the used N's default value of 9 and the minimal value allowed by XFOL with the turbulence model chosen in Fluent is presented.

For the XFOIL results with N = 0, the results are in good agreement with the Fluent's solution, noticing that the turbulence model used is fully turbulent.

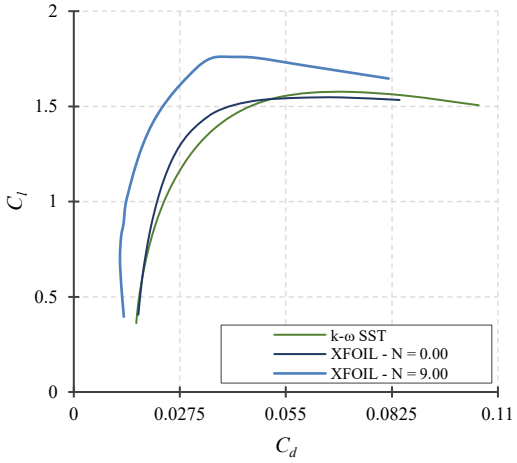

Figure 15. LEEUAV's airfoil drag polar for $Re\sqrt{C_l} = 150{,}000$ for different N values in XFOIL and for the SST k-ω model in ANSYS Fluent.

2. XFOIL Results Comparison

Next, the comparison between the results obtained from XFOIL and from Fluent for the LEEUAV clean airfoil and for airfoils with offsets are presented. The scale of the polar graphs for the results obtained with Fluent is different from the ones with XFOIL, so that, the results are more similar between them.

In Figure 16, the drag polar curve for both software programs is presented. As it was predicted, the results are more similar for greater (t/c), because, in XFOIL, the greater (t/c), the higher the panel angle in the steps' location and the more trustworthy is the step's geometry.

The results from Fluent are in reasonable agreement with the ones from XFOIL, emphasizing two details: first, since it was used a turbulence model without the capabilities to calculate transition, the curves are smoother than the ones from XFOIL. The decrease in C_d seen in the XFOIL's drag polar for the offset with (t/c) of 0.005 as the C_l rises is not present in the Fluent results. Second, for smallest (t/c) in XFOIL, it does not present great difference from the clean airfoil, though in Fluent it does, specially (t/c) of 0.0025 that in XFOIL the results are very similar to the clean airfoil. This is due to the small panel angle in the steps' location, existing in the XFOIL geometry, that in Fluent is a perfect 90-degree step.

With the C_l curve is the same outcome. The results in Fluent are in reasonable agreement with the ones obtained from XFOIL. For Fluent results, the curves are smoother and unlike the XFOIL results, the C_l for the airfoils with offsets presents very similar performance to the clean airfoil for low angles of attack. Furthermore, a detail that was not possible to realize in the XFOIL results, due to the scarcity of point in the greater (t/c), is that the $C_{l_{máx}}$ is inversely proportional to (t/c).

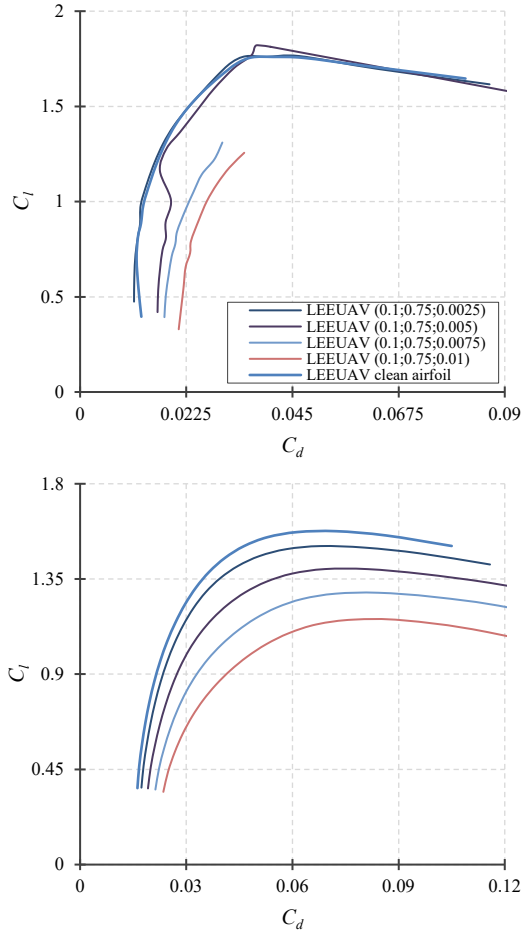

Figure 16. Drag polar at $Re\sqrt{C_l} = 150{,}000$ for the LEEUAV's clean airfoil and for different offset combinations obtained from XFOIL (on the top) and from ANSYS Fluent (on the bottom)

An important aspect, highlighted in the XFOIL analysis, is the relationship between the different offsets' positions. These are demonstrated in Figure 17, where the C_l/C_d's corresponding differences chart is presented, as previously seen in the XFOIL analysis. These are related to the offsets with (t/c) of 0.005 with $(x/c)_i$ of 0.20 and 0.30.

The relationship between the different offsets' positions are in good agreement for both software programs. Higher C_l are the exception, that in the XFOIL results the C_l/C_d curves crosses each other, which in the Fluent results it does not happen. The variation of the C_l/C_d by the airfoils with offsets with (t/c) equal to 0.005, can be divided in two regions, not three like the XFOIL results, within the C_l. Also, it is visible that the performance differences are more degrading, as we move towards lower C_l, unlike the XFOIL, that were higher than the clean airfoil in some C_l ranges and lower in others.

In the case of the XFOIL results, for smaller (t/c), the increase in thickness and camber, caused by the offset, has visible effects in the increase of the C_l and decrease of the C_d in some ranges of C_l. But in Fluent, the performance with the offset presence are always worse. The steps' effects are always greater than the ones from the increase in camber and thickness.

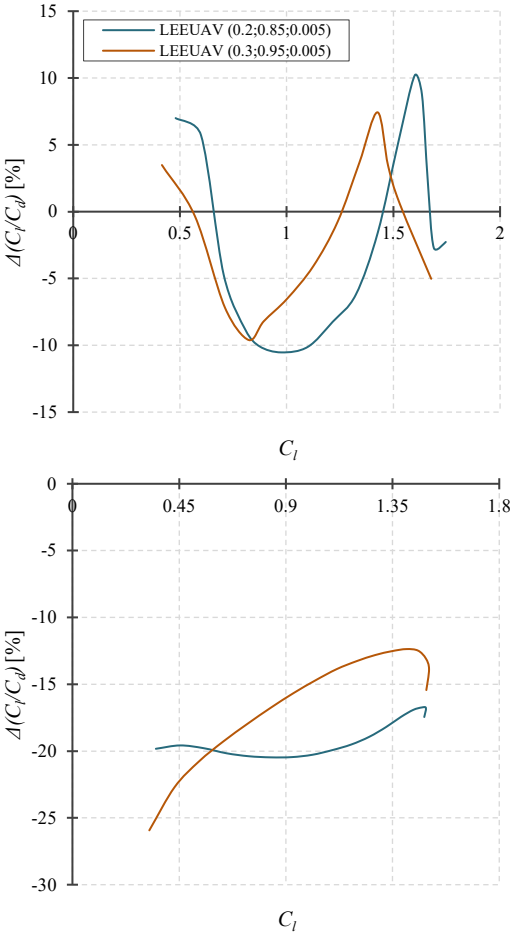

Figure 17. C_l/C_d's corresponding differences at $Re\sqrt{C_l}$ = 150,000 for the XFOIL results (on the top) and for Fluent results (on the bottom).

Figure 18 display a comparison of the C_p distributions between the results obtained from XFOIL and Fluent for a 3 deg angle of attack.

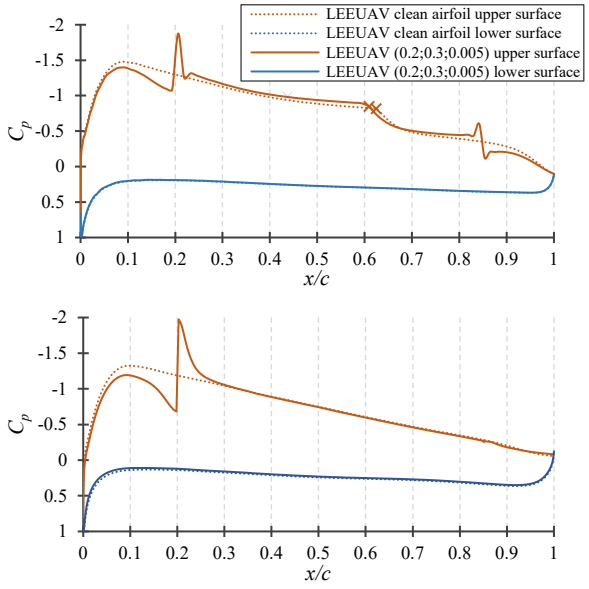

Figure 18. C_p distribution at $Re\sqrt{C_l}$ = 150,000 for α = 3 deg for the LEEUAV clean airfoil and for the LEEUAV (0.20;0.85;0.005) for XFOIL results (on the top) and for Fluent results (on the bottom).

The results are in good agreement for the first half of the airfoil's chord, after that, the results from Fluent do not show a significant change in the C_p over the BFS, as does XFOIL results. The decrease in C_p over the FFS, in the Fluent results, is more accentuated than the XFOIL results. This is due to the step's geometry, that in Fluent is a 90-dregre step, unlike the XFOIL.

3. LEEUAV's Solar Cells

For the LEEUAV's solar cells, all six possibilities for the solar cells' positions were tested. The results confirmed the outcome from the XFOIL analysis that the best positions for placing the offset is between 0.21 and 0.23 of the chord.

As previously said, the results from XFOIL showed regions where the airfoils with offsets show better performance than the clean airfoil. To the Fluent results, the relationship between positions remain the same, but the difference in respect to the clean airfoil are different. This is caused by the small (t/c), which caused extremely small panel angle in the steps' location in XFOIL, and, therefore, less precise results. With a 90-degree steps in Fluent, the results from the airfoils with offsets are always worse than the ones from the clean airfoil.

As for the C_d for the best three positions, the results are very similar between them. Showing that any of the three positions deliver best performance for the C_d between all options of positions. The penalty in the C_d is more pronounced for lower C_l, which means that as velocity increases. The increases in the C_d for the C_l range tested vary from approximately 0.1% to 3.1%.

Regarding C_l the results are also very similar for the three best positions for placing the solar panels. Even so, the $(x/c)_i$ at 0.23 of the chord presents slightly better results than the alternatives. Alike the C_d, the penalty in the C_l is also more pronounced for higher speeds. The decreases in the C_l for the range of angles of attack tested vary from approximately -0.4% to -2.1%.

In Figure 19, the results regarding C_l/C_d are presented.

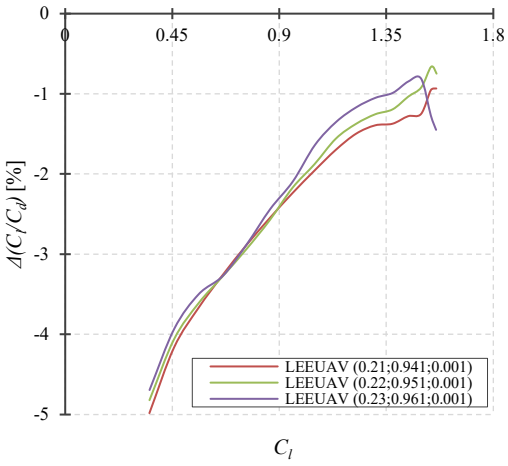

Figure 19. C_l/C_d corresponding differences at $Re\sqrt{C_l}$ = 150,000 for the LEEUAV's clean airfoil and for the best offset positions with the same characteristics as the solar cells.

As seen in the XFOIL analysis for the C_l/C_d, as well as the C_d, there is not a position that delivers the best

performance for all the C_l range. But the little difference from the C_l for the $(x/c)_i$ at 0.23 of the chord makes a difference in C_l/C_d, delivering the best performance from the three positions at almost all C_l range. The penalty associated to C_l/C_d for the C_l range tested vary from approximately -0.7% to -5%.

4. Step's Effects

Figure 20 shows a comparison of the velocity magnitude contour for the LEEUAV clean airfoil and for airfoils with offsets for the four-principal (t/c) under the same flow speed and at the same angle of attack of 3 deg.

The steps' effects in the flow are perfectly visible as described in section "II. B. Problem Definition": the FFS creates two separations regions, one upstream and one downstream; and the BFS creates a separation region downstream, that is extended to the TE for greater step's height.

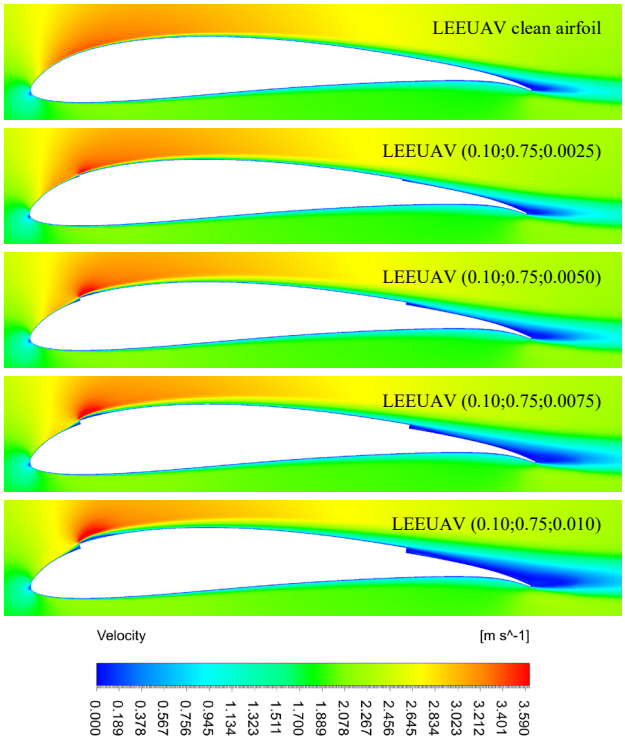

Figure 20. Comparison of velocity magnitude contour under an angle of attack of 3 deg at Re = 150,000 between computed results for the LEEUAV clean airfoil and for the airfoil with offsets for the four-principal (t/c).

The size of these separation regions is proportional to the steps' height. The features of the FFS and BFS can be seen in detail in Figure 21, with the flow streamlines evidencing the separation regions. In Figure 22, a comparison of the turbulence kinetic energy between the clean airfoil and airfoils with offsets in different positions is shown. These offsets have a (t/c) of 0.005 and the airfoils are subjected to the same flow conditions at an angle of attack of 3 deg. As concluded with the XFOIL analysis, and mentioned in section "II. B. Problem Definition", the separation downstream of the FFS generates the highest levels of turbulence, showing that the FFS position ($(x/c)_i$) is the most important aspect when choosing the position of the offset (solar cells).

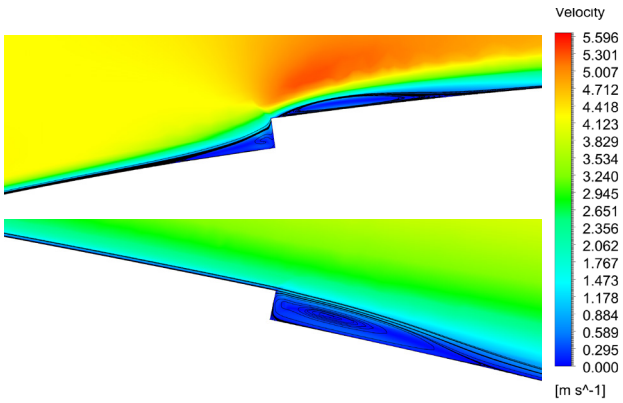

Figure 21. Detail of flow streamlines with velocity contour under an angle of attack of -3 deg at Re$\sqrt{C_l}$ = 150,000 for the FFS and BFS of the LEEUAV (0.20;0.85;0.005).

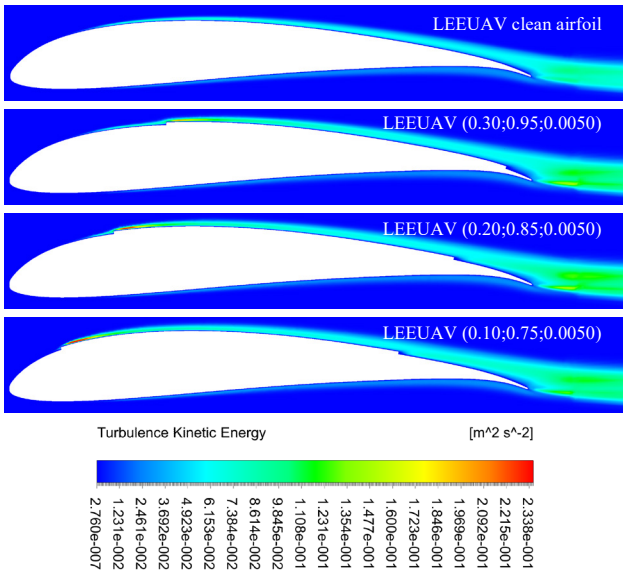

Figure 22. Comparison of turbulence kinetic energy under an angle of attack of 3 deg at Re = 150,000 between computed results for the LEEUAV clean airfoil and for the LEEUAV with offsets with four (t/c) equal to 0.005.

V. Conclusions and Recommendations

A. Summary

The aim of this work was to perform an aerodynamic analysis of a forward-backward facing step pair on the upper surface of a low-speed airfoil, belonging to the LEEUAV, due to the presence of solar cells.

For this, two numerical analysis using XFOIL and ANSYS Fluent were performed, both with limitations. In XFOIL, the geometry of the step could not form a 90-degree angle with the airfoil's upper surface, since it resulted in program errors. This lead to the underprediction of the offset effects, more pronounced for the smallest (t/c). In ANSYS Fluent, due to the time and computational resources available, a fully turbulent model was used, which was not capable of predicting transition. Thus, no transition effects were calculated.

The analysis performed with both software programs corresponds to an aircraft, undergoing trim speed changes in level flight at a given altitude, in which the parameter $Re\sqrt{C_l}$ is held constant. This is automatic in XFOIL, but

in ANSYS Fluent it was necessary to implement an iterative strategy, which made the CFD analysis very time consuming.

With XFOIL, it was possible to understand which positions were worst to the airfoil performance and the relationship between the best positions. The $(x/c)_i$ before 0.20 of the chord and after 0.30, and the $(x/c)_f$ before 0.80 of the chord, deliver the worst performance for low C_l. This is extremely harmful because the C_d increase would not give the desired endurance, nor the maximum speed, nor the required power to do so.

The best positions for the FFS is between 0.20 and 0.30 of the airfoil's chord and for the BFS between 0.80 and 0.95. Yet, the BFS have negligible effects when compared to the effects of the FFS. Regarding the relationship between the best positions: for the C_d, the aerodynamic coefficient with most impact, does not have a best position for every C_l range. The C_l presents best results for offsets further away from the LE for the majority of range of angles of attack and the C_m , inverse to C_l, presents best results for offsets closest to the LE. The C_l/C_d and $C_l^{3/2}/C_d$, show similar effects to the C_d, so they do not have a best position for every C_l range.

Regarding the LEEUAV's solar cells analysis, the reduced (t/c) associated with the solar cells has, as consequence, less precise results. Despite this was possible to conclude that the best position for placing the solar cells is between 0.21 and 0.23 of the airfoil's chord.

For the CFD analysis, first it was tested two turbulence models, to see which resembled best the XFOIL's solution. With disappointing absolute results, the model chosen was the SST *k-ω* turbulence model. Then, a small number of offset combinations were analyzed, that served to validate the results from XFOIL, which were in reasonable agreement, except for small details due to the chosen turbulence model. Fluent results showed that the offset presence is always degrading for the airfoil performance relative to the clean airfoil, with the difference, in percentage, proportional to the flow speed. This means that, as speed increases, the influence of the offset relative to the clean airfoil intensifies.

Afterwards, the exact thickness and length of the LEEUAV's solar cells where analyzed, where the influence and relationship between positions were confirmed. In addition, this analysis came to confirm that the best positions for the solar cells are between 0.21 and 0.23 of the airfoil's chord, with better results for the further aft position. For the C_d, it is expected an increase of up to approximately 3% for low C_l, a loss of up to about 2% of C_l and a variation of the C_m of only around 0.5%. Concerning C_l/C_d and $C_l^{3/2}/C_d$, it is expected losses of 5% and 6%, respectively.

And finally, through the airflow visualization, by the velocity contours, streamlines and turbulence kinetic energy, it was possible to confirm the expected flow features described in the literature for the FFS and BFS flows.

B. Concluding Marks

The final objective of this work, is to provide the best position for placing the solar cells, and this is between 21% and 23% of the airfoil's chord, with general best results for the farther position, with losses of around 5% of C_l/C_d for lower C_l relative to the LEEUAV's clean airfoil performance.

C. Future Work

In the future, a more detailed CFD analysis should be performed with a more adequate turbulence model, with boundary layer transition detection capability.

References

[1] Research and Markets, "Unmanned Aerial Vehicles (UAV) Market, By Value and Volume Analysis and Forecast, 2015-2020," 2016.

[2] A. C. Marta and P. V. Gamboa, "Long Endurance Electric UAV for Civilian Surveillance Missions," in *29th International Council of the Aeronautical Sciences Congress*, St. Petersburg, Russia, 2014.

[3] D. Leclercq, M. Jacob, A. Louisot e C. Talotte, "Forward-backward facing step pair - Aerodynamic flow, wall pressure and acoustic characterisation," em *7th AIAA/CEAS Aeroacoustics Conference and Exhibit*, Maastricht, Netherlands, 2001.

[4] J. Morgado, R. Vizinho, M. Silvestre e J. Páscoa, "XFOIL vs CFD performance predictions for high lift low Reynolds number airfoils," *Aerospace Science and Technology,* nº 52, pp. 207-214, 2016.

[5] C. R. Marks, M. P. Rumpfkeil e G. W. Reich, "Predictions of the effect of wing camber and thickness on airfoil self-noise," em *20th AIAA/CEAS Aeroacoustics Conference*, Atlanta, 2014.

[6] Fluent Inc., "Modeling Turbulence," em *FLUENT 6.1 User's Guide*, Fluent Inc., 2003, pp. 659-740.

[7] ANSYS, Inc, ANSYS Fluent User's Guide, ANSYS, Inc., 2013.

[8] N. M. Silva, "Parametric Design, Aerodynamic Analysis and Parametric Optimization of a Solar UAV," Instituto Superior Técnico, Lisboa, 2014.

[9] J. v. Ingen, "The eN Method for Transition Prediction. Historical Review of Work at TU Delft," em *38th Fluid Dynamics Conference and Exhibit*, Seattle, 2008.

Appendix

A. LEEUAV Airfoil Coordinates

Upper Surface					
x	y	x	y	x	y
1.0000	0.0015	0.7409	0.0682	0.2321	0.1012
0.9998	0.0016	0.7270	0.0706	0.2190	0.0997
0.9990	0.0019	0.7129	0.0729	0.2061	0.0981
0.9978	0.0025	0.6986	0.0752	0.1935	0.0964
0.9961	0.0033	0.6841	0.0775	0.1813	0.0945
0.9938	0.0043	0.6694	0.0798	0.1693	0.0924
0.9911	0.0055	0.6545	0.0820	0.1577	0.0902
0.9880	0.0069	0.6395	0.0842	0.1464	0.0878
0.9843	0.0085	0.6243	0.0863	0.1355	0.0853
0.9801	0.0103	0.6091	0.0883	0.1249	0.0826
0.9755	0.0122	0.5937	0.0903	0.1147	0.0798
0.9704	0.0143	0.5782	0.0922	0.1049	0.0768
0.9649	0.0165	0.5627	0.0940	0.0955	0.0736
0.9589	0.0187	0.5471	0.0957	0.0865	0.0703
0.9524	0.0210	0.5314	0.0973	0.0778	0.0667
0.9455	0.0234	0.5157	0.0988	0.0696	0.0631
0.9382	0.0258	0.5000	0.1002	0.0618	0.0592
0.9304	0.0281	0.4843	0.1014	0.0545	0.0552
0.9222	0.0305	0.4686	0.1026	0.0476	0.0512
0.9135	0.0329	0.4529	0.1036	0.0411	0.0470
0.9045	0.0353	0.4373	0.1044	0.0351	0.0428
0.8951	0.0376	0.4218	0.1052	0.0296	0.0385
0.8853	0.0400	0.4063	0.1057	0.0245	0.0343
0.8751	0.0423	0.3909	0.1062	0.0199	0.0302
0.8645	0.0447	0.3757	0.1065	0.0157	0.0262
0.8536	0.0470	0.3605	0.1067	0.0120	0.0223
0.8423	0.0494	0.3455	0.1067	0.0089	0.0187
0.8307	0.0517	0.3306	0.1066	0.0062	0.0154
0.8187	0.0541	0.3159	0.1063	0.0039	0.0123
0.8065	0.0565	0.3014	0.1058	0.0022	0.0094
0.7939	0.0588	0.2871	0.1052	0.0010	0.0067
0.7810	0.0612	0.2730	0.1045	0.0002	0.0039
0.7679	0.0635	0.2591	0.1035	0.0000	0.0000
0.7545	0.0659	0.2455	0.1024		

Lower Surface					
x	y	x	y	x	y
1.0000	-0.0015	0.7409	0.0173	0.2321	-0.0185
0.9998	-0.0014	0.7270	0.0168	0.2190	-0.0194
0.9990	-0.0012	0.7129	0.0162	0.2061	-0.0203
0.9978	-0.0007	0.6986	0.0156	0.1935	-0.0210
0.9961	-0.0001	0.6841	0.0149	0.1813	-0.0218
0.9938	0.0007	0.6694	0.0142	0.1693	-0.0224
0.9911	0.0016	0.6545	0.0135	0.1577	-0.0229
0.9880	0.0027	0.6395	0.0127	0.1464	-0.0234
0.9843	0.0039	0.6243	0.0119	0.1355	-0.0238
0.9801	0.0052	0.6091	0.0110	0.1249	-0.0241
0.9755	0.0066	0.5937	0.0101	0.1147	-0.0242
0.9704	0.0080	0.5782	0.0092	0.1049	-0.0243
0.9649	0.0095	0.5627	0.0082	0.0955	-0.0243
0.9589	0.0109	0.5471	0.0072	0.0865	-0.0242
0.9524	0.0123	0.5314	0.0061	0.0778	-0.0239
0.9455	0.0136	0.5157	0.0050	0.0696	-0.0236
0.9382	0.0148	0.5000	0.0038	0.0618	-0.0231
0.9304	0.0158	0.4843	0.0026	0.0545	-0.0225
0.9222	0.0168	0.4686	0.0014	0.0476	-0.0217
0.9135	0.0176	0.4529	0.0001	0.0411	-0.0209
0.9045	0.0182	0.4373	-0.0012	0.0351	-0.0200
0.8951	0.0187	0.4218	-0.0025	0.0296	-0.0190
0.8853	0.0191	0.4063	-0.0039	0.0245	-0.0178
0.8751	0.0194	0.3909	-0.0052	0.0199	-0.0166
0.8645	0.0196	0.3757	-0.0066	0.0157	-0.0154
0.8536	0.0197	0.3605	-0.0079	0.0120	-0.0140
0.8423	0.0197	0.3455	-0.0092	0.0089	-0.0126
0.8307	0.0196	0.3306	-0.0105	0.0062	-0.0112
0.8187	0.0195	0.3159	-0.0118	0.0039	-0.0096
0.8065	0.0193	0.3014	-0.0130	0.0022	-0.0079
0.7939	0.0190	0.2871	-0.0142	0.0010	-0.0060
0.7810	0.0186	0.2730	-0.0154	0.0002	-0.0038
0.7679	0.0182	0.2591	-0.0165	0.0000	0.0000
0.7545	0.0178	0.2455	-0.0175		